An Automated Malignant Tumour Localization Algorithm for Prostate Cancer Detection in Trans-rectal Ultrasound Images

by

Jim Mu Li

A thesis
presented to the University of Waterloo
in fulfillment of the
thesis requirement for the degree of
Master of Applied Science
in
Electrical and Computer Engineering

Waterloo, Ontario, Canada, 2004

Author’s Declaration for Electronic Submission of a Thesis

I hereby declare that I am the sole author of this thesis. This is a true copy of the thesis, including any required final revisions, as accepted by my final examiners.

I understand that my thesis maybe made electronically available to the public.

Abstract

The goal of this thesis is to design, implement and evaluate an automated algorithm to detect cancerous tissues and segment the malignant tumour in ultrasound images of the prostate. To accomplish this goal, first, the important image features which would lead to the optimal segmentation are identified. This work focuses on the local texture feature and spatial features. Various approaches to extract the local texture feature are explored, including grey-level co-occurrence matrix (GLCM), recurrent random-pulsed neural networks (RNN), and a novel wavelet-based filter. The spatial features are represented using conventional one dimensional fuzzy membership functions and novel multi-dimensional fuzzy membership functions. The texture and spatial features are combined using the fuzzy inference system.

Two of the techniques investigated in this thesis could potentially constitute the basis for key paradigm shifts in medical imaging research. One of these is the idea that medical images in general, and ultrasound images in particular, contain information which are hidden from medical professionals due to limitations in the human visual system. This thesis shows that this information could be extracted using a computerized approach by separating the deterministic components in the image from the indeterministic components, or noise. The other idea concerns the representation of multidimensional statistical distribution information with fuzzy membership functions with the corresponding dimensions. This thesis shows that increasing the number of dimensions with which to represent the statistical distributions results in a more accurate mapping of information that relates to human anatomy, which is essentially 3D in nature.

In the thesis, the natures of the various techniques are explored by testing on synthesized images. Then, these approaches are adapted to the ultrasonic prostate cancer segmentation problem and are evaluated with trans-rectal ultrasound images (TRUS).

The segmentation using only texture features yields results with high sensitivity. When the spatial features are incorporated using the fuzzy inference system, the specificity of the diagnosis improves dramatically and the overall classification accuracy is also increased. Clinically, this automated diagnostic system could be used as a decision support tool for radiologists when identifying suspicious regions in the prostate from which to draw biopsy samples. The proposed system improves the consistency of the cancer detection process and could provide savings in both time and cost in the prevention and treatment of prostate cancer.

Acknowledgements

I would like to thank my co-supervisors, Dr. M.M.A. Salama and Dr. G.H. Freeman, in their guidance in completing this thesis. I would like to thank Dr. H.R. Tizhoosh for his input on the fuzzy inference system sections. I would like to thank Dr. A. Fenster for his suggestions on how to carry out the receiver operation curve analysis and his help with the medical aspect of the system. I would like to thank Dr. D. Downey for providing the original ultrasound images as well as the prostate and cancerous region outlined images. I would like to thank Dr. K. Rizkalla for her views on the medical issues discussed in the thesis. I would also like to thank Dr. T. K. Abdelgalil for giving me valuable feedbacks on earlier versions of this thesis.

Table of Contents

List of Figures

List of Tables

Chapter 1
Introduction

Prostate cancer is the second most common type of cancer for North American men. In 2002, it claimed the lives of 30,200 Americans and 4,300 Canadians, while 207,200 new cases have been confirmed in the two countries [1][2].

If prostate cancer is detected early, complete recovery is possible. Prostate specific antigen (PSA) value analysis and digital rectal examination (DRE) are performed to detect signs of cancer during screening, and then prostate biopsy is performed for conclusive diagnostic of the disease. However, prostate biopsy is a costly and physically invasive procedure for the patient. Thus, it would be beneficial if the number of biopsies could be reduced without seriously reducing the sensitivity and specificity of the diagnosis result. This is usually accomplished with transrectal ultrasound (TRUS) image analysis. In TRUS analysis, a trained radiologist is able to manually identify, with a moderate degree of confidence, the benign and malignant regions in the prostate on the TRUS image from intensity, local texture, and spatial knowledge regarding cancer tissue distribution. This information is then used for biopsy planning and guidance.

However, manual segmentation is a time consuming task as there is often dozens of 2D TRUS slices associated with each single clinical case. The goal of this research is to design an automated algorithm to segment the malignant and benign regions within the prostate on TRUS images. The automated region segmentation could improve both the efficiency and effectiveness of the prostate cancer diagnostic process. It could potentially lead to a reduction in the number of biopsies required for high fidelity diagnosis results.

The content of the thesis is divided into several chapters. Chapter 2 to 4 defines the problem and the current state-of-the-art techniques in dealing with this issue, and in Chapter 5 to 8 I present my proposed solution.

More specifically, in Chapter 2, the medical background on prostate cancer is presented, with emphasis on attributes of the disease which could lead to improved automated segmentation in TRUS images. The ultrasound modality and its characteristics are introduced in Chapter 3. The subject of automated malignant tumour segmentation in TRUS images has been previously examined by Loch [3] and Scheipers [4]. These currently state-of-the-art techniques, along with the relevant associated advanced tools in medical image analysis, specifically in segmentation, are explored in detail in Chapter 4. In Chapter 5, the system level description of the proposed automated diagnostic system is presented. Chapter 6 explores various techniques to capture and improve the local textural feature. In Chapter 7, the issue of extracting statistical spatial feature using standard 1D fuzzy membership functions is examined. Chapter 7 also discusses converting feature distributions into fuzzy membership functions and the fuzzy inference rules which combine the features to provide binary classification outputs. In Chapter 8, the concept of multi-dimensional fuzzy membership functions is explored to improve the representation of the statistical spatial information.

The major issues examined in this work include: 1) identifying key feature groups which leads to the optimal segmentation of the tissue classes (Chapters 2, 3, 4); 2) improving these distinguishing features and designing novel feature extraction approaches (Chapters 6, 7, 8); and 3) selecting and optimizing the classifier (Chapters 4, 5, 7).

Chapter 2
Medical Background on Prostate Cancer

2.1 Cells and Cancer

The human body is made up of many cells. Normally, the cells grow and die in a controlled manner. However, sometimes, cells will keep dividing in an uncontrolled manner, forming tumours. Most tumours do not invade surrounding tissues and are non-life threatening. They are deemed benign tumours. If the tumour does invade and destroy nearby tissues, it is classified as malignant tumour or cancer and might threaten the person's life.

2.2 The Prostate and Prostate Cancer

The prostate organ is one of the male sex glands and is located bellow the bladder and around the urethra. The prostate is visualized in Figure 1. The prostate is about the size of a walnut and is responsible for producing most of the semen.

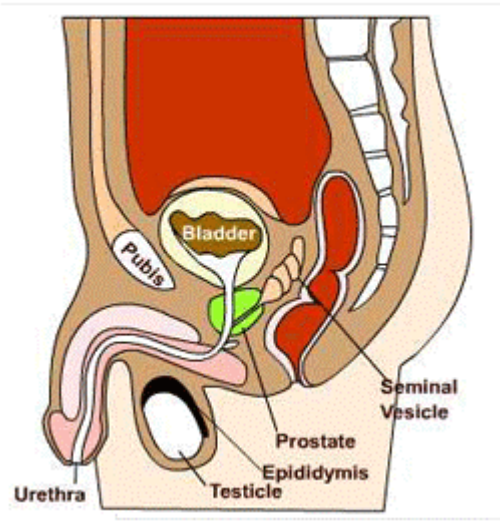

Figure 1. Anatomy of the Prostate.

Usually, early stages of prostate cancer show no symptoms. As the tumour grows, the prostate tissues constrict the urethra, causing difficulties in urinating. This is usually the first symptom of prostate cancer. However, there are also other diseases that will also cause difficulties in urinating.

To detect prostate cancer, one common method is digital rectal examination, during which the doctor will place a gloved finger inside the rectum and probe for abnormalities. However, this approach could only detect a small percentage of cancer cases since some tumours are too small to be noted using this approach and some are located away from the rectum. Prostate Specific Antigen (PSA) is a protein in the blood, an abnormal quantity of which could indicate the presence of prostate cancer. This is another common detection method. The expected PSA level is usually proportional to the prostate volume. Thus, to use the PSA indicator to determine likelihood of cancer, the prostate volume needs to be accurately estimated.

Medical imaging tools such as ultrasound, x-ray, IVP, bone-scan, and MRI help the doctors visualize the prostate and surrounding regions for signs of cancer.

2.3 Visualization in Pathology

For conclusive diagnosis, the doctors will insert a needle into regions of the prostate which are deemed to be suspicious. The needle extracts a small piece of tissue. The tissue samples are then observed using the microscope to determine the grade of cancer. The prostate cancer grading system was developed by Gleason [5]. In the Gleason system, tumours having grade 4 and below are deemed to have low malignant potential. In Table 2.1, the verbal descriptions for a tumour of Gleason grades 1 to 5 are given.

Table 1. Tumour Definitions in the Gleason Scoring System [6].

Gleason grades	Definitions
1	Tumour closely packed. Uniform, packed glands arranged in a nodule with pushing borders.
2	Glands with more variable size and shape, separated by abundant stroma. Tumour nodules less circumscribed.
3	Tumour composed of uniform small glands growing in infiltrative patterns.
4	Small acinar structures. Solid fused glands.
5	Minimal glandular differentiation.

From Table 1, we can conclude that, pathologically, the more serious the tumour, the more the glands will lose shape and structure and start to fuse. Pathologic samples of malignant and benign tissues of the prostate are displayed in Figure 2.

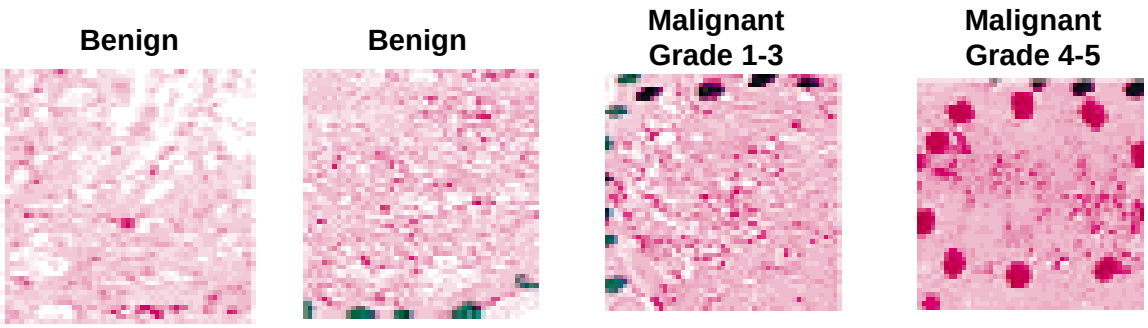

Figure 2. Pathologic Samples of Malignant and Benign Tissues of the Prostate [3].

In Figure 2, we see that as the tumour gets more serious, there is more fusing of the glands and appearances of acinar structures (granular mass).

2.4 Localization

The prostate structure is visualized in Figure 3.

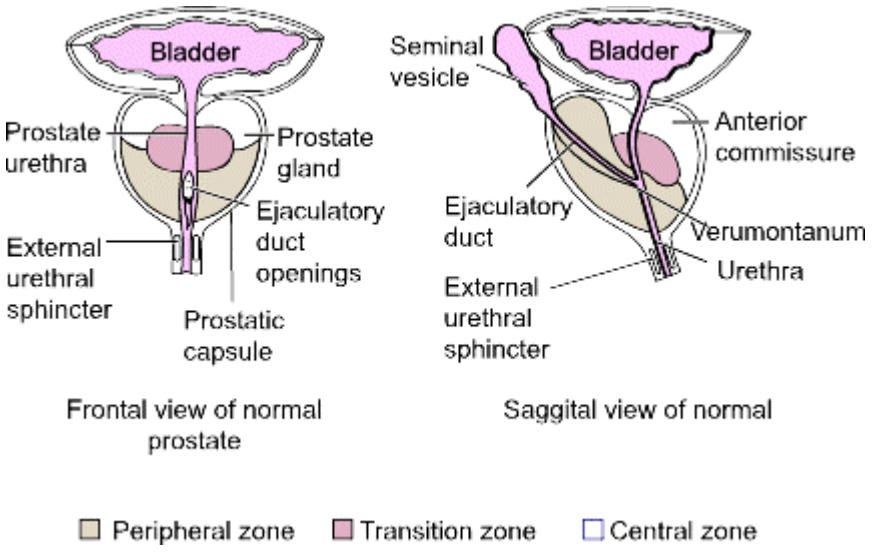

Figure 3. Prostate Structure [7].

Statistically, 68% of prostate cancer originates in the peripheral zone, while only 24% originate in the transition zone [8].

2.5 Chapter Summary

In this Chapter, a brief introduction into the prostate and prostate cancer is given. Some of the important characteristics of the disease which aid in the TRUS diagnosis, such as its visualization in pathology and localization, are also examined.

Chapter 3
Trans-rectal Ultrasound as a Tool for Prostate Cancer Diagnosis

In this chapter, we examine the ultrasound imaging modality and how radiologists determine suspicious cancerous regions from the ultrasound images.

3.1 Trans-rectal Ultrasound

3.1.1 Ultrasound Physics

Ultrasound is a safe and non-invasive medical imaging technology which has been widely applied to aid in the detection, diagnosis, and treatment planning of diseases for more than 50 years. The principle behind ultrasound is based on the nature of waves. In diagnostic ultrasound, the ultrasound transducer emits a high-frequency wave, which interacts with the tissues of interest and is absorbed by a detector. The nature of the waves' interactions with the tissues provides important diagnostic information concerning the tissues of interest. There are five main types of interactions, namely reflection, refraction, scattering and diffraction, interference, and absorption [1][9].

Reflection is by far the most important of the five interactions. When the ultrasound wave arrives at the interface between tissues, part of the acoustic energy is reflected. The reflected energy could be used to identify the type of tissue encountered. Each tissue is characterized by an acoustic impedance value, which is defined as:

$$Z = \rho v \qquad \textbf{Equation 1}$$

where ρ denotes the density of the medium, measured in kg/m^3, v represents the velocity of sound in the medium, measured in m/s, and Z denotes the acoustic impedance, measured in kg/m^2s. The fraction of acoustic energy reflected at the interface depends on the acoustic impedances of the two acoustic media as follows:

$$\alpha_R = \left(\frac{Z_2 - Z_1}{Z_1 + Z_2} \right)^2$$ **Equation 2**

where Z_1 and Z_2 denotes the acoustic impedances of the two mediums and α_R denotes the percentage of energy reflected.

3.1.2 Imaging Modes

An important concept in ultrasound imaging is echo ranging. Echo ranging relates the time difference between the transmission and reception of the signal with the depth of the biological interface which produced the reflection. The concept is defined by the following equation:

$$d = vt$$ **Equation 3**

where *v* denotes the speed of sound, *t* represents the time at which the wave is received (the wave is transmitted at *t*=0), and *d* denotes double of the depth of the tissue interface.

There are various modes of ultrasound scanning, including A-mode, B-mode, real-time mode and transmission mode. The images analyzed in this thesis are obtained using B-mode scanning. Therefore, we will examine B-mode scanning in more detail.

Unlike A-mode scanning, which provides a one-dimensional amplitude graph of the tissue interfaces in the path of wave transmission, B-mode scanning represents these amplitudes by the brightness of an image element spatially located on a 2-D portrait of the anatomical structure of interest. By performing B-mode scanning in many directions, we obtain a complete 2-D representation of the surface of the structure.

3.1.3 TRUS Scanning Motion

Trans-rectal ultrasound (TRUS) is a procedure specifically designed to image organs which surrounds the rectum. To image the entire prostate using this technique, a ultrasound

transducer is inserted into the rectum and scanning occurs in a fan shape, from the base to the apex of the prostate. This is demonstrated in Figure 4.

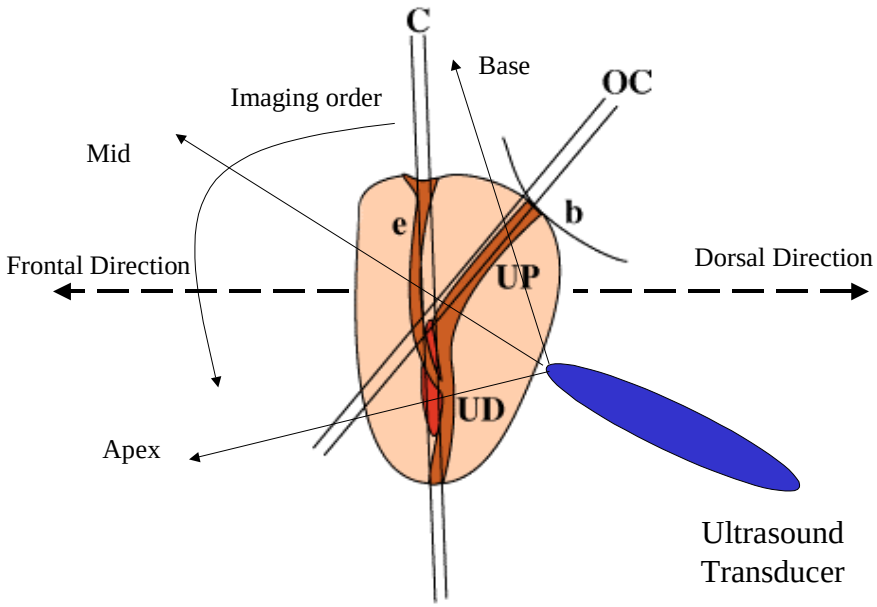

Figure 4. TRUS Image Acquisition Process.

3.2 Radiologist's Diagnostic Process Using TRUS

Figure 5 (left-panel) shows an example of a TRUS slice. The malignant region outlined by the radiologist is represented in Figure 5 (right-panel).

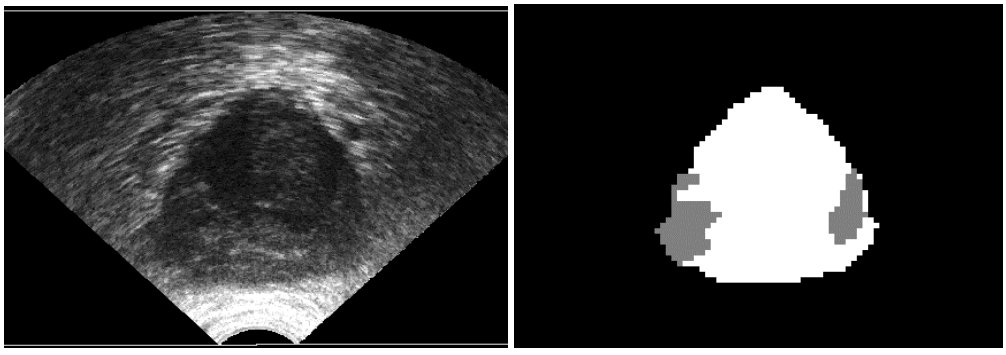

Figure 5. The Segmentation Problem: Original TRUS Image of the Prostate (left panel) and Manual Segmentation of Malignant Region Performed by a Radiologist (right panel).

Traditionally, the radiologists used two major features for identifying suspicious regions of cancer in ultrasound images: the intensity and spatial location. In terms of intensity, radiologists usually associate the diminished echogenic regions in the peripheral zone of the prostate as being cancerous [10]. However, there is a low specificity associated with this malignancy localization method [8]. Furthermore, 25% of prostate cancer appears in the isoechoic regions within the peripheral zone, and these cases cannot be detected by using intensity-based indicators [8]. Therefore, intensity, alone, has been rarely used in previous research on automated prostate cancer malignancy localization. As we have seen in Chapter 2, 68% of prostate cancer originates in the peripheral zone, whereas only 24% originates in the transition zone. This fact is used extensively by radiologists to reject suspicious regions identified by the intensity feature which resides in the transition zone.

Other than intensity and location, there is another class of features called textural features. The parenchyma of malignant tissues differs from that of benign tissues. As a result, the acoustic energy is reflected and scattered differently [9]. Part of this difference is manifested in the local texture variation in the TRUS images. Textural features are less perceptible using human vision, but are found to be quite effective in distinguishing between the malignant and benign tissues in TRUS images [4]. In this thesis, the major emphasis is placed on exploring textural and spatial (location) features.

3.3 Chapter Summary

In this chapter, the modality of ultrasound is examined. The procedure of how radiologists identify suspicious malignant regions is also explored.

Chapter 4
State-of-the-Art Computerized Medical Image Analysis Techniques for Malignant Tumour Localization

In this chapter, the computerized medical image analysis process, alone with the relevant tools, are examined. The major emphasis is placed on image segmentation. Various currently state-of-the-art techniques for the malignant tumour localization problem is explored. At the end of the chapter, potential approaches to improve the current techniques are discussed.

4.1 The Medical Image Analysis Paradigm

Medical imaging provides effective and non-invasive mapping of the anatomy of subjects. Medical imaging analysis is usually applied in one of two capacities: 1) to gain scientific knowledge of diseases and their effect on anatomical structures in-vivo, and 2) as a component for diagnostics and treatment planning.

Medical image analysis is usually performed manually by trained radiologists. However, manual analysis of images is a time consuming process and is susceptible to human errors. Due to the increased application of medical imaging in the clinical and research areas in the recent years, the need for computer-assisted approaches to analyze these images has also increased. Recent developments in image processing research and the exponential growth of computational power have made computer-assisted medical image analysis viable.

The computer-assisted medical image analysis process could be divided into the following subtasks: image acquisition, pre-processing, contour segmentation, feature construction, feature selection, region-of-interest (ROI) segmentation, and image classification. This paradigm is displayed in Figure 6.

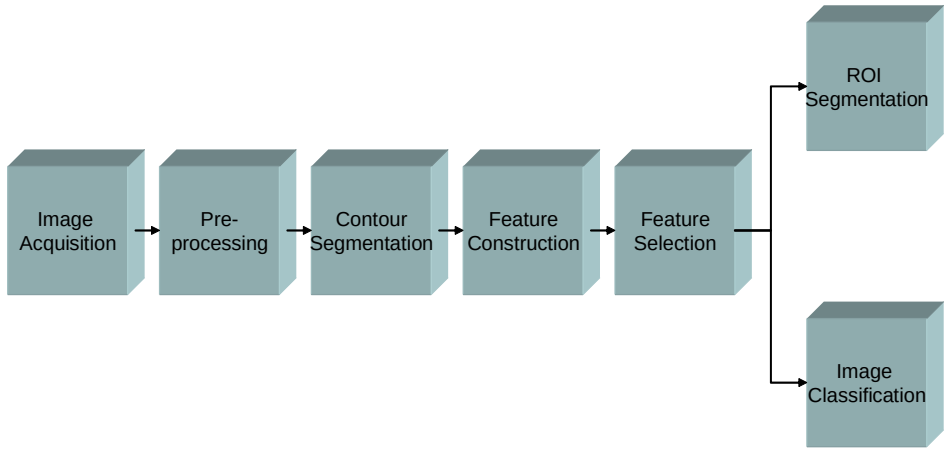

Figure 6. The Computer-assisted Medical Image Processing Paradigm.

Image acquisition involves acquiring the image from the object or person of interest. The common medical imaging modalities include X-ray, CT, ultrasound, and MRI. These imaging modalities contain the hardware and software that allow the visualization of the anatomical structure of interest. Recently, some of these modalities also contained low level hardware and software that accomplish pre-processing tasks.

Pre-processing includes two basic and distinct functions: enhancement and denoising. Denoising refers to the removal of artifacts and information which are not relevant to the analysis. This is often accomplished by removal of high frequency contents. Enhancement deals with improving the visibility of the structure of interest by increasing the contrast or emphasizing the relevant contours.

In contour segmentation, the contour of the structure of interest is delineated. This is accomplished so that subsequent analysis could focus on a specific anatomy of interest.

Image features are well defined properties associated with the image which allows the radiologist or computer algorithm to make inferences about the structures of interest in the image. Common features include intensity based features and texture features. Feature construction is the process through which the feature space is designed and calculated. Theoretically, there are an unlimited number of possible feature spaces. This is referred to as the ‘curse of dimensionality’. To make useful inferences from these features in a reasonable amount of time, the number of features needs to be reduced to the most relevant ones for the task at hand, a process called feature selection.

Once the features are constructed and selected, inferences could be made using these features. One end goal could be locating regions-of-interest in the image being processed or ROI segmentation. For example, the features could be used to determine where on the image a malignant tumour is occurring. Another end goal could be classification. For example, the selected features could be used to determine if the particular image contains malignant tissue or not. If no malignant tissue is detected, the image is classified as benign.

In this work, the goal is localizing malignant tumour growth in TRUS images and the focus will be on the feature construction, feature selection and ROI segmentation aspects of medical image analysis.

4.2 Overview of Medical Image Segmentation Techniques

4.2.1 Introduction

One important task facing radiologists is the delineation of the contour of anatomical structures, also called segmentation. The roles of segmentation includes: 1) quantification of tissue volume, 2) diagnosis, 3) localization of pathology, 4) study of anatomical structure, 5) treatment planning, and 6) computer-integrated surgery. [11]

4.2.2 Terms and Definitions

Manual interaction:

Many computer-assisted segmentation tasks require incorporating the knowledge of operators. When manual interaction is required, there is usually a tradeoff between the segmentation accuracy and the degree of automation. Usually, the greater amount of human interaction applied, the greater the segmentation accuracy, but the lower the degree of automation. We also have to be aware that there is possibility of human error introduced in the final segmented result whenever manual interaction is involved in the procedure.

Intensity inhomogeneity:

Intensity inhomogeneity refers to regions in medical images that belong to the same tissue, but exhibit varying levels of intensity. This is usually due to artificially introduced intensity variation so that regions that should have the same intensity have different intensities.

Partial-volume effect and soft-segmentation:

The partial-volume effect refers to the case where two different tissues overlap and contribute to the intensity of the same image element on a medical image. To take this effect into consideration, some segmentation algorithms allows for soft-segmentation. In soft-segmentation, a single image element could be partitioned into two or multiple tissue classes. This approach is usually accomplished with a fuzzy method.

Validation:

To evaluate the accuracy of the segmentation method under consideration, we apply validation models. When performing validation, we have to first select the truth model with which to compare the segmented result. A common truth model is the manual segmentation by the experienced operator. However, manual segmentations could involve human error.

Therefore, it is not a perfect truth model. Another truth model used for validation is the physical phantom. The physical phantom simulates the image acquisition process accurately. However, it does not reflect the physiological properties of the anatomical structure to be captured. A third truth model is the computational phantom, which simulates the physiological anatomy precisely, but does not capture the image acquisition process.

Once the truth model is selected, we apply figures of merit to measure the accuracy of the segmentation results. Some common figures of merit include the number of pixels misclassified and the distance to true boundary.

4.2.3 Thresholding

Thresholding segments the image by setting a binary partition in image element intensities. To perform thresholding, we have to 1) select the appropriate threshold and 2) group pixels with intensities above this threshold into one class and those below into a second class. If we wish to segment the image into several classes, we can select several intensity thresholds and apply the segmentation. This is referred to as multi-thresholding.

The key to thresholding is selecting the appropriate threshold value to separate the image elements. A common method is to use valleys of the histogram profile as thresholds. The threshold is usually selected interactively, however automated methods also exist [12].

The following is an example of how the thresholding method is applied in practice. Figure 7 is the ultrasound image of a prostate. To preprocess this image, we might want to remove the border regions. We might also want to segment prostate regions from the non-prostate regions within the ultrasound portions. Therefore, we set the number of classes to 3.

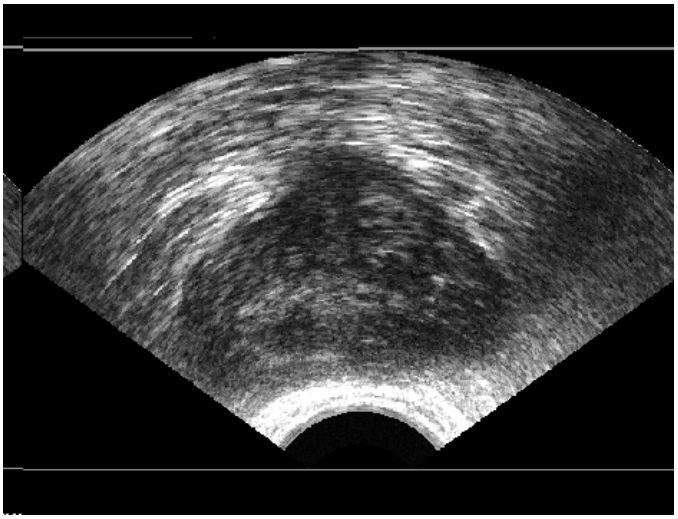

Figure 7. Original Ultrasound Image of the Prostate.

To apply thresholding, we first calculate the histogram profile of the original image (Figure 8). Then, we apply the thresholds at the visible valleys in the intensity profile (arrows on histogram image). The result of the segmentation is displayed in Figure 9.

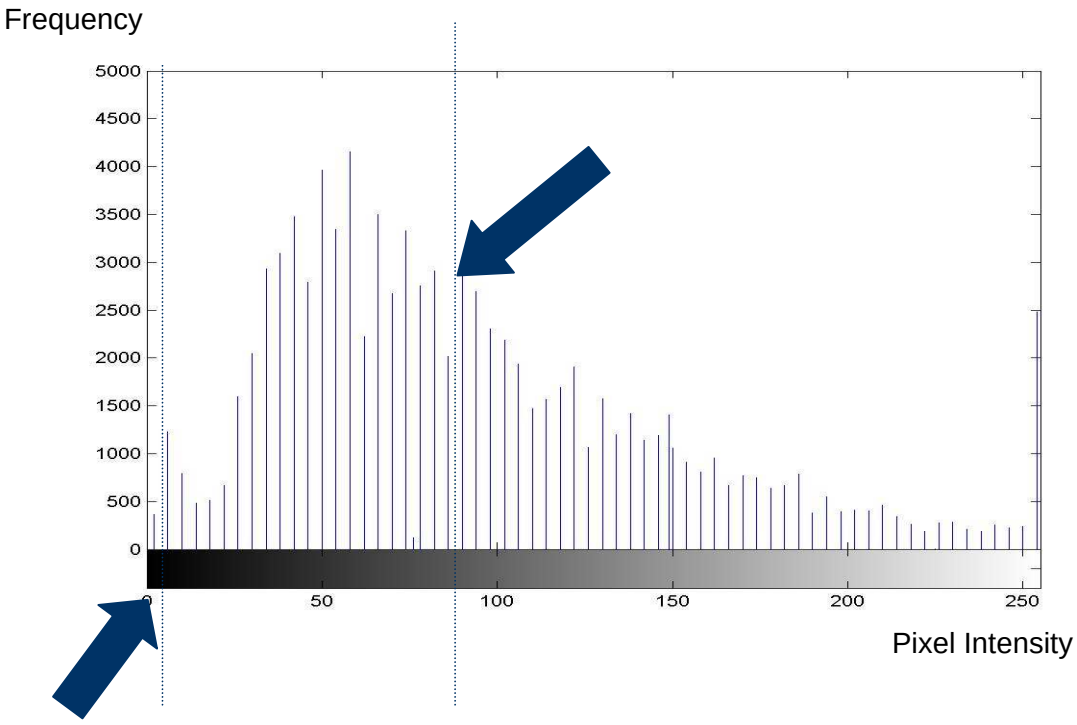

Figure 8. Histogram of the Original Image.

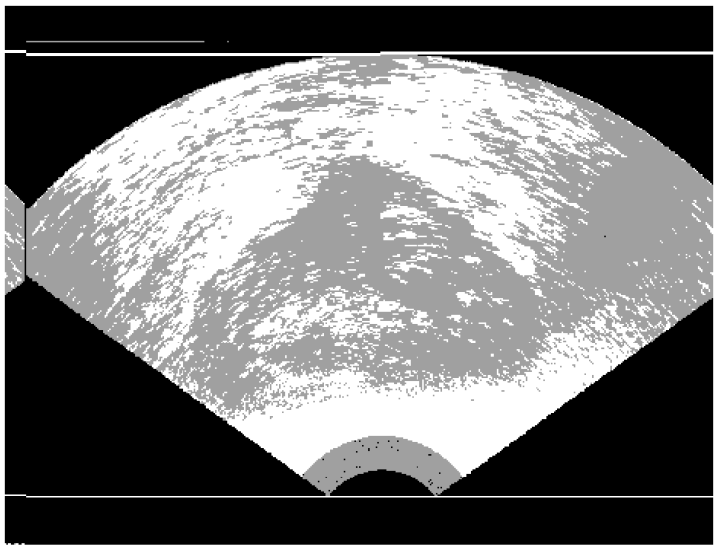

Figure 9. Segmentation by Thresholding.

The example above demonstrates some of the advantages and disadvantages of the thresholding approach. One advantage is the simplicity of the method, which involves minimal implementation and computational requirements. This method is also very effective when the regions to be segmented have homogeneous intensities. The main disadvantage of the method is that it is very sensitive to noise. From Figure 9, we can see that some regions, which are non-prostate, are segmented as being part of the prostate. This is the result of noise.

Thresholding is usually used as the first or last step in a series of image processing procedures. New research on thresholding mainly focuses on reducing the sensitivity of the method to noise. In 1995, Li et al. incorporated local intensity information to thresholding for tumour detection in digital mammography [13]. In 1998, Lee et al. added connectivity information to thresholding to segment brain tissues in MR images [14].

4.2.4 Region Growing

The region growing method segments the image based on predefined connectivity measures. To apply the region growing method, we have to 1) define the connectivity measures, 2) plant the seed (usually with manual interaction), and 3) grow the region until the connectivity criteria is no longer satisfied.

The key to the region growing method is selecting the connectivity criteria or the stop criteria. This is discussed in detail in Haralick-Shapiro [15]. Edges are a simple form of the stop criteria. More complex stop criteria could be constructed using complex mathematical equations taking textural, spatial, and intensity features as inputs.

Region growing is effective in delineating small and simple structures when well-defined stop criterions exist. A well-defined stop criteria could be a strong edge or a region with homogeneous intensity. One disadvantage of the region-growing method is that it requires manual interaction to plant the seed, therefore it is not completely automated. It is also sensitive to noise, which could cause the appearance of holes in a segmented region or two distinct regions to be connected.

Region growing is usually not used alone but in a chain of image processing procedures. It has been applied primarily in the delineation of tumours and lesions [16][17].

4.2.5 Classifiers

Classifiers provide binary separation of the feature space based on a mapping provided in the manually segmented training data. To apply the classifier, 1) training data needs to be obtained (usually through a manual process). The training data provides the input-output mapping. This is not a direct mapping, but rather a mapping between the features extracted from the training data and the segmented output. After the training data is obtained, 2)

features are extracted from the evaluation input set. 3) These features are then used along with the mapping from the training data to classify the evaluation image elements.

The key to designing the classifier is selecting the optimal features and choosing the most appropriate classification method. The classification methods could be roughly divided into two categories: non-parametric classifiers and parametric classifiers. Non-parametric classifiers hold no underlying assumption on the statistical distribution of the data to be classified. This class of classifiers includes the nearest neighbour, k-nearest neighbour, and the Parzen window. Parametric classifiers make the underlying assumption that there exists a certain statistical distribution in the data to be classified. The Gaussian distribution is usually assumed. The maximum-likelihood method and Bayes method are examples of parametric classifiers.

The advantage of the classifier is that it is in general non-iterative. Therefore, it is computationally efficient. However, for good classification results with these methods, feature spaces which clearly distinguish the classes are required. Manual interaction to obtain training data is also required for most cases. Furthermore, if training data is too small, these approaches could lead to biased results when applied to the general population. The classifier is also sensitive to noise and intensity inhomogeneities.

The classifier is one of the most widely applied methods in medical image segmentation. This is partially due to the fact that in practice, there is usually a human determined desired goal for each segmentation case. Therefore, supervised classifiers are ideal for training the segmentation algorithm to segment toward this target.

The classifier was used as early as 1985 by Vannier and Butterfield in grey matter/ white matter segmentation in MRI of the brain [18]. More recently, artificial neural networks (ANN)

has been trained as a supervised classifier using wavelet features for texture classification [19].

4.2.6 Clustering

Clustering is close in theory to classifiers. However, unlike classifiers, no training data is used. Instead, the evaluation data is computed iteratively such that it trains itself. At the start of the cluster algorithm initial parameters are selected. Then an iterative process of characterizing the properties of each class and then segmenting the image based on the class characterization calculated in the previous step is undertaken. The algorithm terminates when the stop criterion is met.

Clustering algorithms include the k-mean, fuzzy c-mean, and expectation maximization (EM) algorithms. The K-mean algorithm iteratively calculates the mean intensity of the classes and segments the image elements into classes with the closes mean. Fuzzy c-mean is a generalized version of k-mean, using fuzzy theory to allow for soft-segmentation. Expectation maximization is a clustering approach that assumes an underlying Gaussian distribution.

The advantage of clustering is it requires no training data. However, the performance of clustering algorithms is sensitive to initial parameters. This problem is especially acute with EM. Clustering is also sensitive to noise and intensity inhomogeneities.

Clustering is usually applied when there are no training data available. In 1994, EM clustering is applied by Liang et al. for tissue segmentation in MRI [20]. In 1999, Pham et al. implemented the adaptive fuzzy c-mean, which improved the robustness of clustering algorithms to intensity inhomogeneities [21].

4.2.7 Deformable Models

The deformable models or snakes approach to image segmentation uses closed parametric curves that deform under internal and external forces to delineate object boundaries. It involves the following steps: 1) manual placement of initial contour close to the object boundary; then the contour undergoes an iterative relaxation process where 2) the internal force is calculated from within the curve to keep it smooth during the deformation and 3) the external force is calculated from the image to drive the curve toward the desired boundary.

The advantages of the method are that it can generate closed parametric curve directly from the image (external force) and provides smoothness constraints for robustness against noise (internal force). The disadvantages include the requirement of manual interaction to place the initial contour and result sensitivity to the initial contour placement.

The deformable model is usually applied to delineate contours of large organs. In 1996, Davitzikos et al. applied the deformable model to reconstruct the cerebral cortex from MRI [22]. In 2003, this approach is applied to semi-automatically delineate the contour of the prostate in TRUS images [1].

New research in deformable models deals mostly with the issue of reducing the sensitivity to the initial contour. These novel approaches include balloons [23], the geometric model [24], shape modeling with front propagation [25], and gradient vector flow [26].

4.3 Computer-aided Prostate Cancer Diagnosis: Current State-of-the-Art and Improving Upon Existing Algorithms

Classically, research in computer-aided tissue diagnosis have focused on two major areas, namely, selecting the appropriate features from the available feature set and choosing the optimal classifier to distinguish between the tissues. In this thesis, other than

these two mentioned areas, important focus will also be placed on introducing novel approaches to construct features which provide greater distinction between the classes compared to what is available based on existing feature extraction techniques.

One of the primary discriminating features of the different regions is the local texture. Consequently, a method which involves extracting the textural features and then feeding them as inputs into a classifier that yields a binary decision seems a viable approach. Recently, the idea of using a feedforward artificial neural network (ANN) to distinguish between the malignant regions and benign regions in TRUS images has been explored by Loch et al. [3]. However, in their work, the training and evaluation samples (18×18 pixel blocks within the image) were randomly selected from the same set of images. Therefore, whether this approach leads to generalized results for the image samples which are not used in the training set is questionable.

Loch et al. used six local texture descriptors as inputs for the feedforward ANN, including the number of edges, dispersion of the edge intensity, average size of the edges, dispersion of the edge size, contrast intensity of the edges, and dispersion of the edge contrast. A comprehensive classical approach to texture feature construction was demonstrated by McNitt-Gray et al. [27], in which 59 spatial and textural features were evaluated in the segmentation of chest radiographs. However, since these textural features are mostly equation-based, they are not guaranteed to fully capture the complex texture properties in ultrasound images.

Gelenbe's supervised recurrent random pulsed neural network (RNN) has offered a more structurally sophisticated alternative to capture the complex textural information that is based on the recursive nature of the training of the RNN network weights [28]. Also, the

RNN is simple to implement, since it encodes texture information in the local neighbourhood without explicitly extracting features.

In this thesis, we will examine several texture feature extraction approaches, starting with the more classical grey-level co-occurrence (GLCM) features, which have been applied by Schiepers et al. in their attempt to identify malignant tumours in ultrasound images of the prostate. Then, we will explore the more novel RNN approach, which has yet to be applied to ultrasound images. Finally, we will attempt to design novel feature spaces specifically designed to distinguish between the malignant and benign tissue textures.

Fuzzy inference can be used to process the results from spatial and textural information analyses and provide a binary classification. Scheipers et al. have used spectrum and texture parameters, extracted from the prostate region in the TRUS images, as inputs for building two fuzzy inference systems (FIS) to locate prostate carcinoma [4]. Up to six Gaussian membership functions are used per input parameter. One FIS distinguishes hypoechoic and hyperechoic tumours from the normal tissue. The other FIS segments isoechoic tumours from the normal tissue. However, to evaluate TRUS images with Scheipers' approach, there has to be prior knowledge of the type of tumour (whether hypoechoic/hyperechoic or isoechoic). Furthermore, the two FISs, proposed by Scheipers et al., require six and seven inputs, respectively. This incurs a high computational expense. In our work, only three parameters, each with two membership functions, are applied for the task. We will also examine how the spatial features could be best represented by fuzzy membership functions by introducing the novel notion of multi-dimensional fuzzy membership functions.

4.4 Chapter Summary

In this chapter, current tools for medical image segmentation are examined. The issue of improving upon the existing methods in identifying and localizing malignant tumour in ultrasound image is discussed.

Chapter 5
Architecture of the Proposed Automated Diagnostic System

In this chapter, the architecture of the proposed automated diagnostic system is presented. The primary goal of the proposed method is to automatically segment the malignant and benign tissue regions in TRUS images by simulating the manual analysis of an experienced radiologist. Some of the subcomponents of the system could also be used to enhance the local texture differences between the malignant region and the benign region to aid in the manual identification of malignancy.

The ultrasound images, used in the subsequent analysis, were obtained during clinical screening sessions by using an Aloka 2000 ultrasound machine with a broadband 7MHz linear transducer and a field of view of approximately 6 cm. Dr. D.B. Downey, an experienced radiologist, manually outlined the malignant and benign regions in the TRUS images. Manual segmentation was adopted as the gold standard in evaluating the degree of inter-operator agreement between the manual approach and the proposed approach. Before the tissue segmentation by the new approach, the contour of the prostate was segmented by using the deformable model approach [1]. The contour segmented prostate was used as the input to train and evaluate the automated tissue segmentation system.

The new method is proposed to capture the texture and spatial information in the TRUS images that have been identified in Chapter 3 as being important in discriminating between the malignant and benign regions. The main diagnosis feature is based on the local texture variations, whereas spatial information is used as the supporting feature.

In this thesis, several distinct and novel approaches are explored to extract the texture and spatial features. Each of these approaches presents certain tradeoffs. For texture feature extraction, the classical co-occurrence matrix approach is contrasted with novel

methods such as the RNN and the wavelet based texture feature extraction filter. For constructing the spatial feature, the statistical spatial distribution of malignancy was compiled with the atlas-based reference approach and represented as 2D and 3D fuzzy membership functions.

The proposed system provides useful diagnosis results at several levels. Texture based features, by themselves, could be used to identify suspicious regions without regards to spatial likelihood. Thus, by itself, the texture based feature provides diagnosis with relative high sensitivity. To obtain a binary segmentation and classification of the malignant and the benign regions using only texture based features, thresholding is applied to the specific texture feature space. In the case of the wavelet based texture feature extraction filter, along with the binary segmentation, the wavelet coefficient details at fine scales provided by this filter also enhances the visual distinctions between the malignant and benign tissues in the TRUS image. This could help radiologists to identify the malignant regions manually.

The spatial information is used as a supporting feature and it is only applied in conjunction with the textural feature. In this work, the statistical spatial distribution of malignancy is represented as 2D or 3D fuzzy membership functions. To obtain the 2^{nd} level binary segmentation of malignant and benign regions, the texture feature and spatial feature are synthesized with a fuzzy inference system. The system provides a continuous output between 0 and 1, indicating the likelihood of malignancy. A threshold between 0 and 1 is selected based on operating conditions, which results in the binary segmentation. The overall architecture of the proposed system, with its inputs and outputs, are presented in Figure 10.

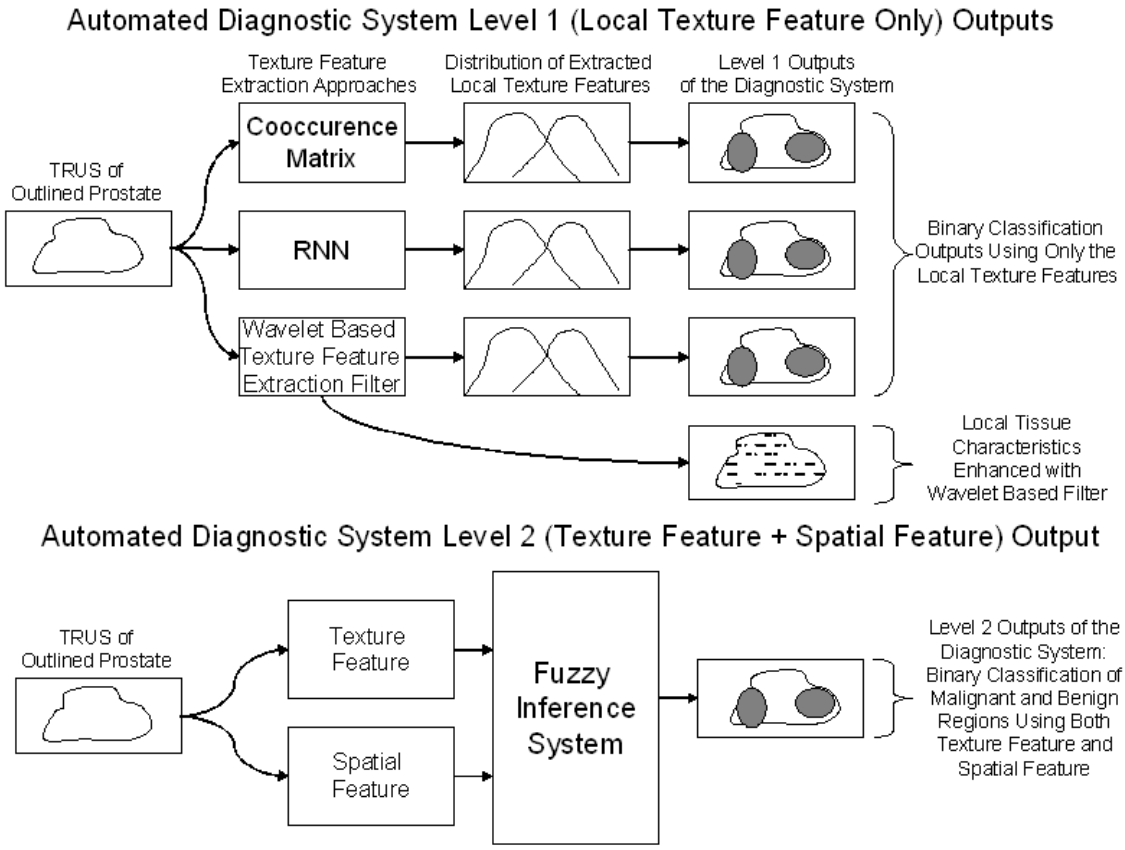

Figure 10. System Overview.

The incorporation of spatial information eliminates suspicious regions with similar local texture to malignant regions but located in regions unlikely to be cancerous according to the statistical spatial distribution of malignancy. This improves the specificity of the diagnosis.

To provide architectural scalability and to allow the operator to take advantage of the individual feature extraction approaches, the operator is allowed to select which of the available approach to apply when constructing the texture or spatial features (Figure 11). The texture or spatial feature is then constructed using the selected method and represented as fuzzy membership function sets. Appropriate inference rules are then chosen for the current set of texture and spatial features and fuzzy inference is applied to obtain the 2nd level automated diagnostic results.

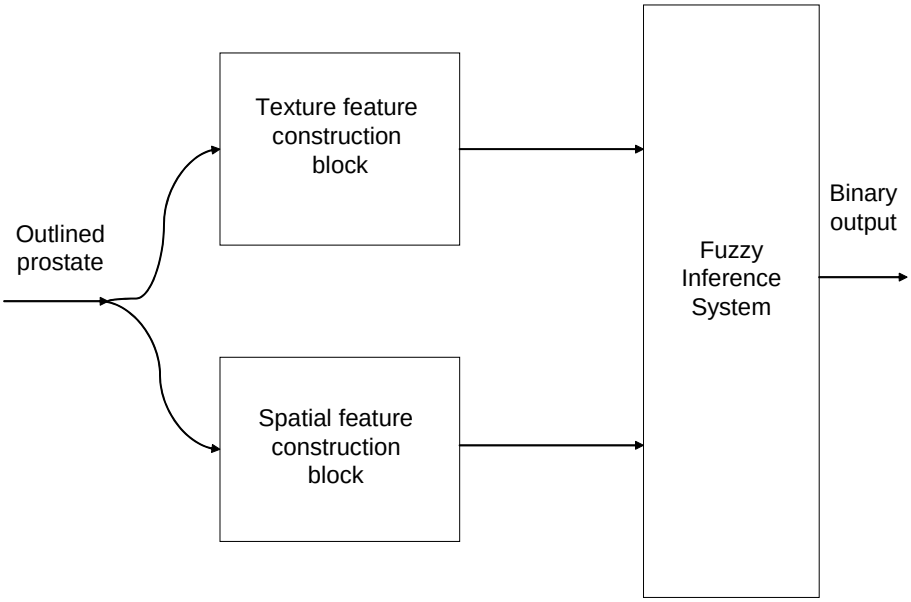

Figure 11. System Architecture: Fuzzy Inference System with Replaceable Feature Construction Blocks.

Some of the subcomponents of the system, such as the RNN, require training with the manually segmented data. After the training is completed, the system is evaluated with a different set of TRUS images.

In subsequent chapters, the various novel approaches implemented to extract the local texture feature and the spatial feature are explained in detail.

Chapter 6
Extraction of Novel Local Texture Features

In Chapters 3 and 4, the local texture features have been identified as one of the key characteristics which both radiologists and existing automated systems alike have used to predict the location of malignancy in ultrasonic TRUS images. In this Chapter, the definition of local texture, the notion of applying local texture features to identify biological tissues in medical images and several novel approaches to extract the characteristic textures of the malignant tissue and the benign tissue within the ultrasonic prostate image are explored in detail.

6.1 Definition of Local Texture and Texture Feature Extraction

The definition of texture in images is vague. Currently, there exist no standard to characterize a specific texture although both statistical and spectral texture measurement approaches exist. Regular textures are usually defined by a texture primitive or textel (orientation parameter) of a specific size (scale parameter) that is repeated at a certain spatial frequency (periodicity parameter). Simple statistical approaches include applying the standard deviation, uniformity, and entropy measures to the local histogram. These measures effectively describe the coarseness or smoothness of the texture [29], thus characterize the periodicity parameter well, but not explicitly the orientation and scale parameters. Spectral approaches such as the Fourier spectrum analysis are effective at characterizing the periodicity parameter. However, the results of the transform are not localized in the spatial domain, thus the method is ineffective when identifying texture regions in an image. Textural feature extraction techniques such as the grey-level co-occurrence matrix (GLCM) and the random pulsed neural network (RNN) capture both the orientation and periodicity characteristics of a texture. To capture the local texture features

in the ultrasonic images of the prostate, the co-occurrence parameters have been applied by Scheipers et al. in [4].

The problem with these textural feature extraction techniques is that they could not effectively distinguish between textures when the texture primitives are located at different scales. This is in part due to the restriction that these approaches could not adaptively vary the size of the texture capturing window to ensure that a single textel is exactly captured within that window. Another difficulty when applying these texture feature extraction tools is that it is usually necessary to reduce the number of grey-levels in order to obtain meaningful results. However, reducing the grey-levels in the texture also imply that the uniqueness of the texture characterized is diminished. Furthermore, intensity inhomogeneity or illumination variation usually occurs at a coarse scale whereas the textures of interest are usually located at a finer scale. The co-occurrence matrix and RNN approach both explicitly capture all pixel intensity variations as local texture variations, which is incorrect if the intensity homogeneity within the region of interest assumption does not hold.

Multi-resolution analysis has been shown to be effective for texture segmentation tasks. Laine and Fan used pixel intensities at various scales of detail derived from the wavelet decomposition as inputs to a two-layer feedforward neural network to classify 25 natural textures with almost perfect accuracy [19]. The Wavelet decomposition projects the image on to orthonormal basis (periodicity parameter), called Wavelets, which could be stretched or compressed (scale parameter). Furthermore, the projection onto the basis is usually accomplished in the horizontal, vertical, and diagonal directions (orientation parameter). Therefore, intuitively, wavelet decomposition should be able to uniquely characterize textures as it takes into account of all of the orientation, scale, and periodicity characteristics of a texture. In

the area of diagnostic medical imaging, the wavelet approach has been applied to liver and breast cancer detection in ultrasound images and mammography [30][31][32].

The basis for this analysis lies in the argument that most relevant tissue textures are to be located at specific and finite resolution ranges, where the texture at other resolutions ranges are most likely noise or other scales of detail that are not relevant to the analysis at hand. Wavelet decomposition provides the tool with which to zoom into the resolution of interest. This notion is supported by the works of Francos et al., who argued that any complex textures could be separated into two mutually orthogonal spatially homogenous components, one which is deterministic and one which is purely nondeterministic [33]. The wavelet decomposition inherently separates a texture into orthogonal components (subbands), some of which are descriptive of the texture, while others are nondeterministic.

In many image processing applications, it is important to distinguish between regions containing different textures. This could be accomplished if the textures in the regions of interest are characterized in some fashion. The role of the textural feature extraction filter is to map different textures to minimally overlapping distributions in the feature space. This problem is illustrated in Figure 12. The prostate region of the TRUS image is used as input into the filter. Texture feature values are obtained at the output of the filter, which would ideally have non-overlapping malignant and benign distributions for good classification results.

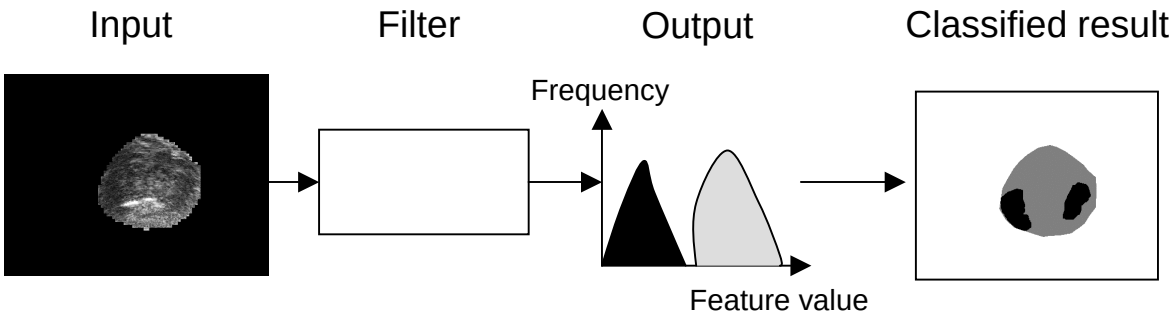

Figure 12. Mapping Textures to Linearly Separable Feature Space.

In subsequent sections, the co-occurrence matrix, RNN, and wavelet based approach are applied to extract the local texture features in prostate TRUS images. The class separability of the extracted feature using each approach is compared and discussed.

6.2 Co-occurrence Matrix for Texture Feature Extraction

The grey-level co-occurrence matrix (GLCM) belongs to the statistical approach of describing textures. A simple way to describe the texture is to use the statistical moments of the grey-level histogram of an image. However, this approach carries no information regarding the relative positions of the pixels as spatial information is lost in the 1-D histogram. To correct for this deficiency, an approach called the gray-level co-occurrence matrix [29] is implemented.

In the following section, the idea behind the co-occurrence matrix is briefly described. Let X be a $n \times n$ image matrix with grey-levels 0 and 1 as follows:

0	1	1	0
1	1	1	1
1	0	0	1
1	1	0	1

Let P be the position operator and A be a $k \times k$ matrix (where k is the number of grey levels) whose element a_{ij} is the number of occurrences of pixels of grey level i with respect to pixels of

grey level *j*. The position operator P determines the relative positions of the pixels to measure. For example, if P is set to (1,1) (meaning one pixel to the right and one down) then A would become:

1	2
2	4

which indicates that there are 1 occurrence of the grey level 0 at position (1,1) from pixels with grey level 0, 2 occurrences of the grey level 1 at position (1,1) from pixels with grey level 0, 2 occurrences of the grey level 0 at position (1,1) from pixels with grey level 1, and 4 occurrences of the grey level 1 at position (1,1) from pixels with grey level 1.

The grey-level co-occurrence matrix C is derived from dividing every element of the matrix A by *n*, the total number of joint pairs (*n*=9 in previous example). By selecting different Ps, different texture patterns could be detected. To analyze textures using the grey-level co-occurrence matrix, a set of features calculated from the matrix are generally used. Some of the GLCM features are defined as follows:

1. Energy or Uniformity

$$\sum_i \sum_j c_{ij}^2 \qquad \textbf{Equation 4}$$

2. Inertia or element difference moment of order 2

$$\sum_i \sum_j (i-j)^2 c_{ij} \qquad \textbf{Equation 5}$$

3. Entropy

$$-\sum_i \sum_j c_{ij} \log_2 c_{ij} \qquad \textbf{Equation 6}$$

4. Homogeneity

$$\sum_i \sum_j c_{ij} / (1 + (i - j)^2) \qquad \textbf{Equation 7}$$

The GLCM was used by Scheipers et al. to extract the tissue texture information in ultrasound images in their attempt to classify the malignant and benign tissues [4]. The GLCM features evaluated in the Scheipers paper include the angular second moment, contrast, correlation, dimension, inverse difference moment, kappa, peak density, variance, and the SNR. However, the relative merit of each GLCM feature and the effect of selecting the position operator P were not analyzed in depth.

In Section 6.5.1, the ability of GLCM features to segment textures is examined with synthesized texture images. In Section 6.6.1, GLCM features are applied to map textural properties of malignant and benign tissues in TRUS images into a linearly separable space. The performance of the GLCM as a texture feature extraction tool is used as a measuring tool to examine the additional benefits brought by novel algorithms introduced later in the section, such as the RNN and wavelet-based approaches.

6.3 RNN for Texture Feature Extraction

Gelenbe introduced the RNN in 1989 [34][35][36]. The method of RNN was introduced in Chapter 4 of this thesis. In 1996, Gelenbe et al. applied the RNN to segment the grey and white matters in MRI images of the brain [28], thereby experimentally proving the RNN's ability to capture the textural differences between the tissues in medical images. Ultrasound images contain speckle, which is absent in MRI images. Therefore, the local texture in different tissue regions in a TRUS image is likely to be affected by the speckle, and the segmentation performance of the RNN will not be as ideal as the MRI results.

If the size of the input pixel block is chosen as $n \times n$, each of the two RNNs are also to be constructed as an $n \times n$ grid of neurons. This is depicted in Figure 13. Each neuron is mapped to

the pixel at the same location in the $n \times n$ grid and interacts directly only with the other neurons in the four first order and four second order cardinal directions (N, NE, E, SE, S, SW, W, and NW).

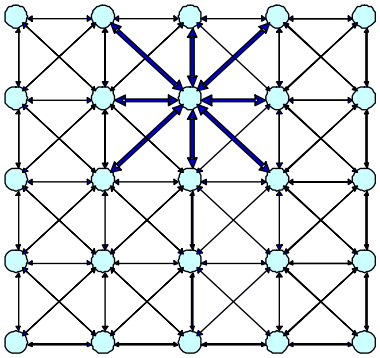

Figure 13. RNN Neuron Grid.

In the training phase, RNN1 is trained with data from the benign region and RNN2 is trained with data from the malignant region. The input to the RNNs consists of distinct 5×5 blocks of pixels with each pixel having scaled intensity values between 0 and 1 (scaled from the original range of 0-255). The histogram of the input pixels is equalized with a base histogram to avoid large contrast variations between the images. The base histogram is selected from one of the training images that is judged by the operator to have the maximum visual separation between the malignant region and benign region. The desired output of each neuron is set as the scaled intensity of the associated pixel.

When the image blocks are evaluated, the output of each RNN is the sum of the squared errors for each block under evaluation. A lower sum of the squared error of one RNN, compared to that of the other, indicates that the block is more texturally similar to the region that the first RNN is being trained with.

In Section 6.5.2, the RNN is applied to segment synthesized Bordatz textures. In Section 6.6.2, RNN is applied to map textural properties of malignant and benign tissues in TRUS images into a linearly separable space.

6.4 Wavelet-based Texture Feature Extraction Filter

In this section, a texture feature extraction filter is implemented based on wavelet decomposition. Parameters of the non-linear filter could be adjusted such that it maps characteristics of a texture onto a narrow distribution band on a single texture feature space. This mapping is accomplished with the goal of maximally linearly separating the band of feature values belonging to different textures in the texture feature space. The filter uniquely characterizes a subset of textures by their scale responses (its local feature distribution over a range of Wavelet decomposition scales). The scale responses could be applied to distinguish different textures appearing in the same image. The optimally linearly separable feature space also allows researchers to easily judge whether texture features provide good class separation for their specific image processing application. It is found that the proposed method minimizes the effect of intensity inhomogeneity on distorting the local texture of images. In this section, it is demonstrated that the wavelet decomposition reveals details in the malignant and benign regions in TRUS images of the prostate which correlate with their pathological representations. The proposed filter is used to extract texture features which provide separation of the malignant region and the benign region in the feature domain. Thresholding could be applied to the extracted texture feature to obtain an automated diagnosis result with high sensitivity. The extracted texture feature could also be used as an input to the FIS for the second stage automated malignancy region classification. It is also shown that the wavelet decomposition could also be applied directly to the TRUS images to enhance the visual distinction between the malignant and benign regions. This could be used by radiologists as a supplementary tool for making manual classification decisions.

In the subsequent subsection, the proposed design to characterize textures is presented. In subsection 6.4.1, the idea behind using wavelet-based texture characterization is validated. In

subsection 6.4.2, the generalized wavelet-based texture feature extraction filter is designed and tested on Bordatz images. In subsection 6.4.3, the wavelet-based texture feature extraction filter is adapted to the ultrasonic prostate cancer detection problem.

6.4.1 Texture Characterization with the Wavelet-based Approach

Complex textures rarely have regular patterns. Thus, it is difficult to characterize such textures by orientation, scale and periodicity descriptors. However, all textures could be viewed as a combination of sub-textures on several scales and orientations (Figure 14). The HL, LH, and HH subbands represent the horizontal, vertical and diagonal components of the decomposition respectively. The subscript represents the scale of the decomposition, with 1 being the coarsest scale.

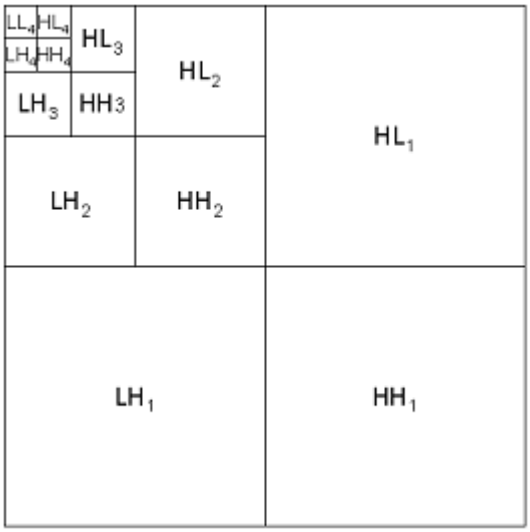

Figure 14. Subbands of the Wavelet Decomposition.

When textures are decomposed into components on different scales, regular sub-texture patterns characterizing the original texture on a particular scale might emerge. In the example in Figure 15, the original roof tile texture is decomposed into its components on four scale levels, from the finest to coarsest, regular patterns characterizing this texture at decomposition levels 3

and 4 in the horizontal direction (HL_3, HL_4) could be distinguished, whereas the presence of noise is noted in the other subbands.

Figure 15. Decomposing the Roof Tile Texture to Reveal the Regular Sub-textures at Different Scales (Refer to Figure 14 to match the subbands).

The decomposition of the texture in Figure 15 reveals some regular sub-textures on certain levels of the decomposition. However, at other levels of the decomposition, the sub-textures are irregular. Therefore, the major challenge in characterizing a complex texture consist of: a) identifying the scales at which its sub-textures are regular and could be characterized, taking care of the scale characteristic of the texture; and b) finding a textural feature measure which would take into account the orientation and periodicity characteristics of the texture. The proposed approach uses Wavelet decomposition to aid in the characteristic scale identification

and to capture the periodicity feature of the texture. For the generalized texture feature extraction filter (6.4.2), local energy will be calculated to capture the orientation of the texture primitives. When the filter is adapted to the prostate ultrasound image problem (6.6.3), local texture characteristics of the malignant tissue and the benign tissue will be used to encapsulate the orientation of the texture primitives.

6.4.2 Implementation of Generalized Texture Feature Extraction Filter

The proposed non-linear filter to extract textural features consists of three levels of sub-filters (**Figure 16**).

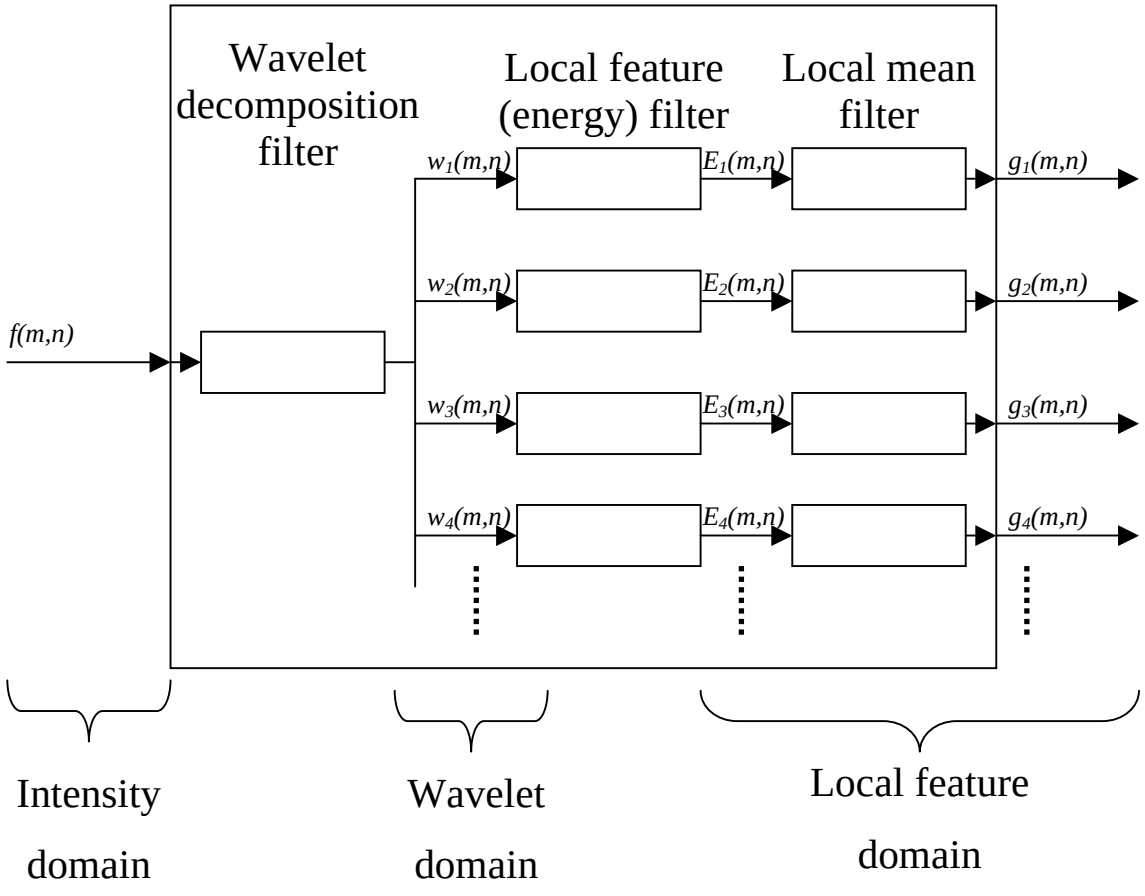

Figure 16. High Level Diagram of the Proposed Textural Feature Extraction Filter.

The first level of the proposed filter consists of a wavelet decomposition sub-filter, which transforms the original image in the intensity domain to wavelet decomposition details $w_i(m,n)$ in the wavelet domain. The subscript i represents the different scale levels of the wavelet decomposition with i=1 being the finest scale. The wavelet decomposition details are then passed through a bank of local feature sub-filters. In this work, energy is the local feature calculated. The local feature sub-filters maps the wavelet decomposition details to the local feature domain, while keeping the local feature values localized in the spatial domain. The local feature values at each scale level are then averaged by a local window to compress the range of local feature values in each texture region. The local feature values at different scales of the wavelet decomposition form the output of the filter and are used to characterize and identify the individual textures in the spatial domain. The following section describes the different levels of sub-filters in more detail.

6.4.2.1. Wavelet Decomposition Sub-filter

The wavelet decomposition expresses the image data as a superposition of scaling functions, which present a coarse representation of the image, and wavelets, which represent the details of the image. The common expression for the discrete wavelet transform (DWT) in 2-D is as follows:

$$f(m,n) = \sum_k \sum_l c_{i\max}(k,l) 2^{i\max/2} \varphi(2^{i\max/2} m - k, 2^{i\max/2} n - l) +$$

$$\sum_k \sum_{i=1}^{i\max} d_i(k) 2^{i/2} \psi(2^{i/2} m - k) + \sum_l \sum_{i=1}^{i\max} d_i(l) 2^{i/2} \psi(n - l) + \qquad \textbf{Equation 8}$$

$$\sum_k \sum_l \sum_{i=1}^{i\max} d_i(k,l) 2^{i/2} \psi(2^{i/2} m - k, 2^{i/2} n - l)$$

where $c_{i\max}(k,l)$ are the approximation coefficients, $d_i(k,l)$ are the difference coefficients, $\varphi(m,n)$ represents the scaling function and $\psi(m,n)$ represents the wavelet. The term in the first line of Equation 8, on the right side of the "equal sign", represents the approximation components. The two terms in the second line represents the vertical and horizontal detail components at all scales from i=1 to i=i_{max}, and the term on the bottom line represents the diagonal detail components at all scales.

For the scaling function and the wavelet to form a basis representing the image data, the recursion equations need to be satisfied.

$$\varphi(m,n) = \sum_u \sum_v s(u,v)\sqrt{2}\varphi(2m-u,2n-v) \qquad \textbf{Equation 9}$$

$$\psi(m,n) = \sum_u \sum_v z(u,v)\sqrt{2}\varphi(2m-u,2n-v) \qquad \textbf{Equation 10}$$

where $s(u,v)$ represents the scaling function coefficients and $z(u,v)$ represents the wavelet coefficients. To satisfy the non-redundancy and completeness constraints, Equation 11 must be satisfied,

$$z(m,n) = (-1)^m (-1)^n s(M-1-m, N-1-n) \qquad \textbf{Equation 11}$$

where $s(m,n)$ is a matrix of finite size *MxN* and *M*, *N* are even.

The proposed wavelet decomposition filter takes as input the original image and outputs the wavelet decomposition details at scale levels from i=1 (finest scale) to i=p, where p is the coarsest scale level required to describe the texture. The wavelet decomposition output $w_i(m,n)$ at a specific scale level i is the average of the wavelet decomposition detail differences in the horizontal, vertical, and diagonal directions at that scale level. The wavelet decomposition is

accomplished with the discrete filter D9 from Daubechies [37]. The equation describing the wavelet decomposition filter for scale level *i* is as follows:

$$w_i(m,n) = \frac{1}{3}[\sum_k d_i(k)\psi(m-k) + \sum_l d_i(l)\psi(n-l) + \sum_k \sum_l d_i(k,l)\psi(m-k,n-l)] \quad \textbf{Equation 12}$$

where $d_i(k)$, $d_i(l)$, and $d_i(k,l)$ are the difference coefficients at scale level *i* in the horizontal, vertical, and diagonal directions respectively and $\psi(m,n)$ is the wavelet.

This filter is implemented with a DWT quadrature mirror filter (QMF) (Figure 17). To maintain the resolution at each scale, the filtered results are not down-sampled as is the norm in common QMF designs.

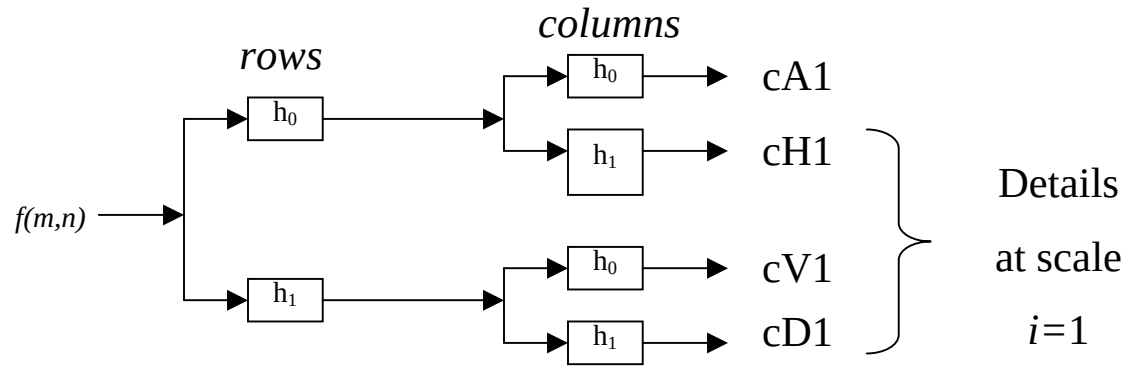

Figure 17. QMF for Implementation of Wavelet Decomposition.

The filter h_0 is a low pass filter with its impulse response characterized by the scaling function coefficients $s(m,n)$, while h_1 is a high pass filter with its impulse response characterized by the wavelet coefficients $z(m,n)$.

6.4.2.2. Local Feature Filter and Local Mean Filter

The local feature filter maps the wavelet decomposition details to the local feature domain and the local mean filter compresses the range of feature values characterizing a particular texture

at a specific scale so that multiple textures in the same image could be maximally linearly separated in the feature space at that scale. It has been previously proposed that energy pattern distributed in scale space represents texture in a unique way [19]. Therefore, we use the local energy measures as the local textural feature, which is written as

$$E_i(m,n) = \frac{1}{aN^2}\sum_{l=1}^{N}\sum_{k=1}^{N} | w_i(m-k, n-l) |^2 \qquad \textbf{Equation 13}$$

where N is the size of the local feature window in pixels, a is a constant used to normalize the energy value, and $w_i(m,n)$ is the wavelet decomposition details at scale i.

The orientation selectivity is stored within the tensor product of the high pass filters and low pass filters of the QMF [19]. Therefore, the energy measure will capture the orientation characteristic of the textures.

To reduce the range of local energy values that characterize a texture on a specific scale level, the local energy values are passed through a local mean filter written as

$$g_i(m,n) = \frac{1}{M^2}\sum_{l=1}^{M}\sum_{k=1}^{M} E_i(m,n) \qquad \textbf{Equation 14}$$

where M is the size of the local averaging window in pixels and $E_i(m,n)$ represents the local energy at scale i.

In Section 6.5.3, the wavelet-based texture feature extraction filter is applied to segment synthesized Bordatz textures. In Section 6.6.3, this filter is adapted to map textural properties of malignant and benign tissues in TRUS images into a linearly separable space.

6.5 Applying GLCM, RNN and Wavelet-based Texture Feature Extraction Filter to Segment Synthesized Bordatz Textures

Bordatz textures are widely used to test the performance of texture segmentation algorithms. Figure 18 is synthesized from four Bordatz textures and is used for preliminary evaluation of the texture segmentation algorithms examined in this thesis, namely the GLCM, the RNN, and the wavelet-based texture feature extraction filter.

Four distinct natural textures are selected from public archives. The textures are quantized at 256 grey-levels and are divided into sub-samples of size 100×100. The sub-samples are then synthesized to form an image containing all four textures.

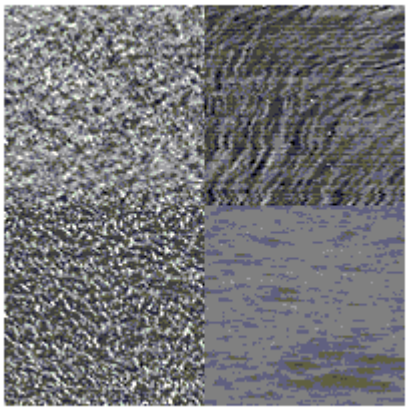

Figure 18. Synthesized Image Containing the Four Textures to be Characterized (Texture 1—Top Left, Texture 2—Top Right, Texture 3—Bottom Left, Texture 4—Bottom Right).

Texture 1 and Texture 3 are selected based on their orientation, scale, and periodicity similarities. Texture 4 is selected to study the effect of intensity inhomogeneity on the characterization of textures (the intensity inhomogeneity is located at bottom right of the sub-sample).

6.5.1 Applying GLCM to Segment Bordatz Textures

The GLCM of the synthesized texture image in Figure 18 is calculated with the following parameters: window size=10×10, X_{step}=1, Y_{step}=1 (diagonal 1,1 co-occurrence), 256 grey levels. The resulting energy, inertia, entropy, and homogeneity features are represented in Figure 19.

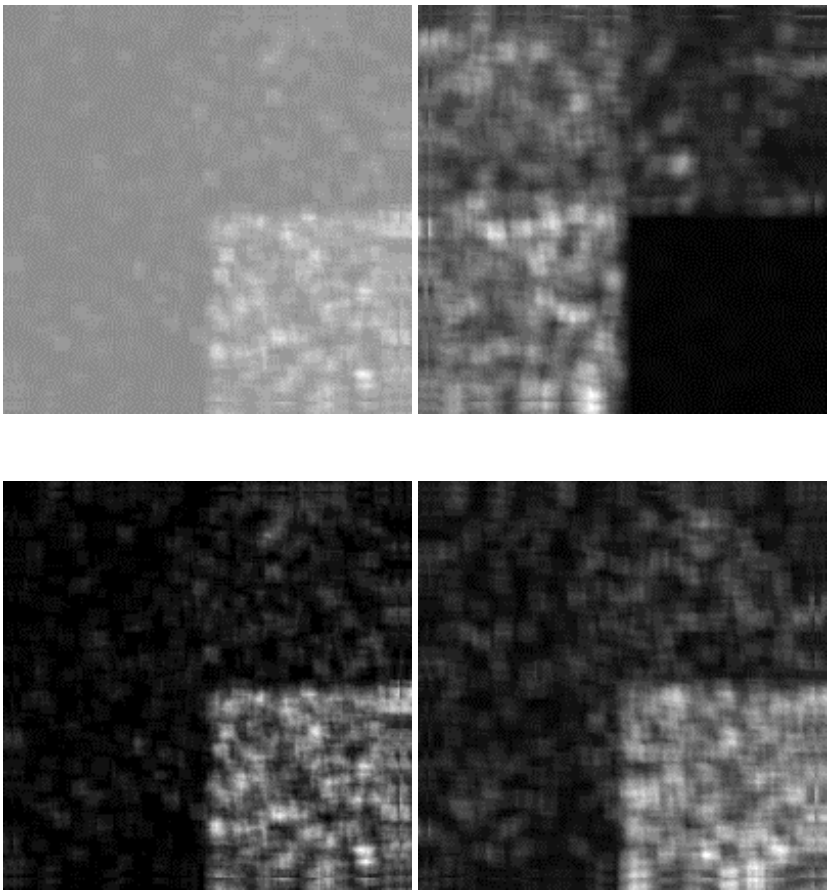

Figure 19. GLCM Energy (top left), Inertia (top right), Entropy (bottom left), and Homogeneity (bottom right) Features.

From Figure 19, it could be visually determined that the inertia feature provides the best separation amongst the four selected textures. The normalized histogram for the inertia feature is displayed in Figure 20.

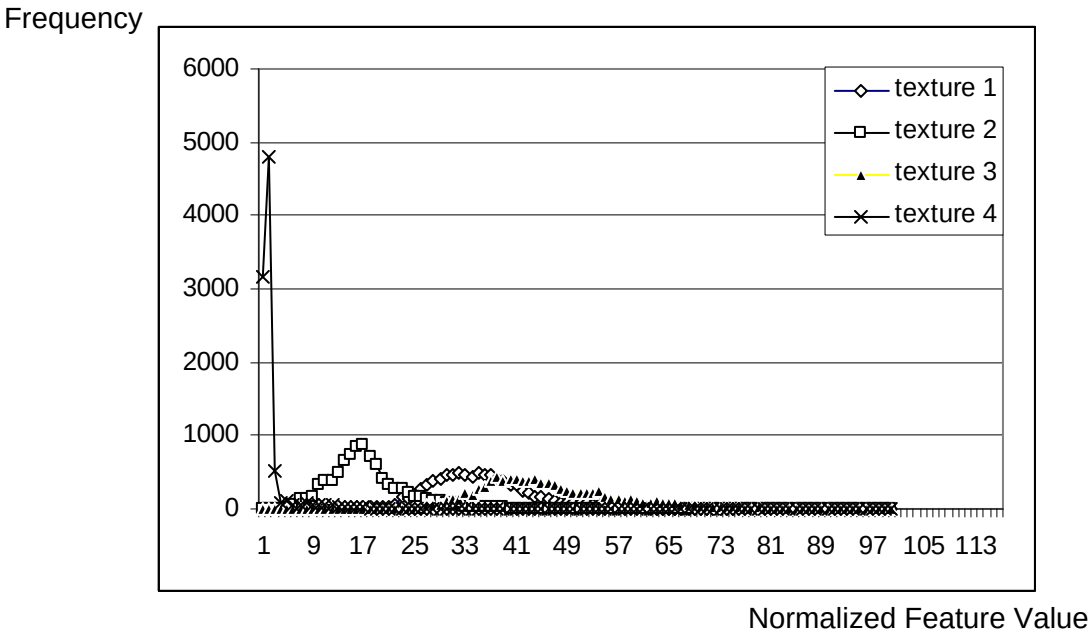

Figure 20. Normalized Histogram of the Inertia Feature.

Analyzing Figure 20, the valleys of the histogram separating the textures are located at 5, 25, and 40. Applying hard thresholding as the method of classification at these values on the inertia feature, the segmentation result in Figure 21 is obtained. The classification accuracy is evaluated at 78%.

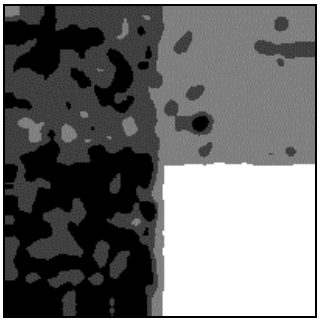

Figure 21. Segmentation Result of the GLCM Inertia Feature with Hard Thresholding.

6.5.2 Experimental Results of RNN Method on Segmenting Bordatz Textures

The RNN segmentation approach is tested by using natural texture images to resolve issues such as how to appropriately post-process the output of the RNN to improve the segmentation result and which size of input block is optimal for capturing the textural differences between the regions.

Four RNNs are trained with each of the textures in Figure 18. In the evaluation phase, the resulting segmented blocks, which are not connected to another segmented block of the same region in any of the eight first and second order cardinal directions, are likely the result of the noise within the original image. A self-devised filter that is similar to morphological dilation is used to remove all the unconnected blocks as shown in Figure 22 (a). This filter is implemented at the block level and converts the label of a particular block, if the label is discovered to be inconsistent with the labels of the surrounding blocks. This filter, along with the use of a median filter, results in a more contiguous segmentation of the four texture regions. This is displayed in Figure 22 (b). Another variable in determining the training methodology is the size of the input block. It is found that a smaller input block results in a finer contour along the edge of the regions. However, more noise results in the interior of the regions. The results from 4×4 and 5×5 input blocks are contrasted in Figure 23.

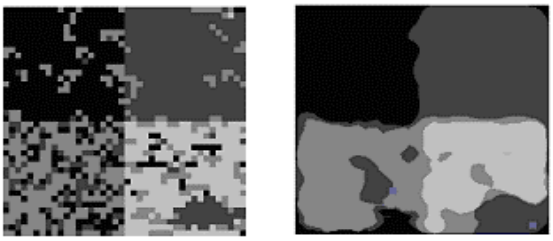

Figure 22. (a) Result of RNN (After Filtering Out the Unconnected Blocks), and (b) Median Filtering of Result in (a).

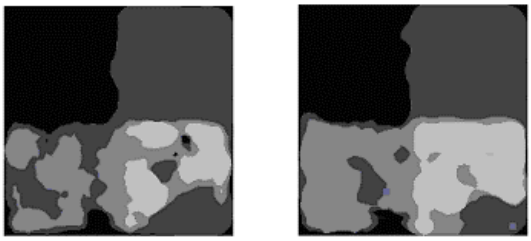

Figure 23. Effect of Size of Input Block: (a) Result From 4×4 Input Blocks, and (b) Result From 5×5 Input Blocks.

The post-processing procedure, described in this section, is followed for the TRUS image evaluation. For a more contiguous segmentation result, a 5×5 input block size is selected for the training and evaluation of the TRUS images. This texture feature extraction approach results in a classification rate of 77%.

6.5.3 Results of the Wavelet-based Texture Feature Extraction Filter When Applied to Bordatz Textures

In this sub-section, the proposed wavelet-based textural feature extraction filter is applied to segment the textures in Figure 18. The characteristics of the filter and how parameters of the filter could be adjusted to optimally linearly separate the texture distributions in feature space are discussed.

Characterizing and identifying a specific texture using the proposed textural feature extraction filter involves four steps as follows:

1. Pass sub-samples of textures to be identified into the filter to map their characteristics into the local feature domain. Local feature distributions for each texture at all scales are obtained.

2. Identify the scale level at which the local feature ranges are maximally linearly separable as the characteristic scale for the texture set. Identify the size of the local feature window that optimally linearly separates the feature distributions.
3. Pass images containing the textures to be discriminated into the filter. The image is mapped to the local feature domain with the local feature values localized in the spatial domain.
4. On the characteristic scale for the texture set, compare the local feature values at each discrete spatial location obtained in 3 with the local feature value distributions for each texture at that scale obtained in 1. Each discrete spatial location is assigned the texture label associated with that texture's local feature distribution that the local feature value of the spatial location is judged to belong to the most. The simplest classification approach, thresholding, is applied to demonstrate the linear separability of feature space obtained by the proposed approach.

To characterize each of the four textures, we pass 100×100 sub-samples of the textures into the filter to obtain their local feature value distributions at each wavelet scale. Figure 24 shows the wavelet domain representations of the textures at the four finest wavelet scales (at the output of the wavelet decomposition sub-filter). In Figure 25, the local feature distributions of the four textures on the four finest wavelet scales are displayed (output histogram of the local mean filter).

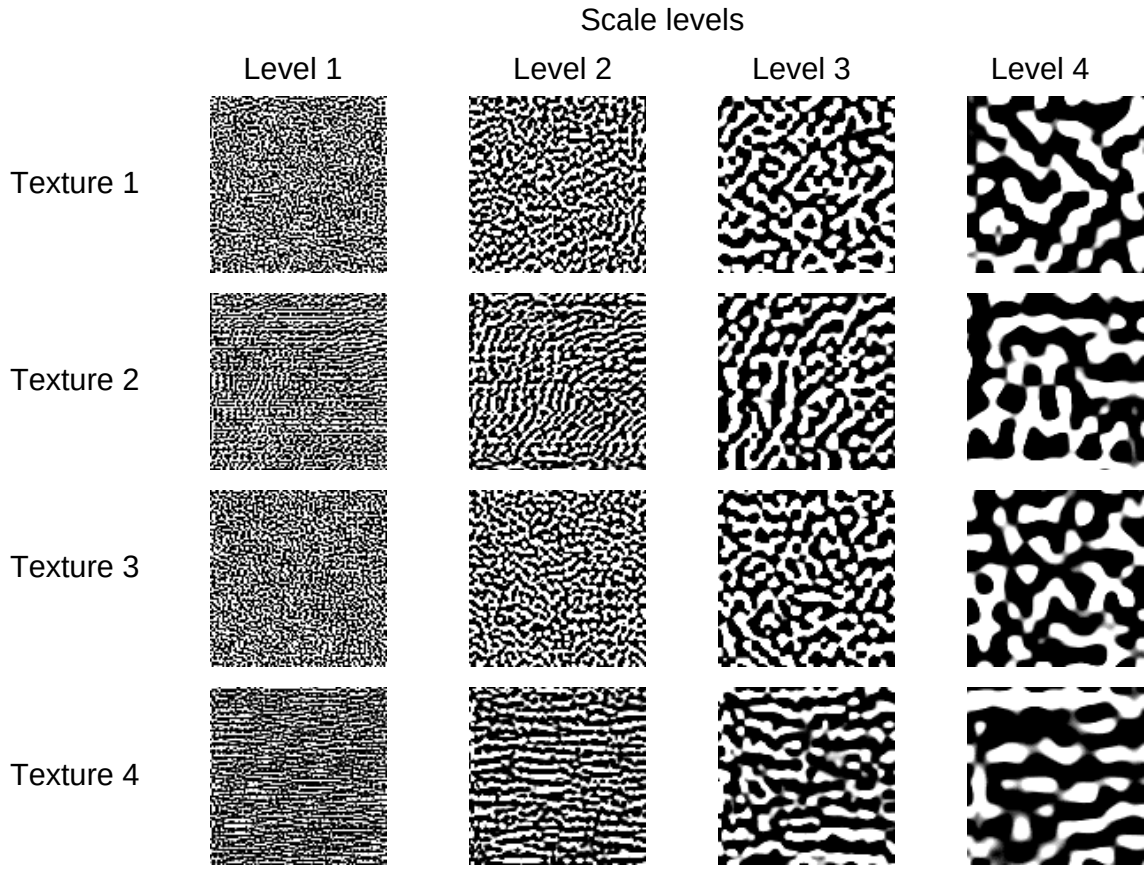

Figure 24. Wavelet Decomposition Sub-filter Output of the Four Texture Sub-samples at the Four Finest Wavelet Scales.

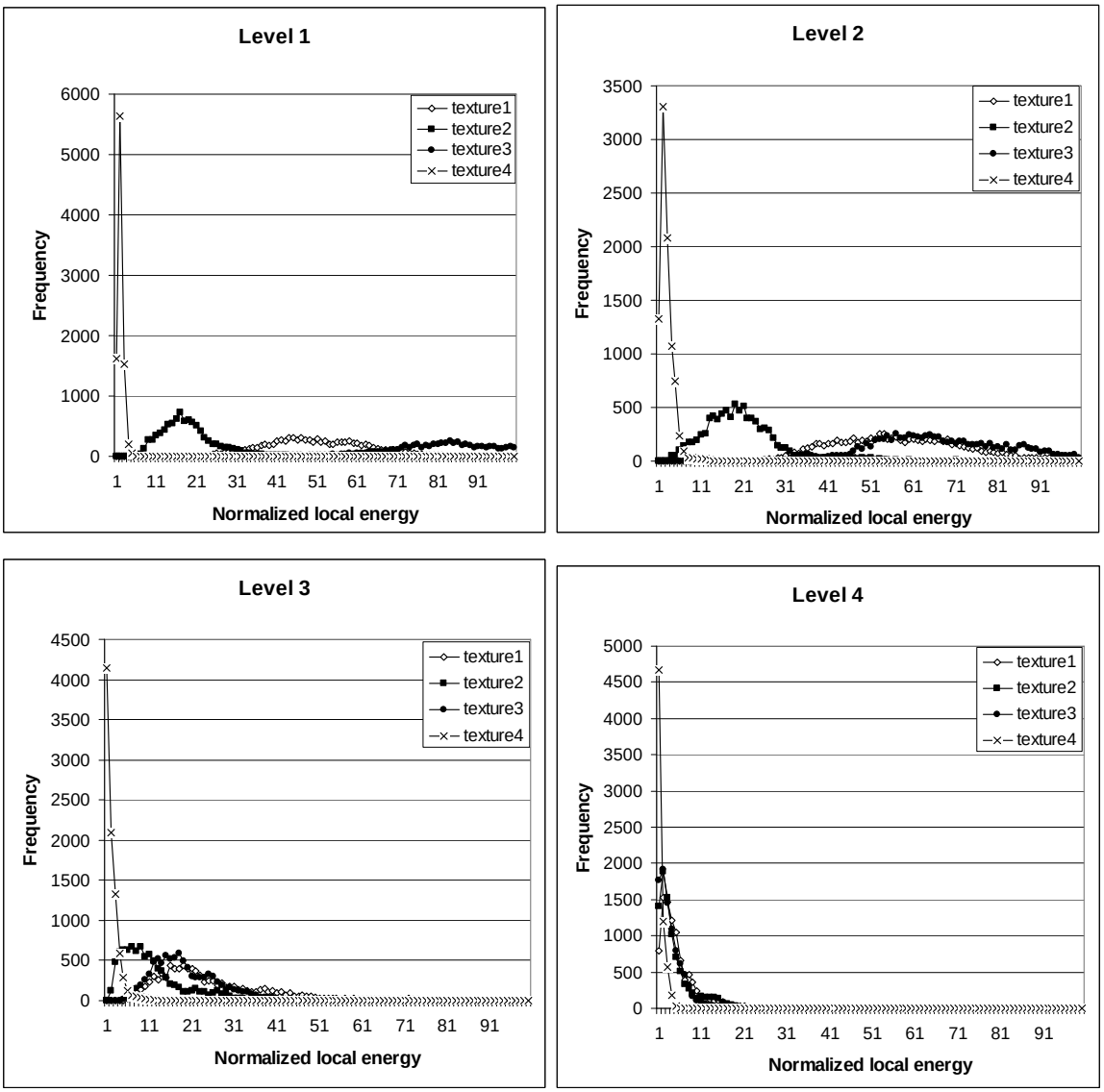

Figure 25. Local Feature Value Distribution for Four Textures at Four Finest Wavelet Decomposition Levels.

From Figure 25, we note that in this set of four textures, the level 1 decomposition details yields the optimally linearly separable local feature distributions. The local energy values could be viewed as representative of the graininess of the sub-textures. As the decomposition level increases, the sub-textures of the decomposition details become smoother, thus the normalized

local energy values are lowered. At higher decomposition levels, the feature value distributions for the textures start to overlap considerably and linear separability is reduced.

The feature value distributions of the four textures at different scales could be studied in more depth by plotting the minimum, maximum, and mode values in the distribution against the decomposition scales as in Figure 26.

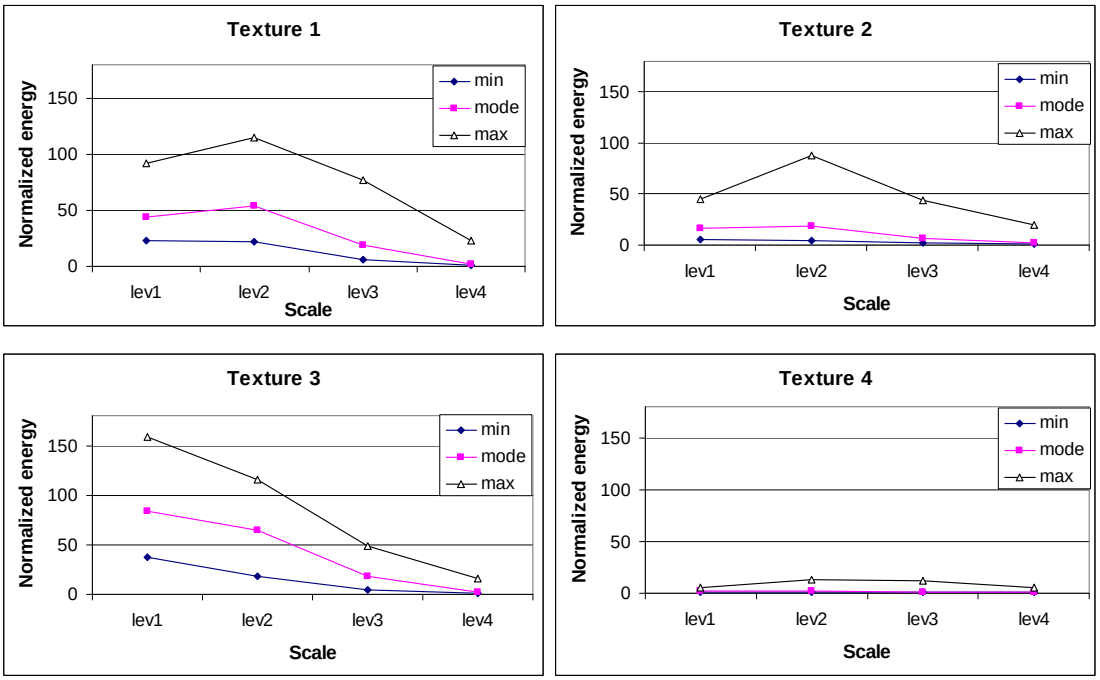

Figure 26. Scale Response of the Four Textures: Local Feature Distribution Range and Mode at Each Scale.

From Figure 26, notice that each of the four textures exhibits a unique scale response. The mode represents the value that occurs with the maxim frequency in the distribution at each scale and is unique to each texture at low decomposition levels. As the scale level increases, the mode peaks at a certain intermediate scale level and then decreases toward a low constant value. The range of the distributions, defined to be between the minimum and maxim values, are restricted to a well defined range at low scale levels. The range peaks at an intermediate scale level and drops off to a constant range close to minimum energy at high scale levels. The

scale at which the mode and the range peak could be interpreted as the scale at which that texture is optimally represented or is most visually distinguishing. However, whether this representative scale, when used alone, is suitable for distinguishing between the textures depends on the amount of overlap between the feature distributions of the textures to be distinguished on this scale. For these four textures, we identify scale level 2 as the characteristic scales for texture 1, texture 2, and texture 4 and scale level 1 as the characteristic scale for texture 3. We also identify scale level 1 as the optimally linearly separating scale level for this four texture set.

Other than the decomposition scale, another filter parameter that needs to be studied for optimal feature distribution separation is the size of the local feature window, *N*. In Figure 27, the histogram of the local features are plotted for local feature window of size 4×4, 6×6, 8×8, and 10×10. In Figure 28, the maximum, minimum, and mode values of each texture's feature value distribution at scale level 1 are plotted against the local feature window size.

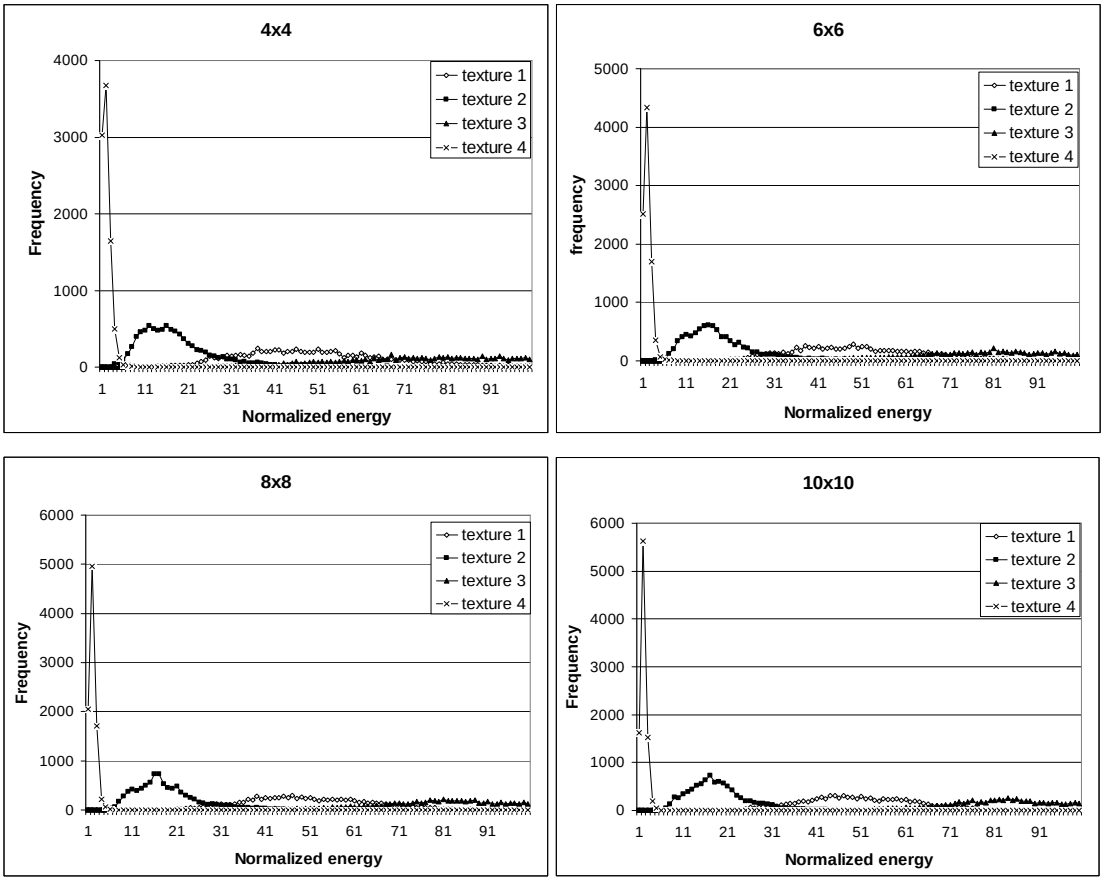

Figure 27. Local Feature Distributions Calculated with Different Local Feature Window Sizes.

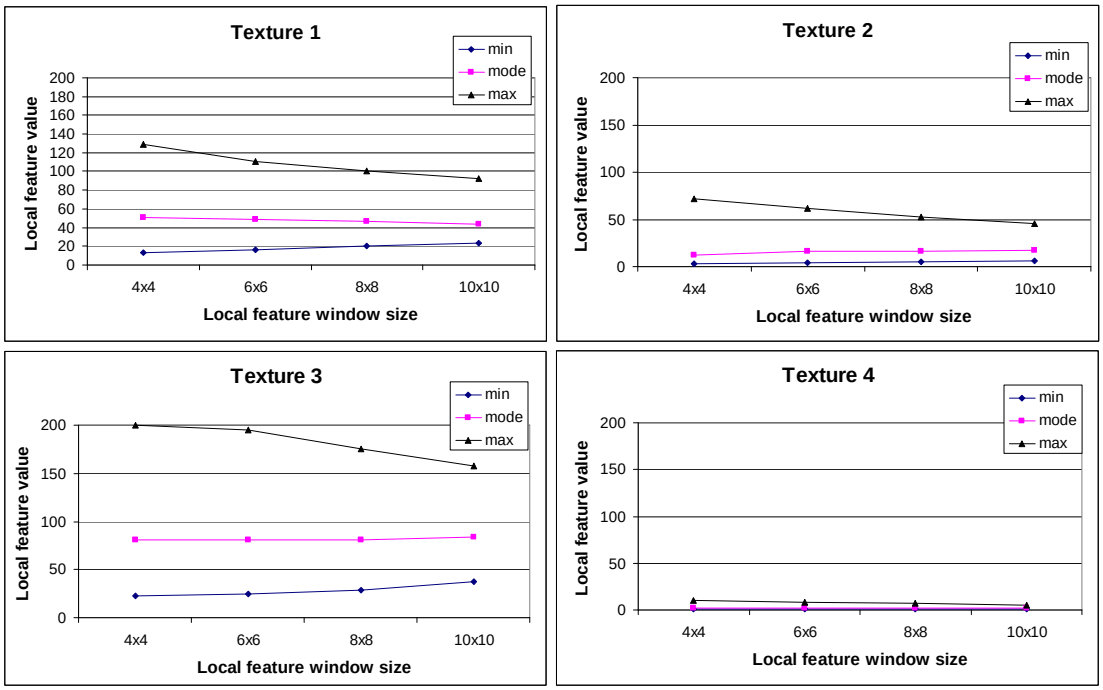

Figure 28. Maximum, Minimum, and Mode of the Feature Value Distributions Against the Local Feature Window Size for Four Textures at Scale Level 1.

From Figure 27 and Figure 28, it could be noted that the size of the local feature window, *N*, used to calculated the local feature values, does not affect the mode of the distribution. However, as *N* increases, the range defining the distribution narrows, making it easier to characterize and identify the texture as there is less overlap with the distribution of other textures. This is attributed to the observation that as the local feature window increases in size, it is more likely to capture the exact local feature value of the texture primitive, as the texture primitive of a complex texture is likely to be more irregular in a smaller local window. However, we could not set the local feature window size infinitely large as this would decrease the distinguishing ability of the feature values at or around texture boundaries. For this work, the local feature window size is set to *N*=10. Likewise, we can infer that the size of the local mean filter, *M*, also affects the range of the feature value distribution. As we increase *M*, the distribution range narrows and vice versa. *M* is set to 10 for the subsequent sections.

Now that we have characterized the four textures by their local feature distribution at different scales of the wavelet decomposition, we could proceed to identify these textures in a synthesized image containing all four textures (Figure 18). We decompose the synthesized image into its difference details at four scales by passing it through the wavelet decomposition sub-filter. The outputs of the sub-filter are displayed in Figure 29.

Level 1 decomposition difference details

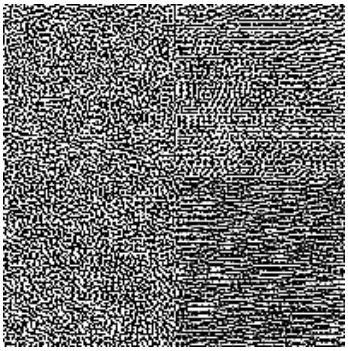

Level 2 decomposition difference details

Level 3 decomposition difference details

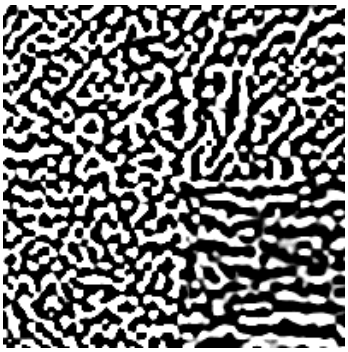

Level 4 decomposition difference details

Figure 29. Synthesized Image's Decomposition Difference Details at Different Scales.

As we have already identified level 1 of the decomposition details as yielding the maximally linear separable feature space, we pass the level 1 decomposition details into the local feature filter with window size 10×10. The result is then passed through the local mean filter. The outputs of the local feature filter and local mean filter are displayed in Figure 30.

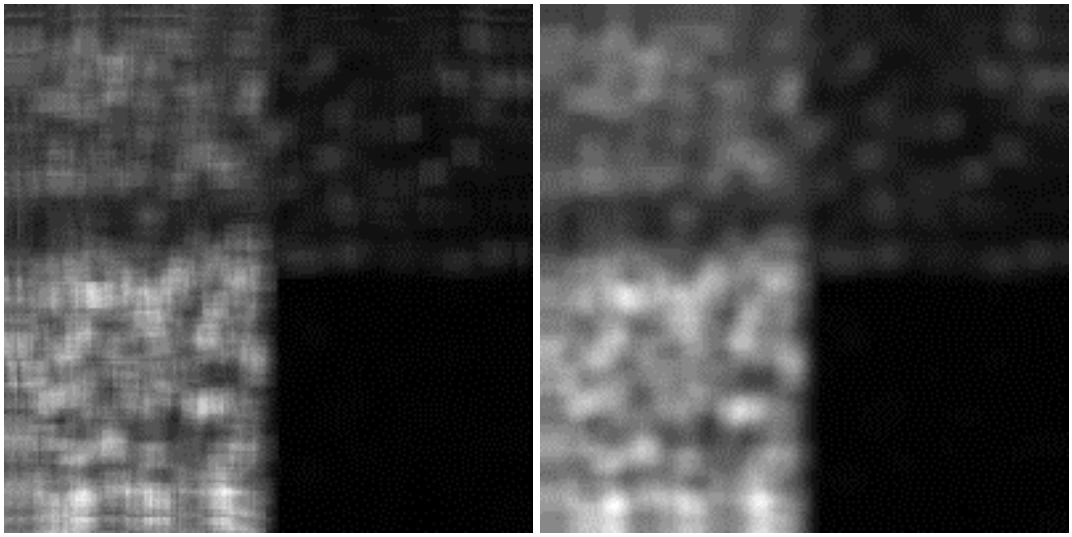

Figure 30. Outputs of the Local Feature Filter (left) and Local Mean Filter (right).

The histogram of the local feature values is displayed in Figure 31.

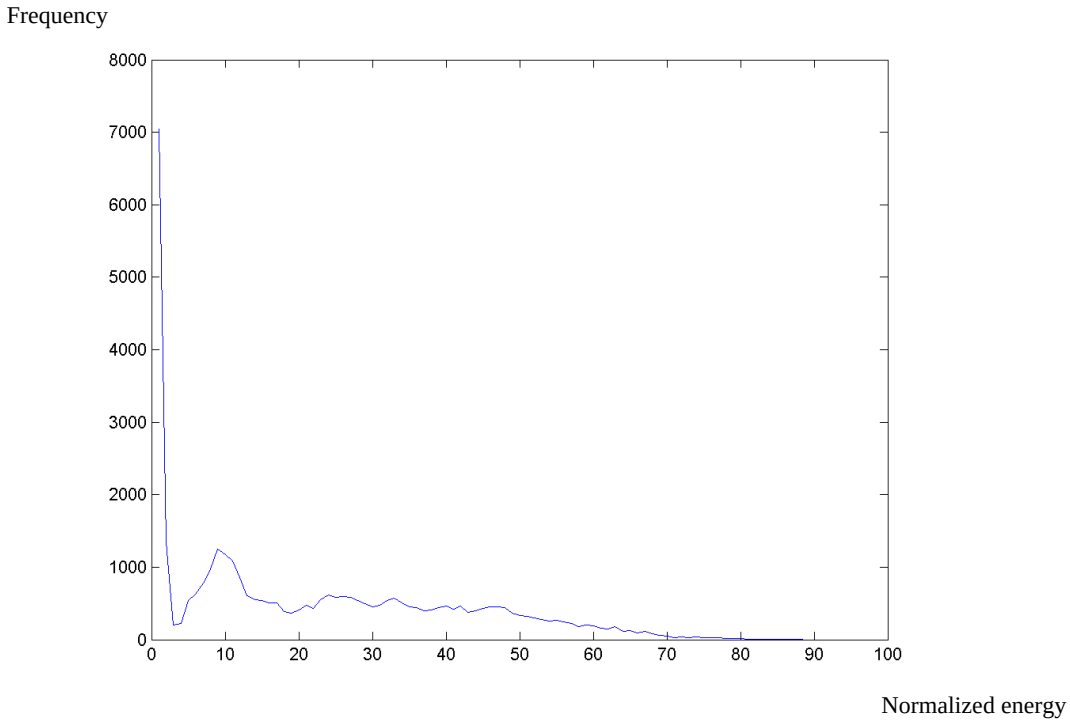

Figure 31. Histogram of the Local Feature Values for the Synthesized Image.

To demonstrate the linear separability of the textural feature extracted, we used the simplest linear classification approach, thresholding. We set hard thresholds at the crossings of adjacent

texture feature distributions in Figure 25 (level 1). The optimal thresholds are located at 6, 32, and 70 respectively. Applying thresholding, we obtain the classified image in Figure 32, where each identified texture is labeled by a constant grey-level (texture 1—grey level 128, texture 2—grey level 64, texture 3—grey level 0, texture 4—grey level 255). The classification rate is measured at 90%.

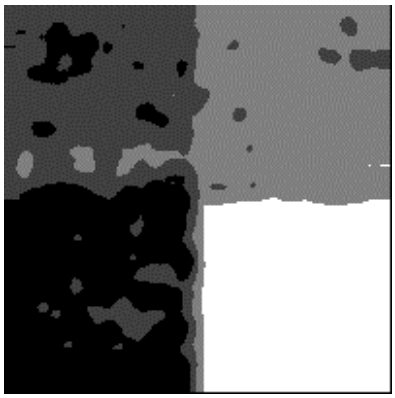

Figure 32. Classification Result Using Texture Feature Extracted by Proposed Filter and Hard Thresholding.

The classification results between the co-occurrence matrix, RNN, and proposed approach on the synthesized image are listed in Table 2.

Table 2. Classification Results of Co-occurrence Matrix, RNN, and Wavelet-based Filter When Applied to Synthesized Texture Segmentation.

	Classification rate
Co-occurrence matrix (energy feature)	78%
RNN	77%
Wavelet Based Filter	90%

Table 2 shows that the Wavelet-based texture feature extraction filter could be used to extract texture characteristics and provide better class separation compared to the co-occurrence matrix and RNN approaches. The improved classification rate could be partially inferred by comparing Figure 20 and Figure 25 (top-left figure), where the advantage in class separability

(less overlap of distribution) of the Wavelet-based texture extraction filter compared to the GLCM approach is demonstrated. The reason behind this improvement most likely lies in the fact that the wavelet approach offers a more precise characterization of the scale parameter of the texture.

6.6 Applying the GLCM, RNN and Wavelet-based Texture Feature Extraction Filter to TRUS Images

6.6.1 GLCM

To calculate the GLCM of the ultrasound images, we must first select 1) the position operator P, 2) the size of the GLCM (the number of grey-levels to take into consideration) and 3) the desired GLCM features to compute. Since there are 256 grey-levels in the original TRUS images, the size of the GLCM is set to 256×256. As a preliminary experiment, 8 position operators are selected, covering the major directions of 0°, 45°, 90°, and -45°, at a distance of 1 and 3 pixels respectively (ie. (1,0), (1,-1), (0,1), (-1,1), (3,0), (3,-3), (0,3), (-3,3)). The features evaluated include energy, inertia, entropy, and homogeneity. (The contrast and correlation parameters are also examined. However, they were found to be unsuitable for distinguishing tissues in TRUS images.)

To evaluate the effect of the position operator, the GLCM of the TRUS image in Figure 33 is calculated with the 8 different position operators and the results are displayed in Figure 34 to Figure 37, visualizing the energy, inertia, entropy, and homogeneity in the different co-occurrence directions. The contrasts of the energy and homogeneity images are adjusted to increase the visual distinction between the benign and malignant tissues.

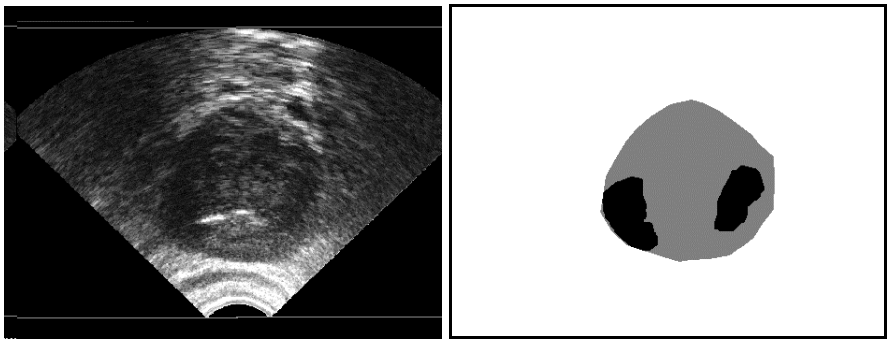

Figure 33. Original TRUS Image (left) and Radiologist Determined Tissue Classification (dark regions indicate potential tumour) (right).

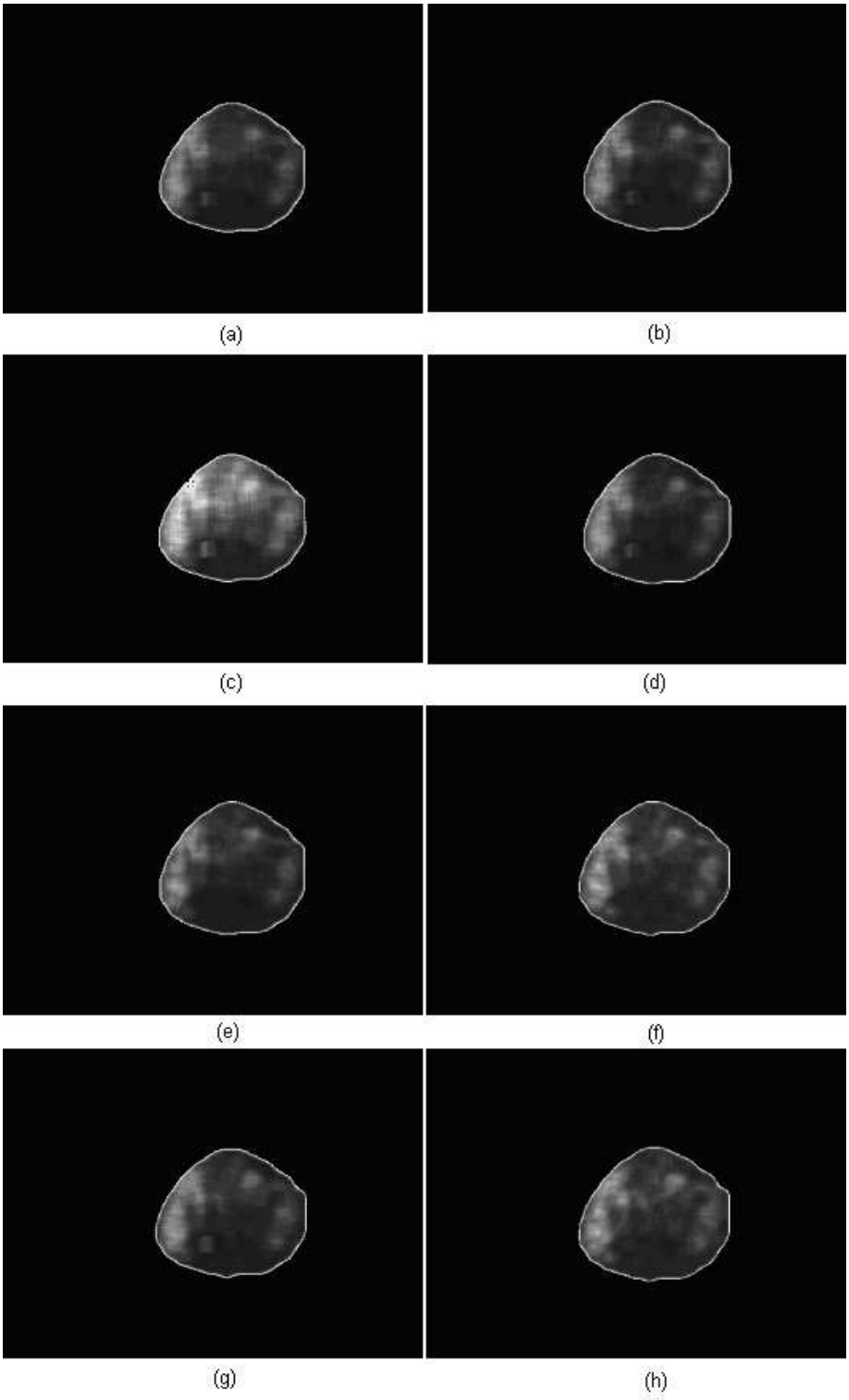

Figure 34. Energy of the GLCM of the TRUS Image in Figure 33 (left) at 8 Different Co-occurrence Positions: (a) (1,0), (b) (1,-1), (c) (0,1), (d) (-1,1), (e) (3,0), (f) (3,-3), (g) (0,3), (h) (-3,3).

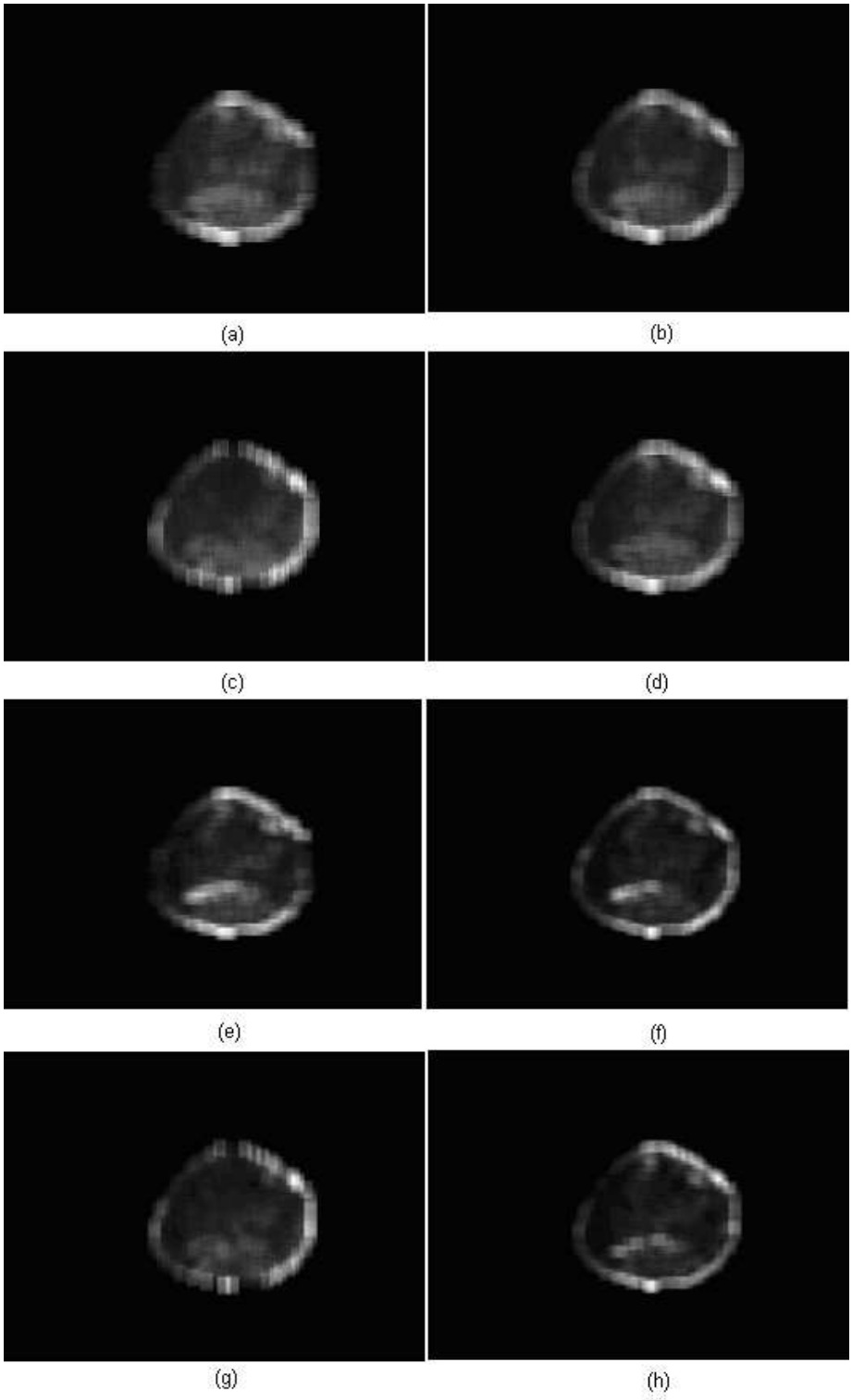

Figure 35. Inertia of the GLCM of the TRUS Image in Figure 33 at 8 different co-occurrence positions: (a) (1,0), (b) (1,-1), (c) (0,1), (d) (-1,1), (e) (3,0), (f) (3,-3), (g) (0,3), (h) (-3,3).

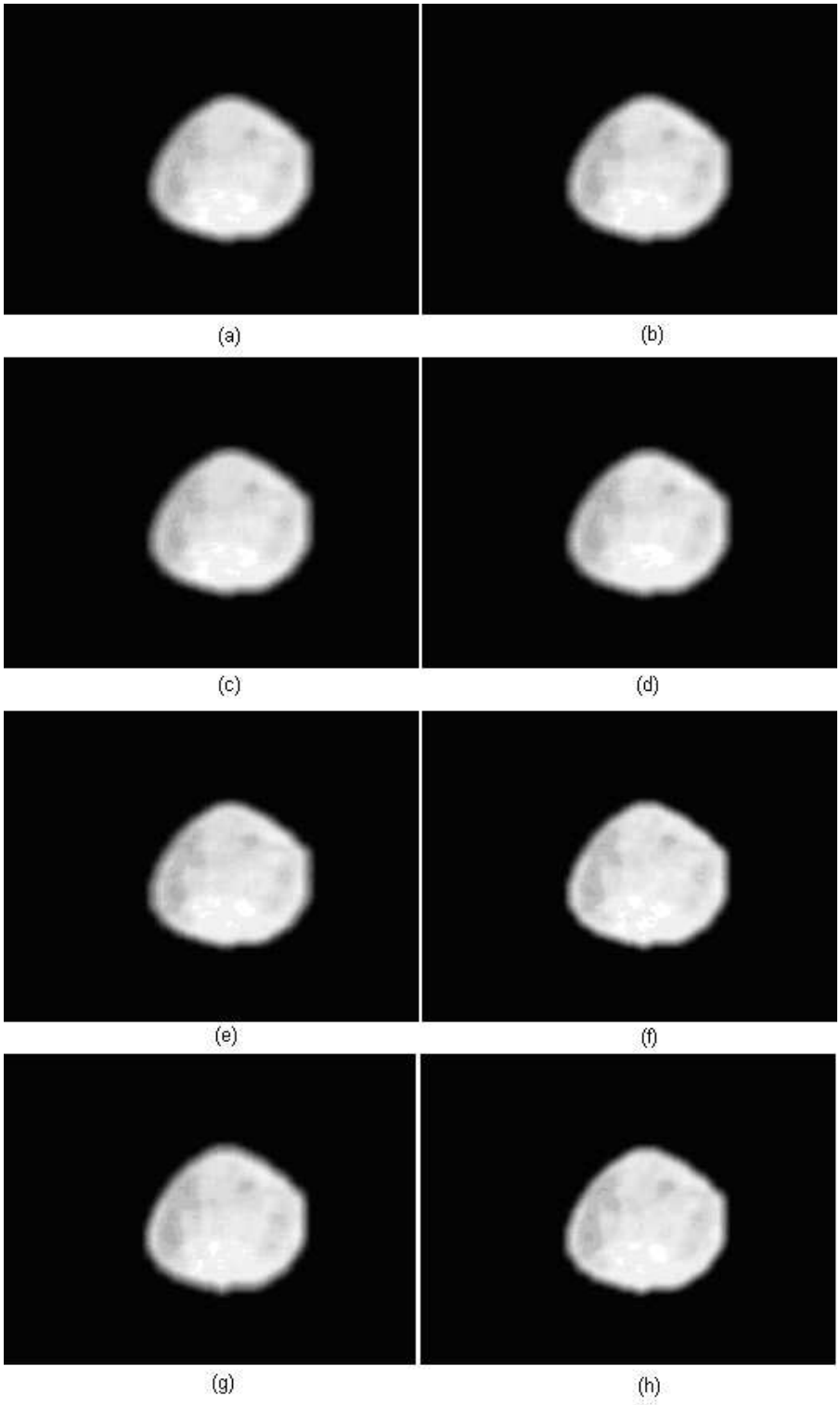

Figure 36. Entropy of the GLCM of the TRUS Image in Figure 33 at 8 Different Co-occurrence Positions: (a) (1,0), (b) (1,-1), (c) (0,1), (d) (-1,1), (e) (3,0), (f) (3,-3), (g) (0,3), (h) (-3,3).

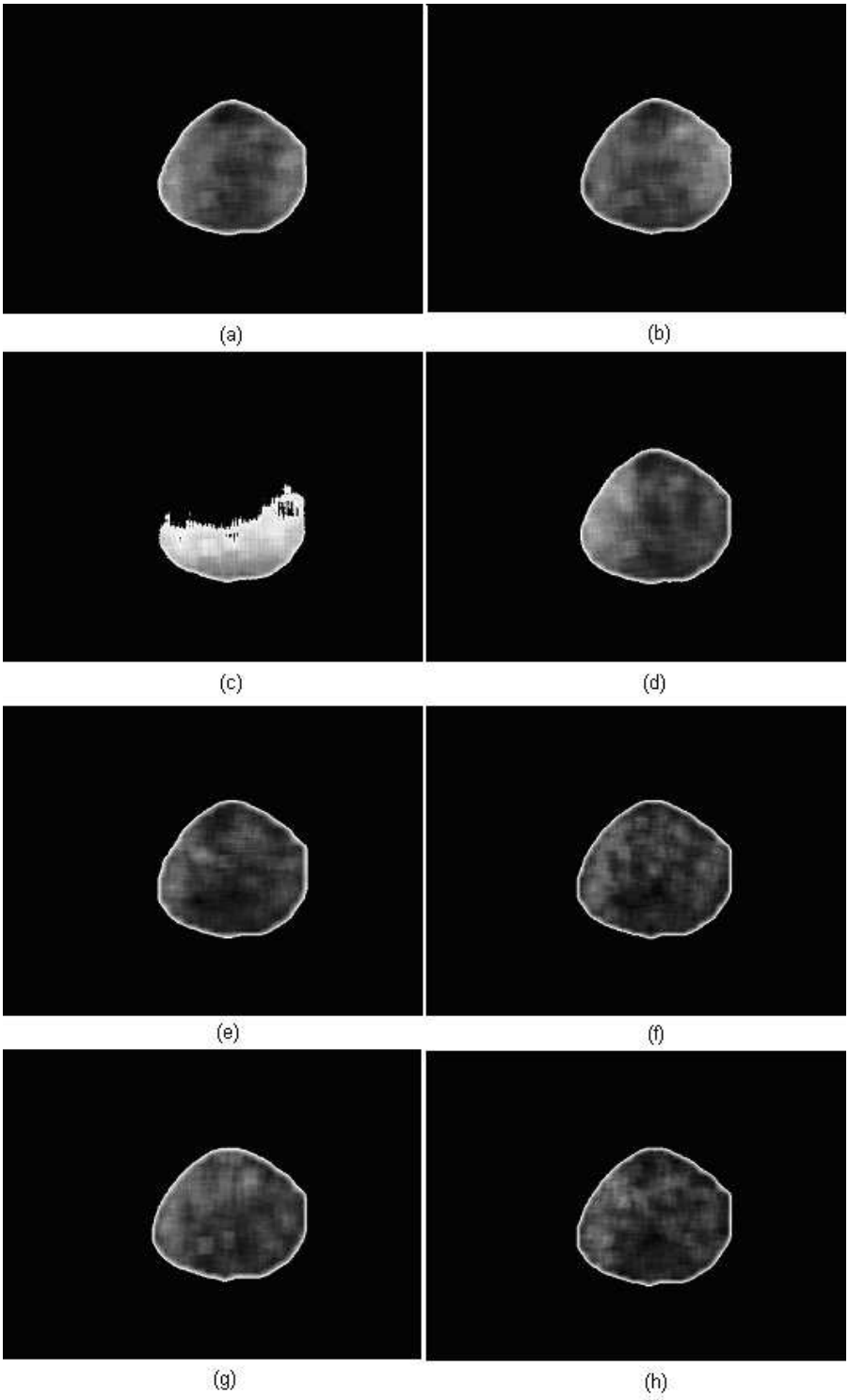

Figure 37. Homogeneity of the GLCM of the TRUS Image in Figure 33 at 8 Different Co-occurrence Positions: (a) (1,0), (b) (1,-1), (c) (0,1), (d) (-1,1), (e) (3,0), (f) (3,-3), (g) (0,3), (h) (-3,3).

Examining Figure 34 to Figure 37, we can see that the contrast adjusted GLCM features could potentially aid in distinguishing between the malignant and benign regions. It could also be argued that the effect of the position operator is not very noticeable, as the images of the same feature at various co-occurrence directions provide similar visual results. This indicates that the distribution of the tissue textures in the image is asymmetric with respect to the ultrasound probe.

To further probe the classification ability of the GLCM features, the GLCM of 24 TRUS images are evaluated at the (1,1) direction and the energy, inertia, entropy, and homogeneity are measured. Then, for each feature, a threshold is varied through its full range to segment the malignant and benign regions. For example, in Figure 38, the energy feature is used to segment the tissue regions at the threshold of 55 (left) and 60 (right).

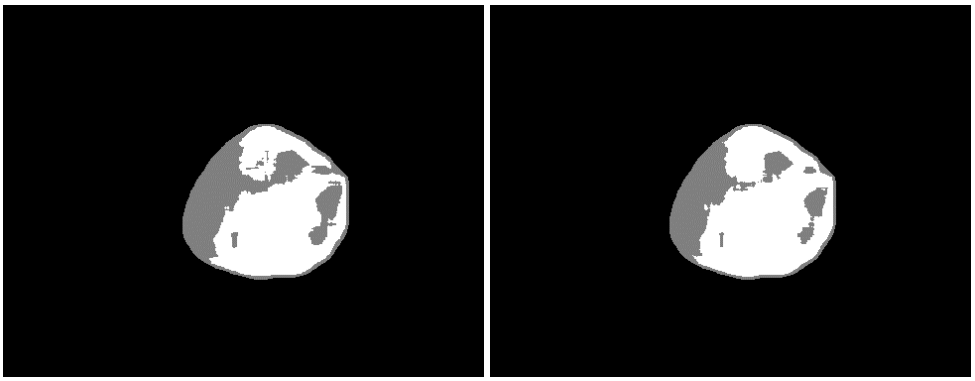

Figure 38. Segmented Image Using the GLCM Energy Descriptor at Thresholds of 55 (left) and 60 (right).

The receiver operating characteristic curve (ROC) analysis in Figure 39 demonstrates the sensitivity and specificity performance of the RNN in all the operating conditions. The ROC curves are obtained by continuously varying the two separation thresholds [38]. The area under the ROC curve (AUC) [39], in Figure 39, summarizes the accuracy of the test, taking into

account both sensitivity and specificity, as well as the full range of possible operation conditions. The classification rate (CR), sensitivity and specificity are defined as follows:

$$CR = \frac{tp + tn}{tp + fn + fp + tn}, \quad \textbf{Equation 15}$$

$$sensitivity = \frac{tp}{tp + fn}, \quad \textbf{Equation 16}$$

and

$$specificity = \frac{tn}{fp + tn}, \quad \textbf{Equation 17}$$

where *tp* denotes the true positives (the malignant blocks identified by the radiologist that are correctly detected), *fn* denotes the false negatives (the malignant blocks that are undetected), *fp* denotes the false positives (the benign blocks that are wrongly detected as malignant), and *tn* denotes the true negatives (the benign blocks that are correctly classified as such).

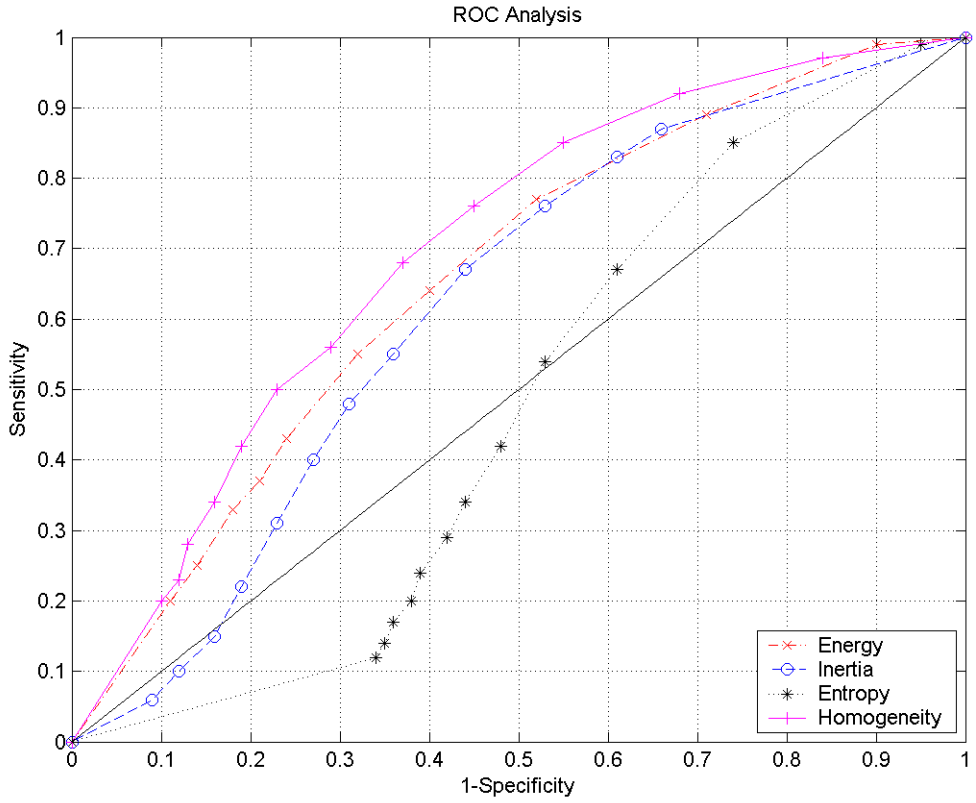

Figure 39. ROC of the GLCM Features Evaluated with 24 TRUS Images.

The area under the curve (AUC) for each GLCM are A_{ener}=0.66, A_{iner}=0.62, A_{ent}=0.48, and A_h=0.70. This indicates that amongst these GLCM features, energy and homogeneity are the best at distinguishing between the malignant tissue and benign tissue in TRUS images.

6.6.2 Applying RNN to TRUS

Six TRUS images that consist of 7,603 5×5 samples were used to train the RNNs with the procedure described in Section 6.3. The segmentation performance of the proposed algorithm was evaluated with five TRUS images that are distinct from the training images. From these images, a total of 6,423 5×5 samples were evaluated and classified. The resulting segmented images are compared to the desired segmentation in Figure 40.

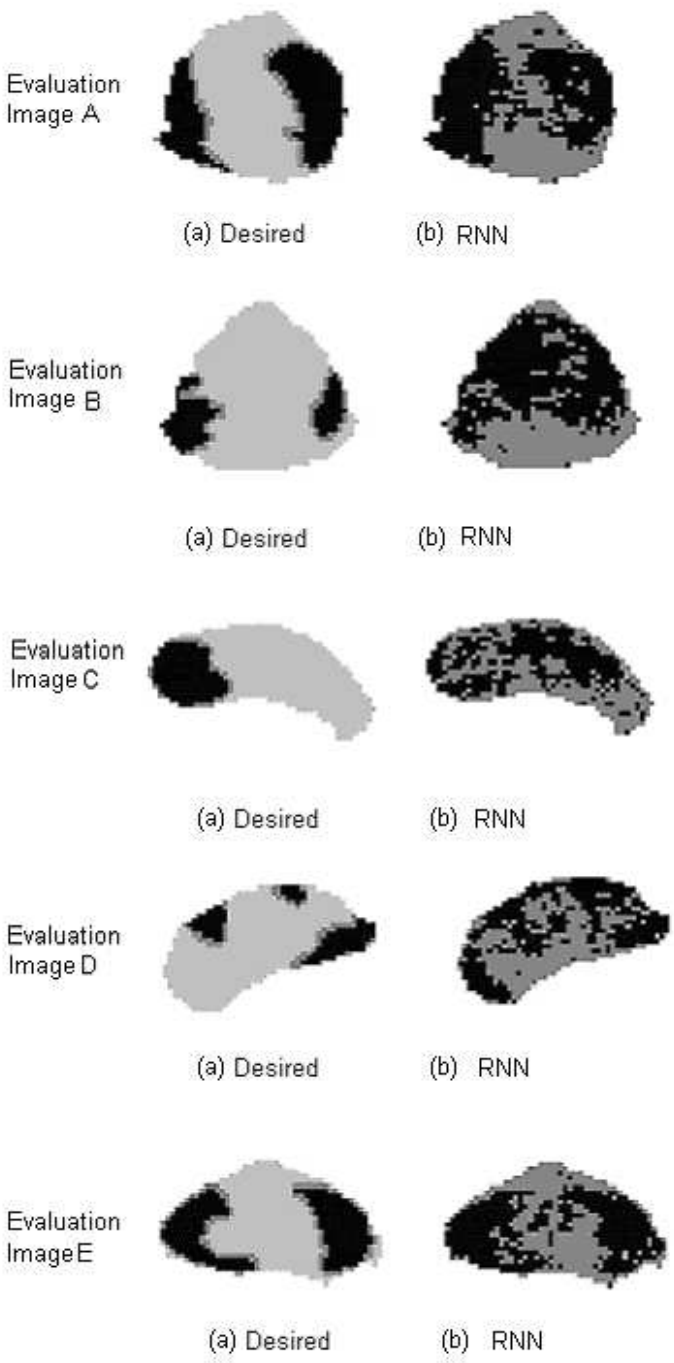

Figure 40. Result of the Segmentation with the RNN Approach (b) Compared to Desired Result (a).

The ROC for the RNN is displayed in Figure 41. The areas under curve (AUC) for the RNN is A_{RNN}=0.78.

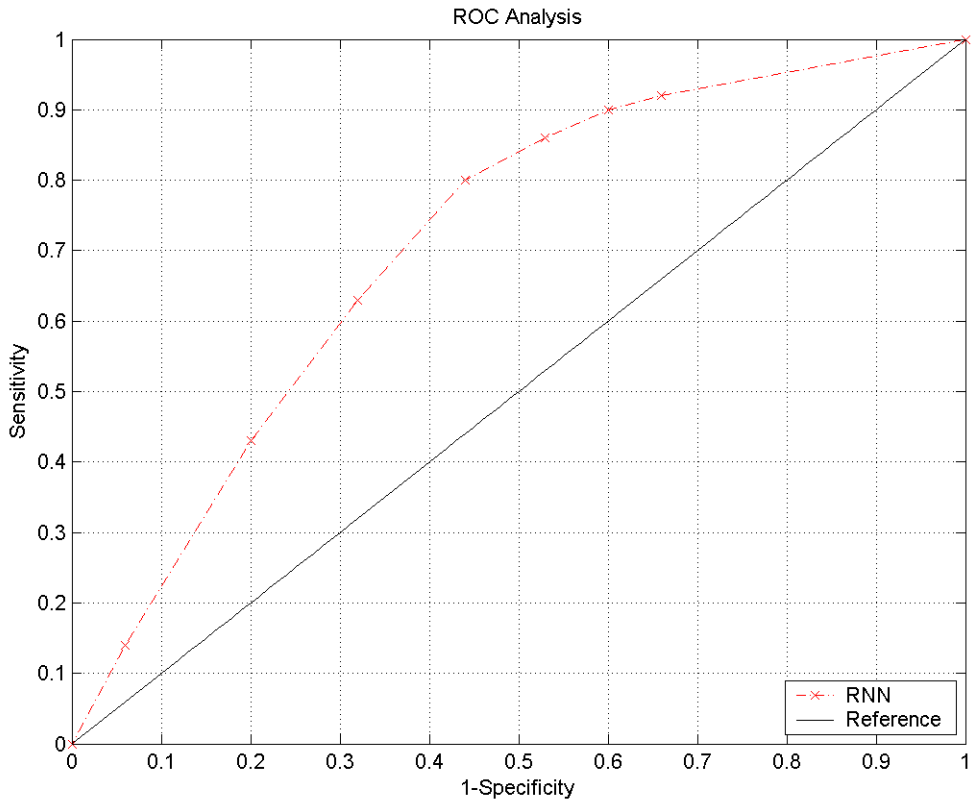

Figure 41. ROC of the RNN Approach.

6.6.3 Adapting the Generalized Wavelet-based Texture Extraction Filter for the Ultrasonic Prostate Cancer Detection Problem

A. Local Feature Filter

In order to construct a local feature filter that maximally linearly separates the malignant and benign regions, we must identify textural characteristics that distinguish the two regions.

The visual appearance of different grades of prostate cancer tissues through the microscope is described in Chapter 3. Although it is doubtful that glandular level details could be captured by a 7MHz transducer, due to its limited resolution, it is likely that part of this textural pattern is

reflected in the fine resolution speckles in the TRUS image due to the differing parenchyma of the malignant and benign tissues.

Passing the input image in Figure 33 (left) through the wavelet decomposition filter, we obtain the detail differences on the four finest resolution scales, which are displayed in Figure 42.

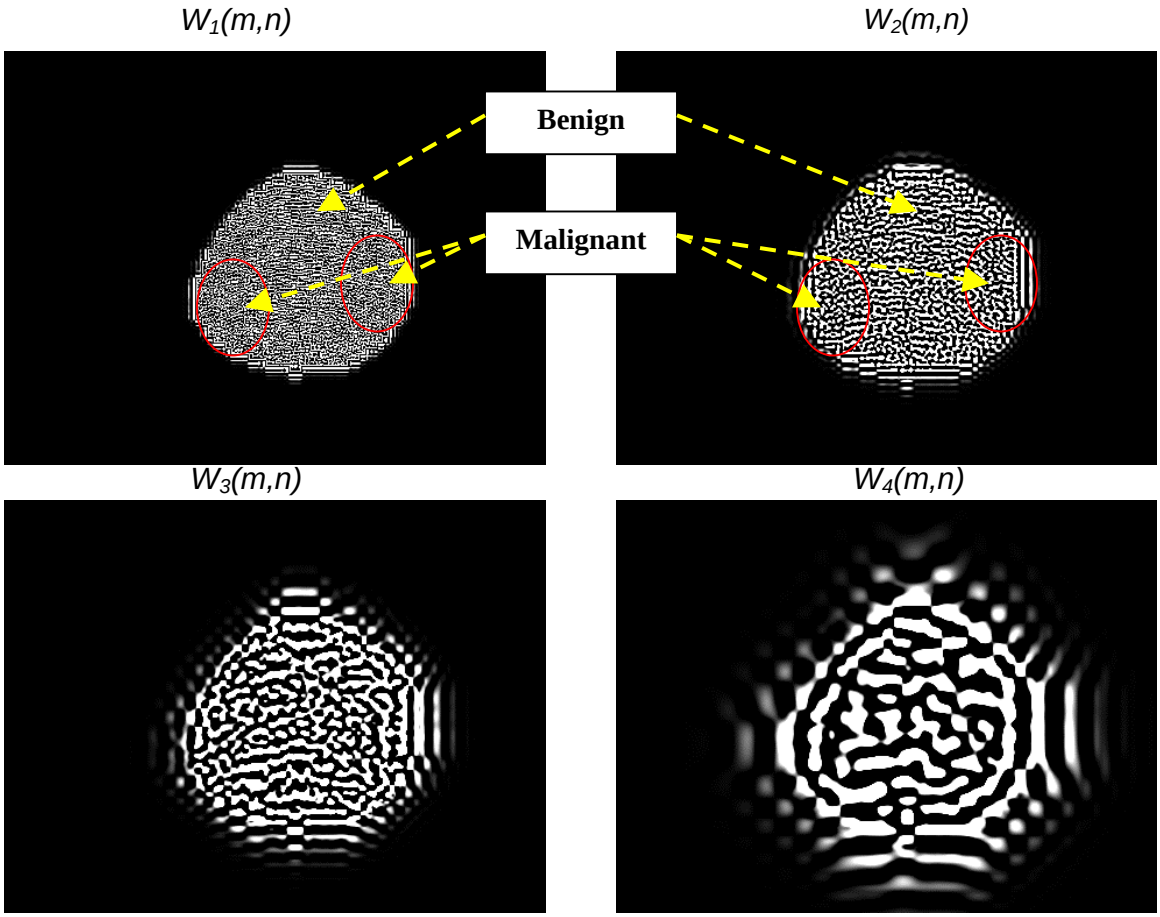

Figure 42. Wavelet Decomposition Details at the Four Finest Scales.

Examining the wavelet decomposition detail difference images at the finest resolutions, $W_1(m,n)$ and $W_2(m,n)$, it could be noted that the texture in the benign regions have a more ordered appearance characterized by uniform horizontal lines. The textures in the malignant regions however, are more disordered and granular. This is consistent with the pathological

description of tumour, with the benign regions consisting of uniform glands and malignant regions where the uniform structures are destroyed.

In Figure 43, the histogram of the wavelet decomposition detail difference $W_1(m,n)$, is displayed.

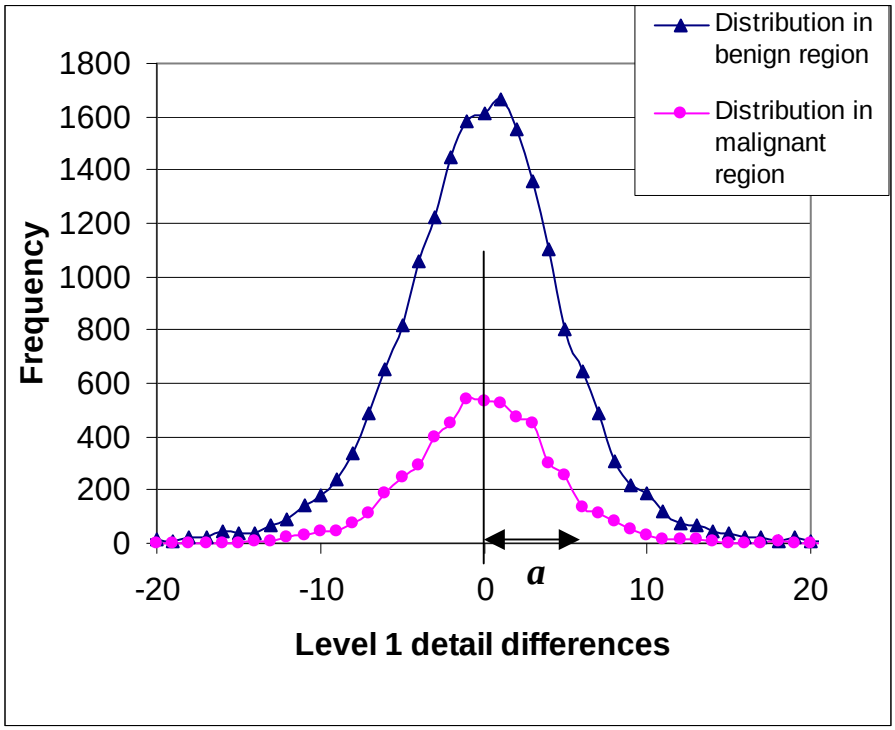

Figure 43. Wavelet Decomposition Level 1 Detail Difference Distribution in the Malignant and Benign Regions.

From Figure 43, it could be noted that at the finest wavelet decomposition level, the detail difference values in the malignant region are distributed in a more narrow range around zero as compared to the detail difference values in the benign region. This implies that it is possible to choose a threshold *a* as a tool to separate the malignant and benign regions, since the distribution shows that for detail difference values below *a*, the associated pixel is much more likely to be benign than malignant. It is found that by shifting $W_1(m,n)$ up by the value *a*, we can visually enhance the details in malignant and benign regions. This is because in the original

$W_1(m,n)$, values above 0 appear as bright image elements while those below appear as dark ones. As we shift $W_1(m,n)$ up by the value *a*, due to the more narrow distribution of the malignant region difference values, we effectively increase the perceived brightness in the malignant region compared to the benign region. This is shown in Figure 44 where *a* is set to 3.5.

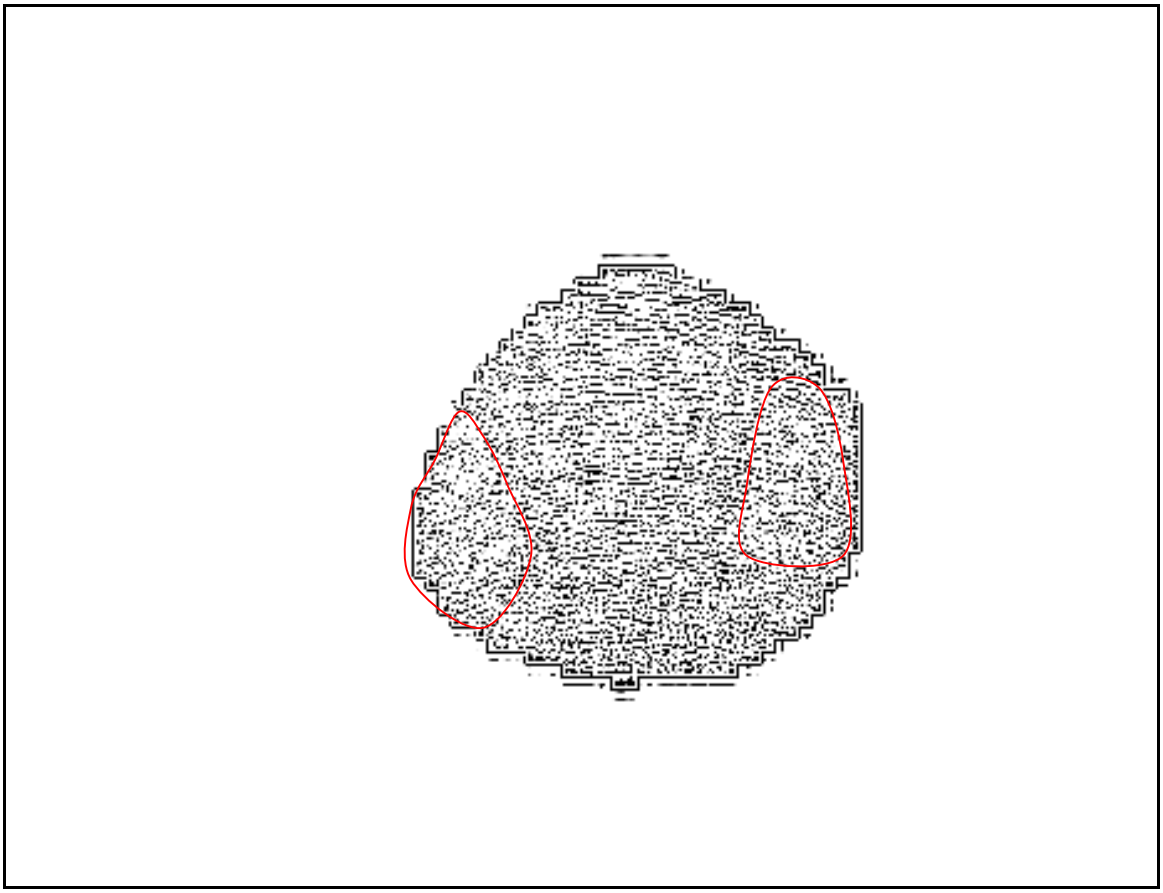

Figure 44. Enhanced Wavelet Decomposition Level 1 Detail Differences.

We also noted in Figure 42 and Figure 44 that in the fine scale wavelet decomposition detail that the benign region is characterized by uniform horizontal lines. We can also attempt to capture this characteristic by counting the amount of horizontally connected image elements with values below the threshold *a* in a local neighbourhood, which constitutes the local feature value for the centre image element of that local neighbourhood. We can define the degree of

connectivity by a parameter *b*, such that if *b* is set to 3 and there are three horizontally connected pixels below the threshold *a* in the local neighbourhood, the local feature counter would increase by one.

To find the optimal values of *a* and *b* to separate the malignant and benign distributions in the local feature domain, we first define the neighbourhood within which to count the local feature values to be 24×24 image elements. Then, to find the optimal value for the threshold *a*, we set *b* to a constant of 2, and plotted the distributions of the local feature values in the malignant and benign regions with *a*=10, *a*=5, *a*=3.5, and *a*=2. The histogram of local feature value distributions are displayed in Figure 45.

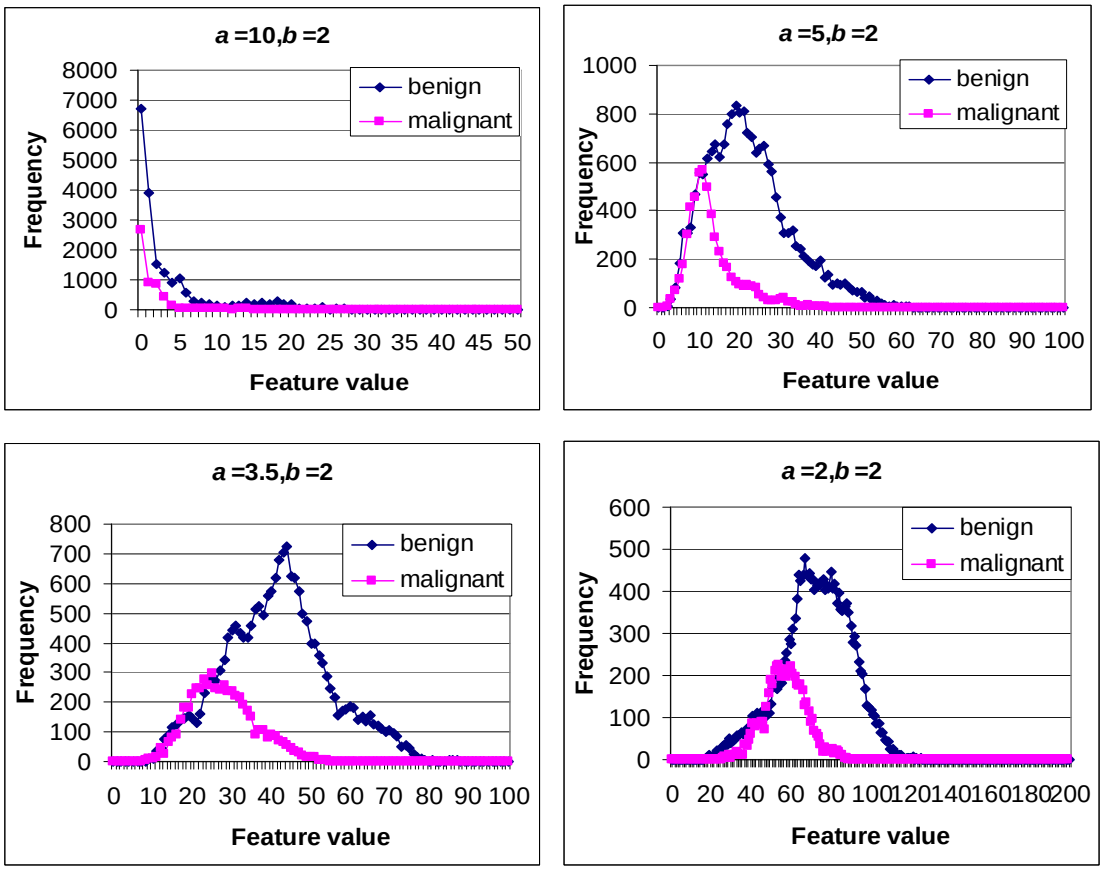

Figure 45. Local Feature Value Distributions with the Threshold *a* Set to 10, 5, 3.5 and 2 Respectively.

From Figure 45, we note that the threshold yielding the highest linear separation for the local feature values in the malignant and benign regions is *a*=3.5. At this threshold, the modes of the malignant and benign distributions are separated by a feature value distance of 25, which approximately covers half of the malignant distribution range.

Likewise, we can find the optimal characterizing degree of connectivity value *b*, by plotting the feature value distributions when *b* is varied. In Figure 46, the feature value distributions are plotted with *a* held constant at 3.5 and *b* set to 1, 2, 3, and 5 respectively.

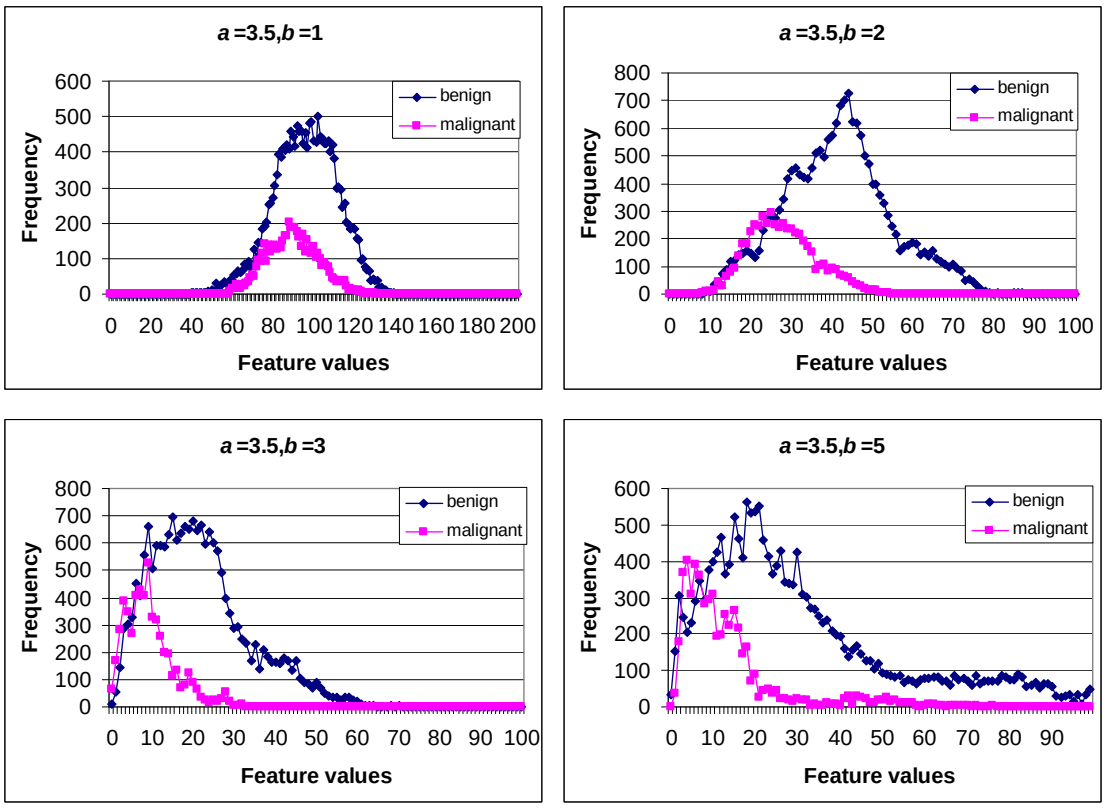

Figure 46. Local Feature Distributions with Varying Characteristic Degree of Connectivity Measure *b*.

From Figure 46, we notice that *b*=2 and *b*=5 yields good linear separation of the local feature distributions. For *b*=2, the modes of the distributions are separated by feature value distance of 25, which is approximately half of the range of the malignant distribution. For *b*=5, the modes of

the distributions are separated by a distance of 16, which almost covers the entire range of the malignant distribution. Therefore, a characteristic degree of connectivity value of 5 is selected for the subsequent analysis.

B. Identifying Malignant and Benign Regions with Proposed Texture Feature Extraction Filter

With the local feature distributions characterized by the parameters *a* and *b*, which should be universal for all TRUS images obtained at the same frequencies (ie. same spatial resolution), TRUS images suspected to have malignant tumour could be evaluated with the following steps.

1. Feed the outlined prostate image into the proposed filter, which transforms the input image in the intensity domain to the wavelet domain and then the local feature domain. At the output of the filter, the local feature values are calculated for each discrete image element.
2. Apply the local feature values as input to a classifier to classify the image elements.

The classifier used in step two could be a complex classifier such as a neural network or fuzzy inference system. However, to demonstrate the effectiveness of the textural feature extracted using the proposed algorithm, the simplest classifier, thresholding, will be used for the subsequent analysis.

Figure 47 demonstrates the classification result by setting the local feature value threshold to 8 (dark grey) and 25 (light grey) for the training image (white represents benign region).

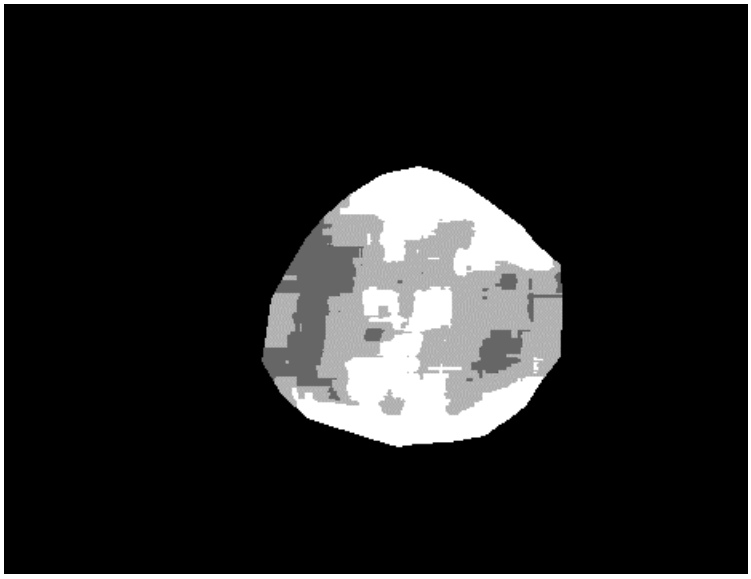

Figure 47. Classification Result with Local Feature Value Thresholds of 8 and 25.

The effectiveness of the textural feature extracted is examined by applying the proposed approach to 23 TRUS images distinct from the training image used to characterize the local textural feature distributions. Thresholding is used as the classification method. In Figure 48 to Figure 55, the original TRUS image, desired classification, enhanced level 1 detail difference image, and resulting classification of 8 of the evaluation images are displayed. For the resulting classification image, feature value thresholds of 8 and 25 are used.

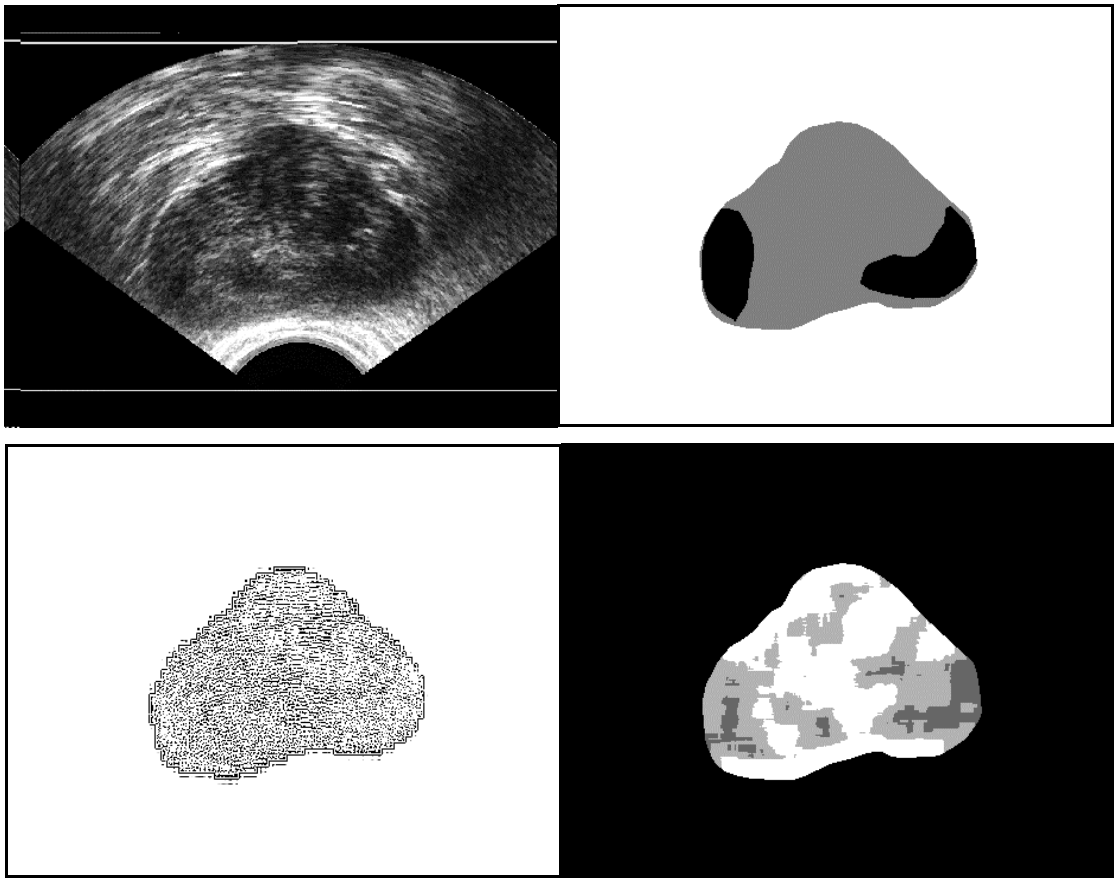

Figure 48. Results for Evaluation Image A. Original Image (Top-Left), Desired Segmentation (Top-Right), Enhanced Level 1 Detail Difference (Bottom-Left), and the Result of Applying Thresholding to the Extracted Textural Feature (Bottom-Right).

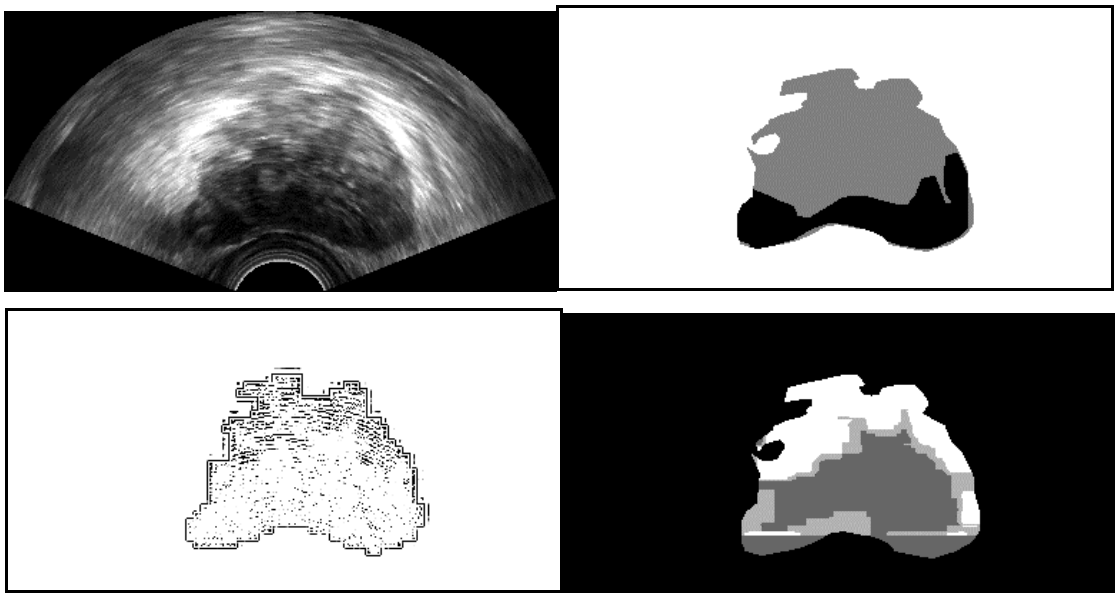

Figure 49. Results for Evaluation Image B. Original Image (Top-Left), Desired Segmentation (Top-Right), Enhanced Level 1 Detail Difference (Bottom-Left), and the Result of Applying Thresholding to the Extracted Textural Feature (Bottom-Right).

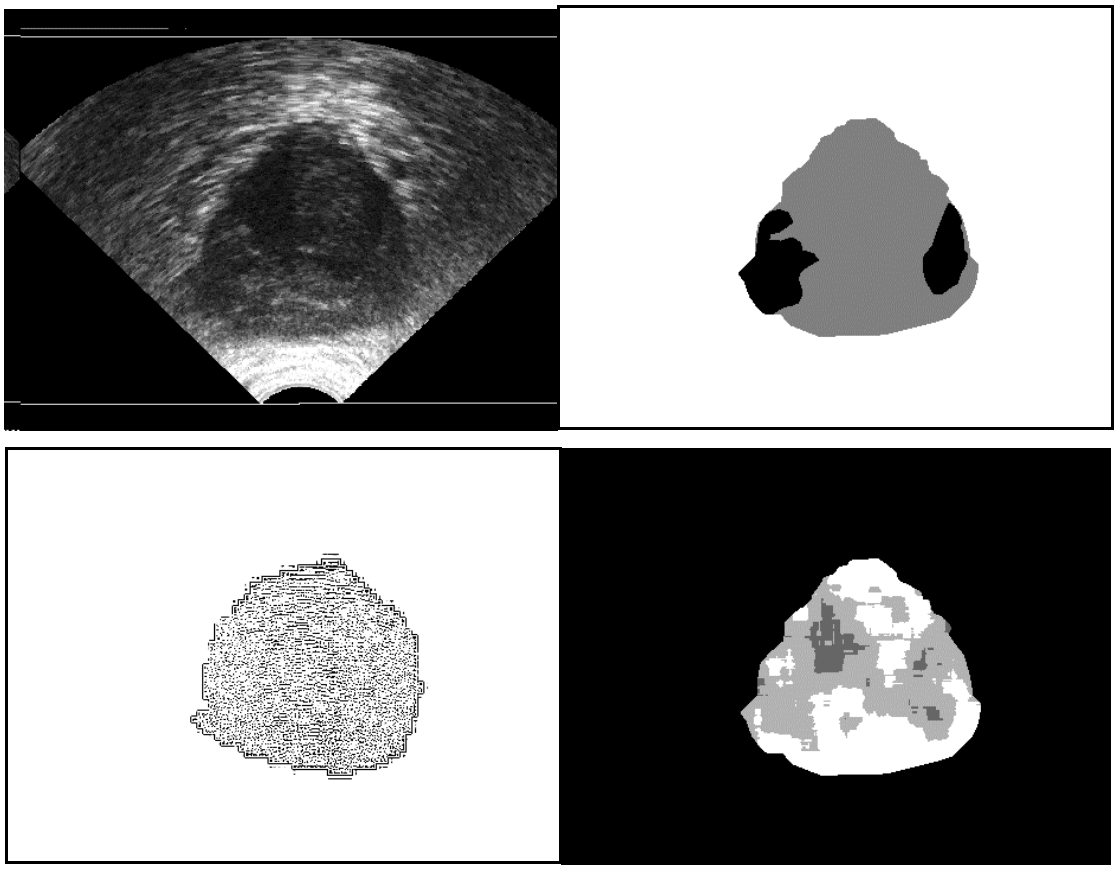

Figure 50. Results for Evaluation Image C. Original Image (Top-Left), Desired Segmentation (Top-Right), Enhanced Level 1 Detail Difference (Bottom-Left), and the Result of Applying Thresholding to the Extracted Textural Feature (Bottom-Right).

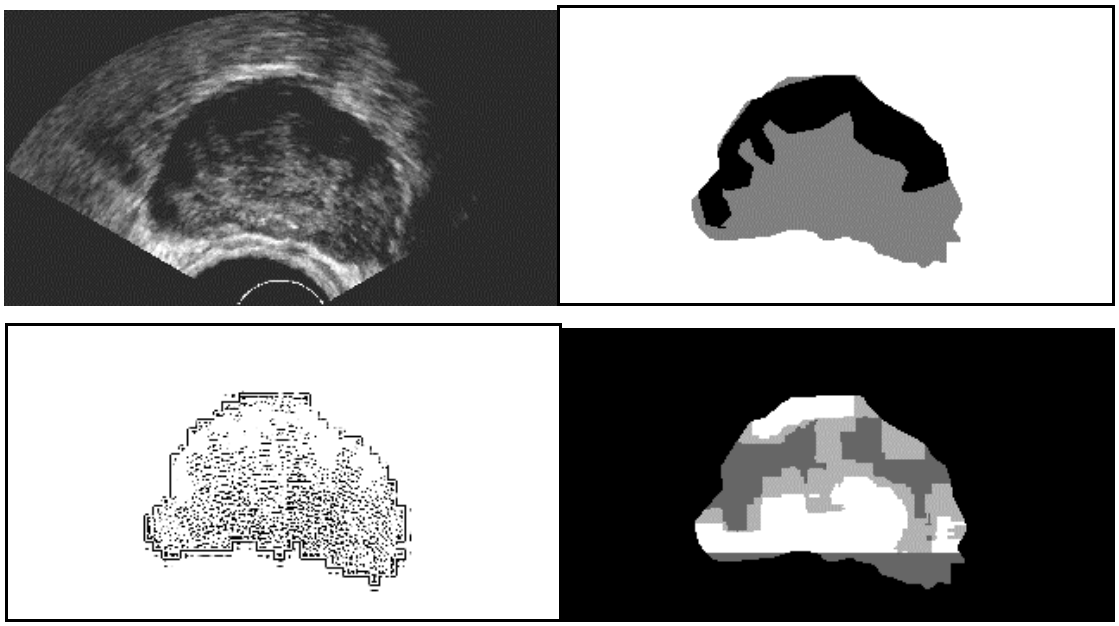

Figure 51. Results for Evaluation Image D. Original Image (Top-Left), Desired Segmentation (Top-Right), Enhanced Level 1 Detail Difference (Bottom-Left), and the Result of Applying Thresholding to the Extracted Textural Feature (Bottom-Right).

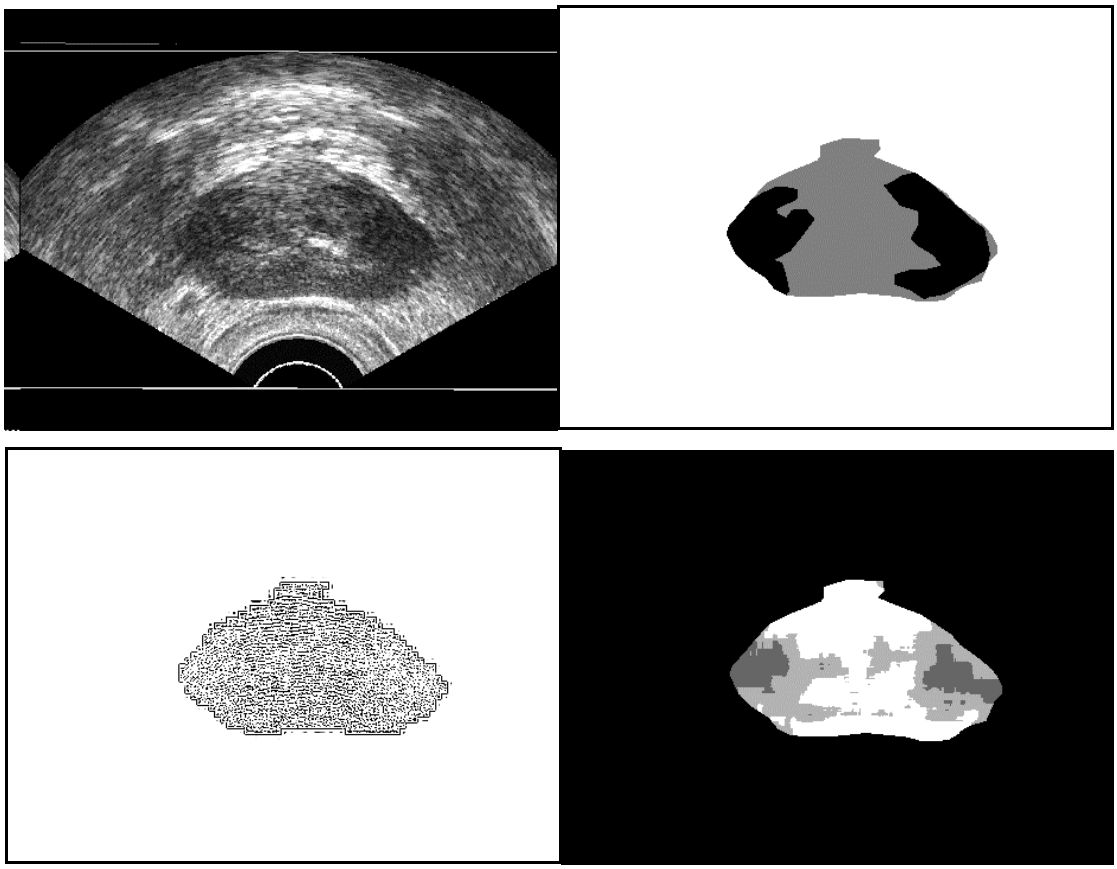

Figure 52. Results for Evaluation Image E. Original Image (Top-Left), Desired Segmentation (Top-Right), Enhanced Level 1 Detail Difference (Bottom-Left), and the Result of Applying Thresholding to the Extracted Textural Feature (Bottom-Right).

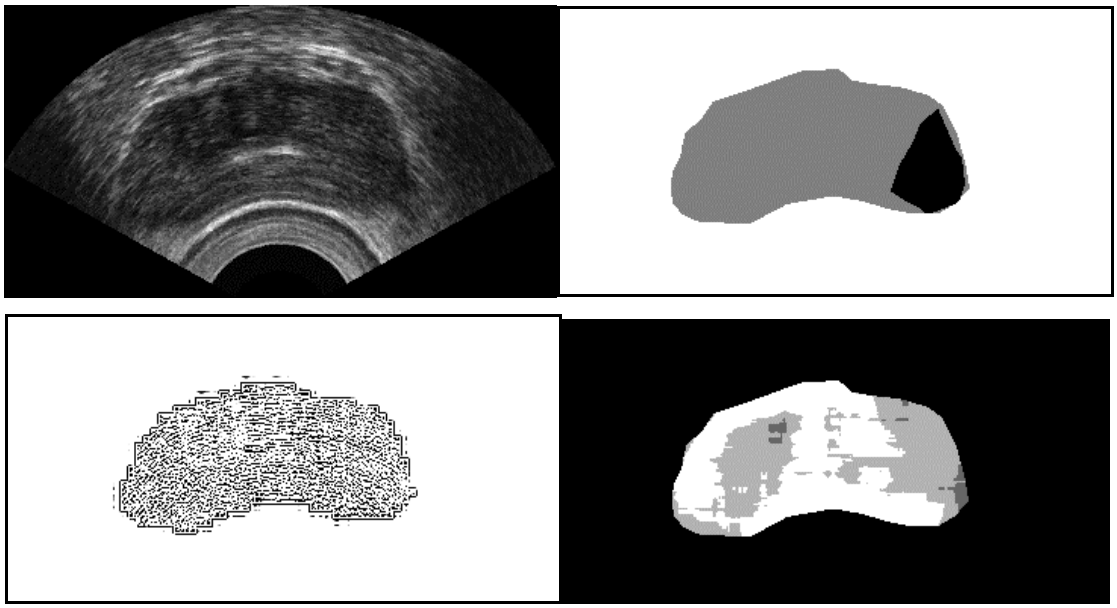

Figure 53. Results for Evaluation Image F. Original Image (Top-Left), Desired Segmentation (Top-Right), Enhanced Level 1 Detail Difference (Bottom-Left), and the Result of Applying Thresholding to the Extracted Textural Feature (Bottom-Right).

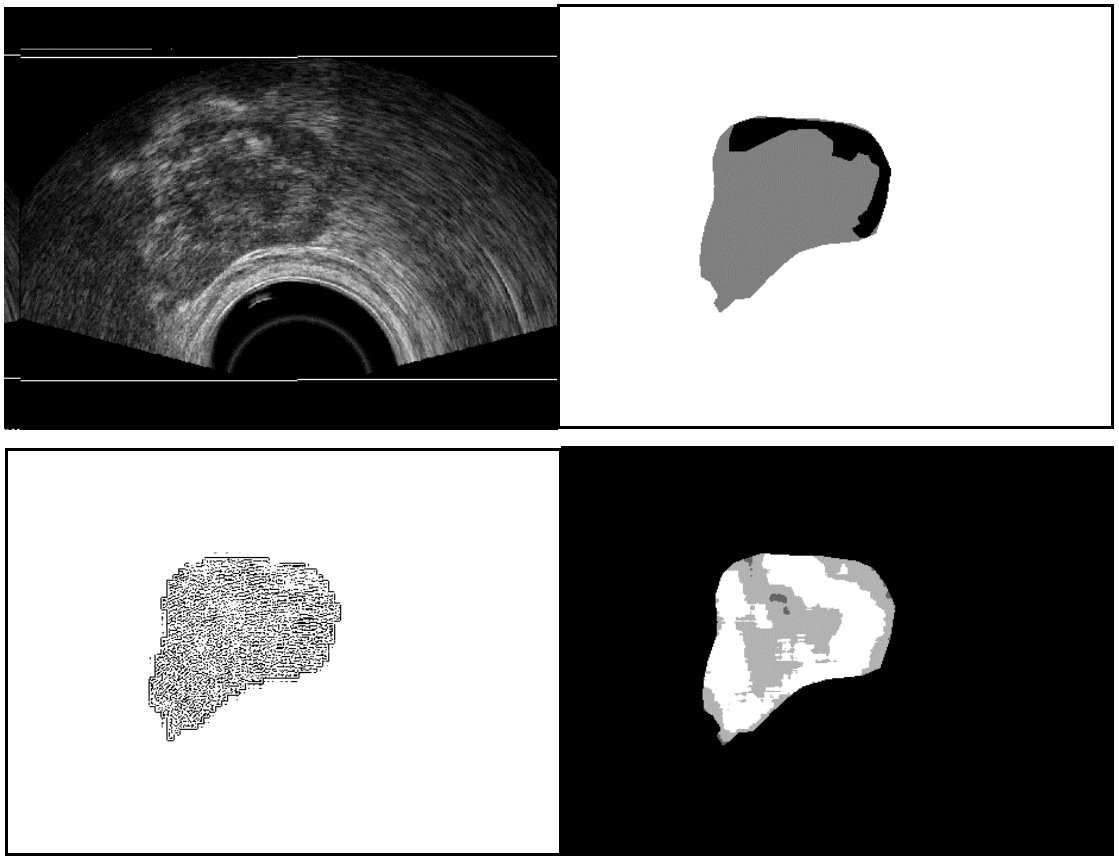

Figure 54. Results for Evaluation Image G. Original Image (Top-Left), Desired Segmentation (Top-Right), Enhanced Level 1 Detail Difference (Bottom-Left), and the Result of Applying Thresholding to the Extracted Textural Feature (Bottom-Right).

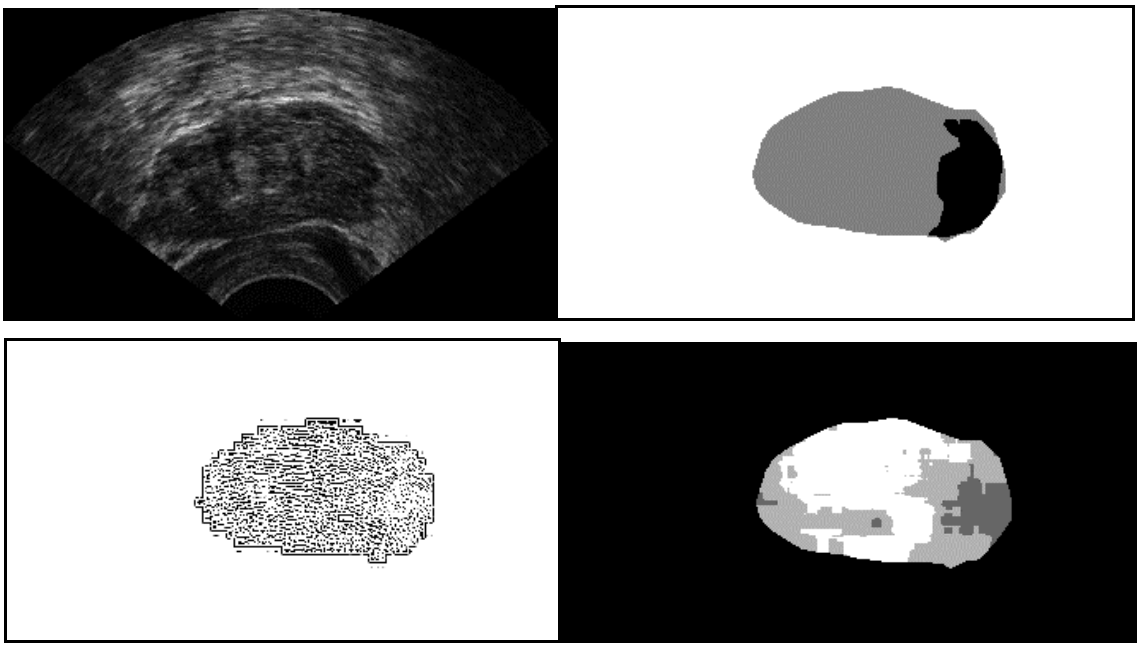

Figure 55. Results for Evaluation Image H. Original Image (Top-Left), Desired Segmentation (Top-Right), Enhanced Level 1 Detail Difference (Bottom-Left), and the Result of Applying Thresholding to the Extracted Textural Feature (Bottom-Right).

The proposed textural feature could effectively identify most of the malignant regions in the evaluation images. Most of the segmentation results are already apparent in the enhanced level 1 detail difference image. In fact, the enhanced detail image contains much more information than the feature value image, and it could be effective as a decision support tool for radiologists for manual region segmentation. The value of the extracted textural features lies in their ability to be used as input to complex classifiers for robust automated malignant and benign region identification.

The receiver operating characteristic curve (ROC) analysis in Figure 56 compares the sensitivity and specificity performance of the extracted textural feature taking into account all 23 evaluation images. The ROC curves are obtained by continuously varying the feature value threshold. The areas under curve (AUC) when applying linear thresholding to the extracted

textural feature is A_z=0.72. The AUC quantifies the linear separability of the malignant and benign distributions in the extracted textural feature. Thus, the AUC is a measure of the effectiveness of the feature if it is used as input to a complex classifier.

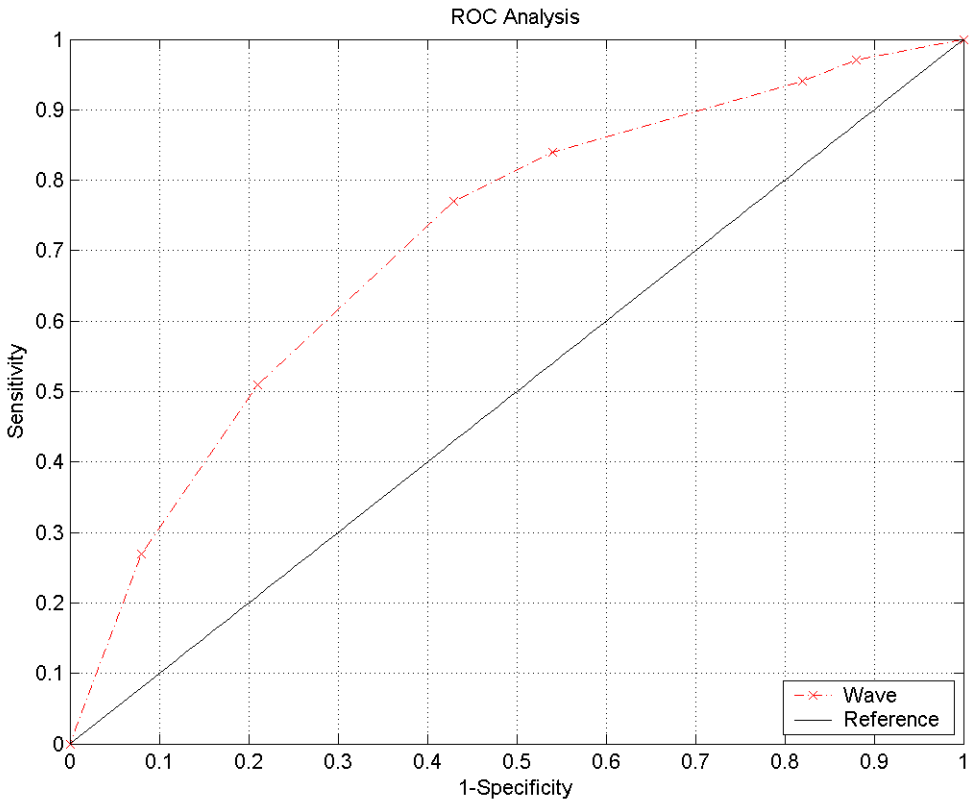

Figure 56. ROC Analysis for Extracted Textural Feature.

6.6.4 Comparing the Performance of the Three Approaches on Extracting Texture Features From TRUS

The areas under the ROC curve for the various approaches examined in this chapter are listed in Table 3. From the data cited, the RNN approach provides the highest AUC. However, the wavelet-based filter provides a better tool to visualize the textural properties within the TRUS image as demonstrated in Figure 44. Furthermore, with further optimization, the wavelet-based filter should achieve improved separation of the malignant region and the benign region.

Table 3. AUC Comparison Between the Different Approaches.

	Area Under ROC Curve (AUC)
GLCM (Energy)	0.66
GLCM (Inertia)	0.62
GLCM (Entropy)	0.48
GLCM (Homogeneity)	0.70
RNN	0.78
Wavelet-based Filter	0.72

6.7 Chapter Summary

In this chapter, the topic of texture feature extraction in the context of ultrasound prostate cancer images is explored. The notions of local texture feature and texture feature extraction are defined. Then, three approaches to extract the local texture features are examined in detail. These include the co-occurrence matrix approach, the RNN approach and the wavelet-based texture feature extraction filter. In the next chapter, the topic of spatial feature extraction and how the extracted texture feature and the spatial feature could be synthesized to produce a more accurate automated diagnostic result is examined.

Chapter 7
Spatial Feature Extraction and Fuzzy Inferencing to Combine the Features

7.1 Introduction

Spatial features are identified in Chapter 4 to be useful in determining malignancy in ultrasound images of the prostate. In this chapter, a novel approach to extract statistical spatial features is examined. We also look at how the information from the textural feature and the spatial feature could be fused to provide a binary classification decision with fuzzy inferencing.

7.2 Converting Texture Feature Space to Fuzzy Membership Functions

The fuzzy inference stage defines the relationship between the output of the RNN, the spatial distribution of the cancerous tissues in the prostate, and the desired result. To construct the fuzzy inference system [40][41], the fuzzy membership function that is associated with each of the input variables needs to be found.

7.2.1 Converting GLCM Features to Fuzzy Membership Functions

The extraction of GLCM textural features is explored in Chapter 6. Amongst this class of features, the energy feature and the homogeneity feature have shown to provide the best separation between the malignant and benign image elements. In this section, the statistical distributions of these two features are converted into fuzzy membership functions.

A basic definition of fuzzy membership function is at a specific feature value, what is the probability that this element belongs to a particular class. For the 'is malignant' fuzzy membership function of the GLCM energy feature, μA_1, this translates to the following equation:

$$\mu A_1(x) = \frac{m(x)}{m(x) + b(x)} \qquad \textbf{Equation 18}$$

where *x* represents the full range of the GLCM energy feature space, *m(x)* represents the total number of malignant image elements at that feature value and *b(x)* represents the total number of benign image elements at that feature value.

The complementary fuzzy membership function, μA_2, which denotes 'is benign from GLCM energy feature', is defined as follows:

$$\mu A_2(x) = 1 - \mu A_1(x) \qquad \textbf{Equation 19}$$

To ensure the smoothness of the fuzzy membership functions, Equation 18 is evaluated in 20 ranges of the GLCM energy feature space. The ranges are selected to optimally represent the distribution at locations with the highest distribution densities. Similarly, the fuzzy membership functions 'is malignant from GLCM homogeneity feature' and 'is benign from GLCM homogeneity feature' could be calculated using Equation 18 and Equation 19. The resulting fuzzy membership functions 'is malign from GLCM energy feature', and 'is benign from GLCM homogeneity feature', are displayed in Figure 57.

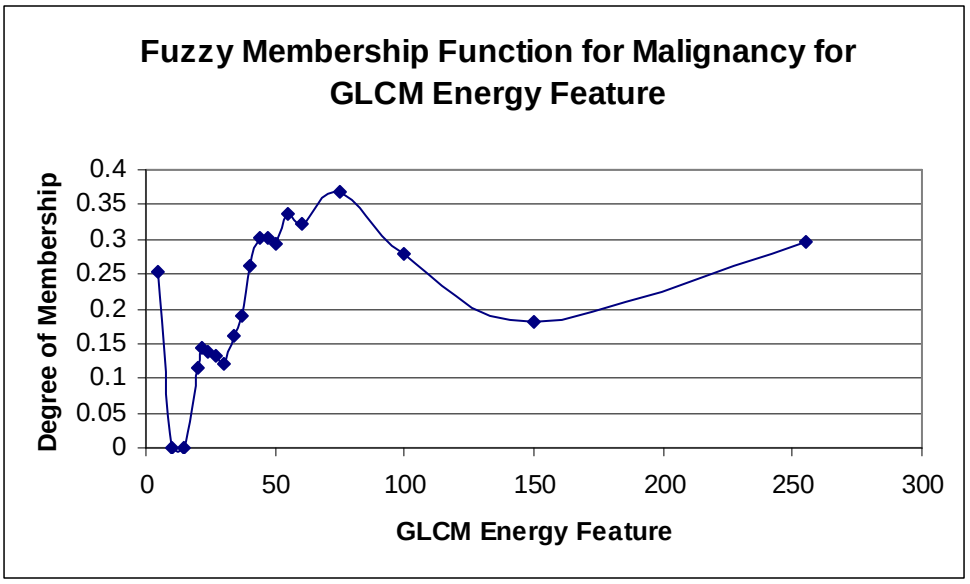

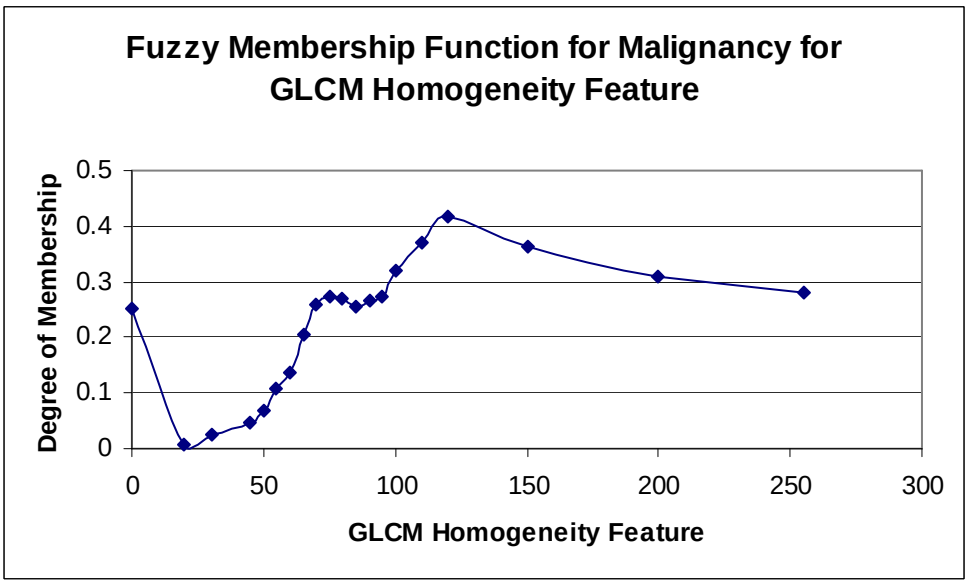

Figure 57. The 'is Malignant' Fuzzy Membership Function for the GLCM Energy and Homogeneity Features.

7.2.2 Converting RNN Output to Fuzzy Membership Functions

A lower error output from one RNN compared to the other indicates that the input block is more likely to belong to the region that the first RNN represents. Therefore, the difference between the outputs of the RNNs can be used as an indicator to classify the input block. The RNN output difference from the training sample ranges from -0.6 to 0.2. The desired result, with respect to the difference between the RNN output values is plotted in Figure 58.

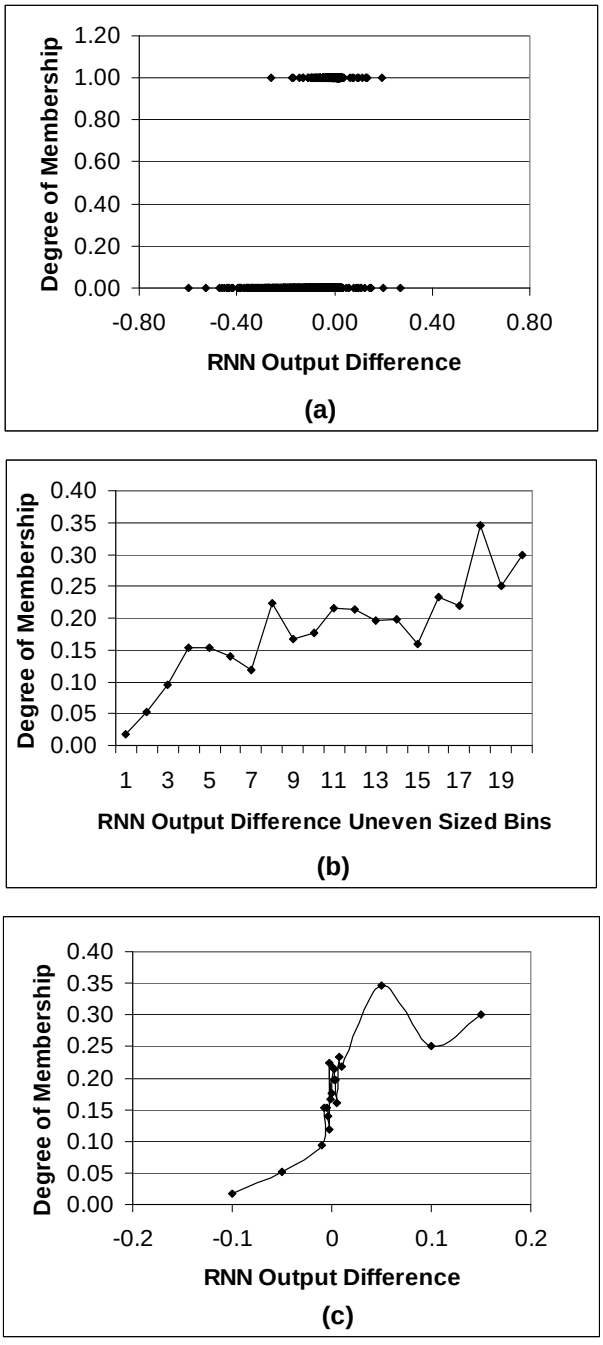

Figure 58. (a) Desired Output with Respect to the Distribution of RNN Output Difference (On y-axis, 1 Signifies Malignant and 0 Signifies Benign), (b) Degree of Membership Distribution Slotted into Uneven Sized Bins, and (c) Rescaled Degree of Membership Distribution.

To construct the membership function, this difference is slotted in 20 uneven sized bins (along the RNN output difference axis in Figure 58a). The bin size is chosen to be proportional to the density of the distribution of RNN output differences. This expresses the rapid variation in the degree of membership around the RNN output difference of zero, where the distribution density is the highest. The degree of membership is obtained by dividing the number of malignant samples by the number of total samples in that bin, as defined in Equation 18, and is illustrated in Figure 58(b). The rescaled degree of membership distribution is constructed by converting the x-axis from the uneven sized bins back to the original RNN output difference scale. This distribution is reflected in Figure 58(c) with the x-axis representing the RNN output differences and the y-axis representing the proportion of the malignant blocks to the total blocks in each RNN output difference segment. This is used as the membership function μA_1, which denotes "*is malignant* from the RNN indicator". Its complement is used as the membership function μA_2, which denotes "*is benign* from RNN indicator".

7.2.3 Converting Texture Feature From the Wavelet-based Filter to Fuzzy Membership Functions

The fuzzy membership functions 'is malignant from Wavelet-based filter' and 'is benign from Wavelet-based filter' are constructed using similar approach as described above. The resulting 'is malignant' fuzzy membership function is displayed in Figure 59.

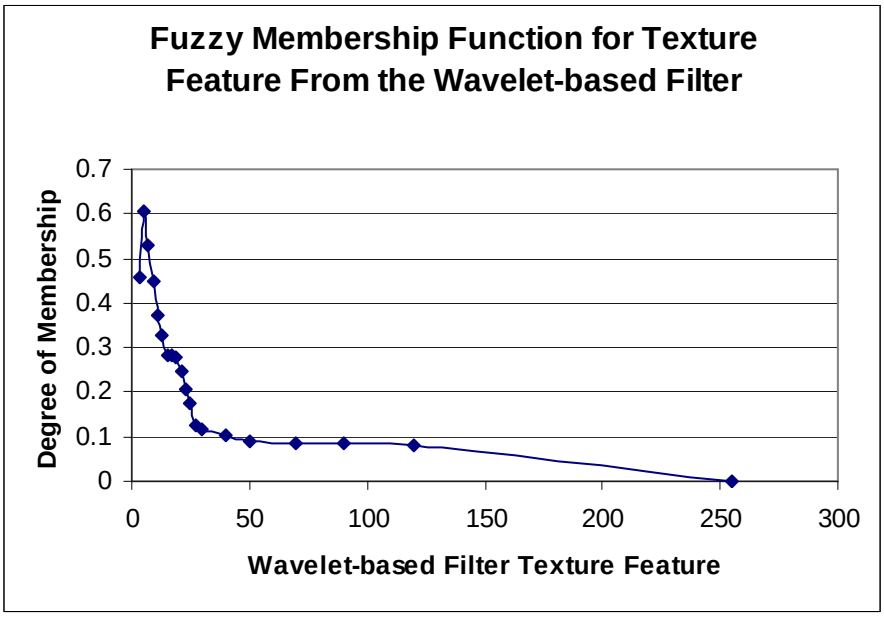

Figure 59. Fuzzy Membership Function 'Is Malignant From the Wavelet-based Filter'.

7.3 2×1D Membership Function Approach to Capture the Statistical Spatial Distribution of Malignancy

If we use a conventional 2×1D fuzzy membership function to capture the statistical spatial distribution of malignancy, the fuzzy inference system, as is described in Chapter 5, consists of 3 inputs and 3 classical 1D membership functions. The first input and the corresponding membership function is associated with the textural feature value (GLCM, RNN, or Wavelet-based). The second and third inputs and the corresponding membership functions relate to the 1D statistical distributions of malignancy in the horizontal (*l* direction) and vertical (*m* direction) directions. Together, these two 1D membership functions give an approximation of the 2D statistical distribution of malignancy.

The relative horizontal and vertical position finders translate absolute pixel position into relative position with respect to the center of mass in the horizontal and vertical directions. The centre of mass in the horizontal direction is located by summing the *l*-coordinate of the first pixel

of each block and dividing the sum by the total number of blocks. The centre of mass in the vertical direction is computed similarly using the *m*-coordinate (Equation 20). The expression for the centre of mass calculation is as follows:

$$CM_l = \frac{1}{N}\sum_{i=1}^{N} l_i$$
$$CM_m = \frac{1}{N}\sum_{i=1}^{N} m_i$$

Equation 20

where l_i and m_i represent the *l*-*m* coordinates of the first pixel of the image block *i* and *N* is the total number of blocks within the prostate boundary.

The relative position in the horizontal and vertical direction are divided into 20 bins, with bins -10 to 0 representing relative positions from the extreme left or extreme top block to the centre of mass and 0 to 10 representing relative positions from the centre of mass to the extreme right or extreme bottom block. The spatial distribution of malignant tissues (% malignant tissue blocks over the total number of blocks in each of the relative position bins) in both directions is plotted in Figure 60.

The horizontal distribution, or distribution in the *l* direction (Figure 60a), is used as the membership function μB_1 ('is malignant' from horizontal distribution) and its complement as μB_2 ('is benign' from horizontal distribution). The vertical distribution, or distribution in the *m* direction (Figure 60b), is used as the membership function μC_1 ('is malignant' from vertical distribution) and its complement as μC_2 ('is benign' from vertical distribution).

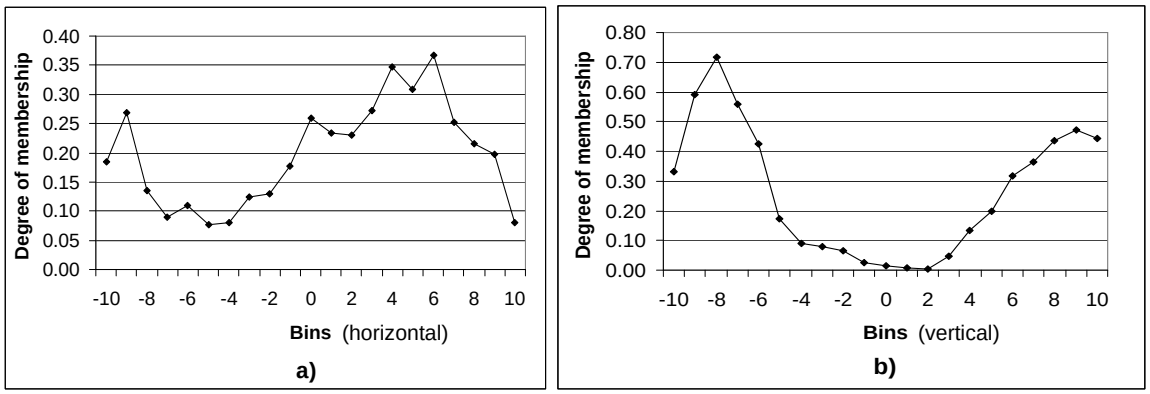

Figure 60. 1D Membership Functions in the *l* (a) and *m* (b) Directions in the Fuzzy Inference System Using Purely 1D Fuzzy Membership Functions.

7.4 Fuzzy Inference System

The fuzzy inference system architecture with the replaceable textural feature extraction and spatial feature extraction blocks is explained in Chapter 5. For example, if RNN is used for textural feature extraction and the 2×1D fuzzy membership function approach described in Section 7.3 is used to represent the spatial features, then the resulting system is the one represented in Figure 61.

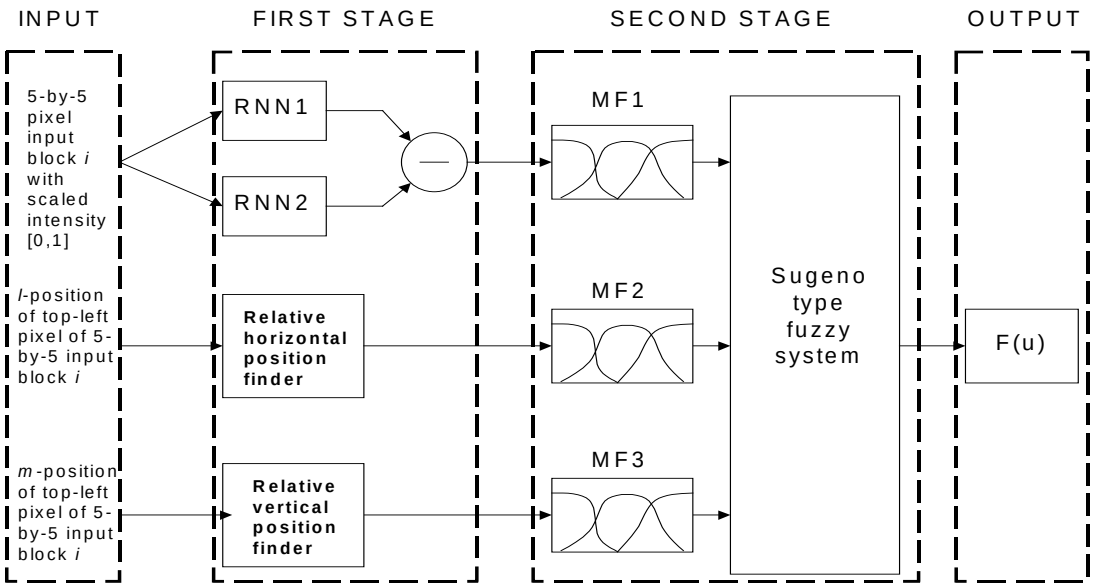

Figure 61. The Fuzzy Inference System with the RNN as the Textural Feature Extraction Block and 2×1D Fuzzy Membership Functions as the Spatial Feature Extraction Block.

If the GLCM features or Wavelet-based features are used for textural feature extraction, then instead of using 5×5 pixel blocks, individual pixels are used as inputs.

The input membership functions, μA_1, μA_2, μB_1, μB_2, μC_1, and μC_2, are defined in the previous sections.

The output membership functions are defined as two triangular membership functions. μD_1 represents ‘is benign’, while μD_2 represents ‘is malignant’ (Figure 62).

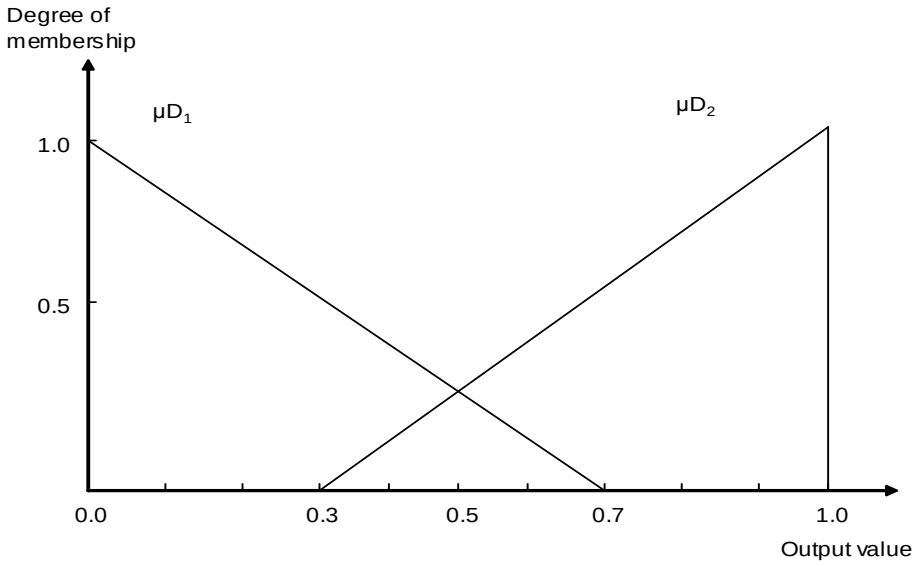

Figure 62. Output Membership Functions μD_1 and μD_2.

7.4.1 Fuzzy Inference Rules

There are a total of 16 possible fuzzy rules. Two rules are selected based on heuristic knowledge. They are represented as follows:

R_1: If μA_1 ('is malignant' from textural feature) and μB_1 ('is malignant' from horizontal distribution) and μC_1 ('is malignant' from vertical distribution)

Then μD_2 ('is malignant').

R_2: If μA_2 ('is benign' from textural feature) and μB_2 ('is benign' from horizontal distribution) and μC_2 ('is benign' from vertical distribution)

Then μD_1 ('is benign').

Else

Provide warning to user.

Here, the else action prevents system instability and warns the user of potential unintended erroneous results.

Using max-min inference, the output is given by Equation 21.

$$D' = (A_1' \times B_1' \times C_1' \circ R_1) \cup (A_2' \times B_2' \times C_2' \circ R_2) \qquad \textbf{Equation 21}$$

where

$$A_1' \times B_1' \times C_1' \circ R_1 = \underset{v,l,m}{\vee} [\mu_{A1'}(v) \cdot \mu_{B1'}(l) \cdot \mu_{C1'}(m)] \wedge [\mu_{A1}(v) \cdot \mu_{B1}(l) \cdot \mu_{C1}(m) \cdot \mu_{D1}(z)]$$

$$A_2' \times B_2' \times C_2' \circ R_2 = \underset{v,l,m}{\vee} [\mu_{A2'}(v) \cdot \mu_{B2'}(l) \cdot \mu_{C2'}(m)] \wedge [\mu_{A2}(v) \cdot \mu_{B2}(l) \cdot \mu_{C2}(m) \cdot \mu_{D2}(z)]$$

7.5 Results of the Fuzzy Inference Systems

The fuzzy inference systems using the 2×1D approach to capture the spatial statistical distribution of malignancy and the GLCM, RNN, and Wavelet-based approaches to capture the textural information are applied to five TRUS images for evaluation purposes. The results are correlated with the radiologist determined malignant regions to produce the ROC analysis.

7.5.1 Fuzzy Inferencing Results Using GLCM Textural Features

The ROCs of the FIS result using the GLCM energy and homogeneity textural features are displayed in Figure 63.

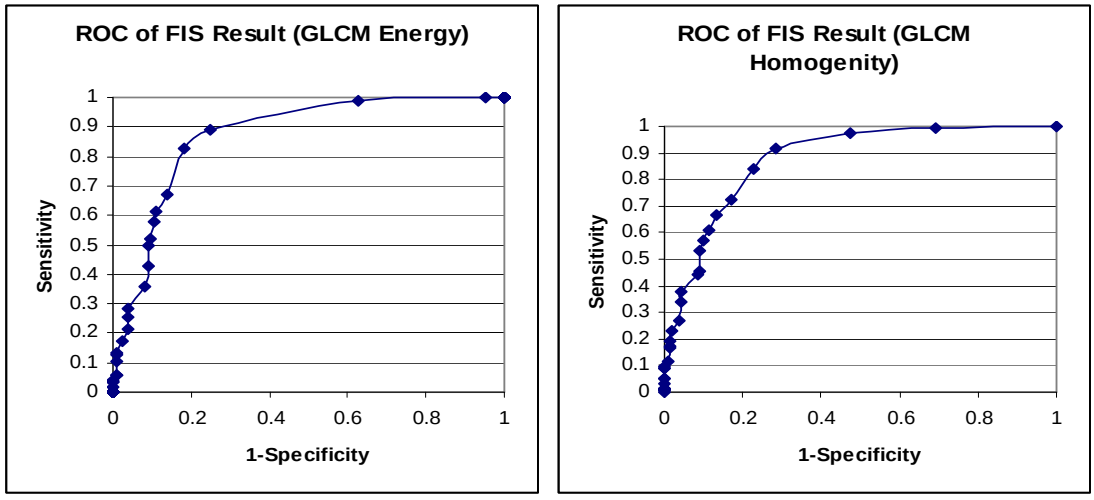

Figure 63. ROC of FIS Result (GLCM Energy and Homogeneity).

The AUC for the FIS using the GLCM energy and homogeneity textural features are $A_{z,E}$=0.87 and $A_{z,H}$=0.88 respectively. The outputs of the FIS using the GLCM features are contrasted with the desired output in Figure 64.

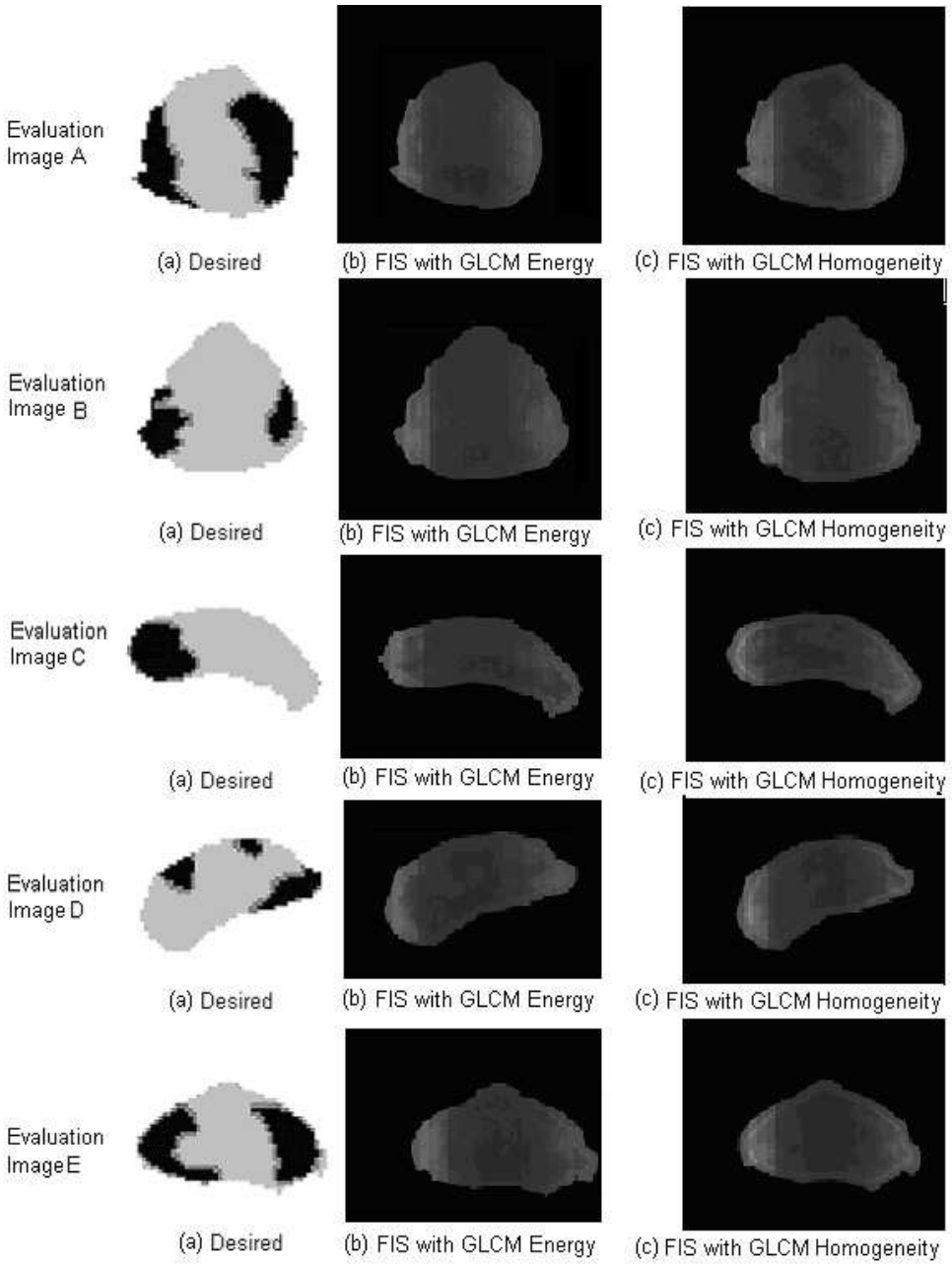

Figure 64. The Desired Segmentation and the Outputs of the FIS with GLCM Textural Features.

7.5.2 Fuzzy Inferencing Results Using RNN Textural Features

The ROC of the FIS result using the RNN textural features is displayed in Figure 65.

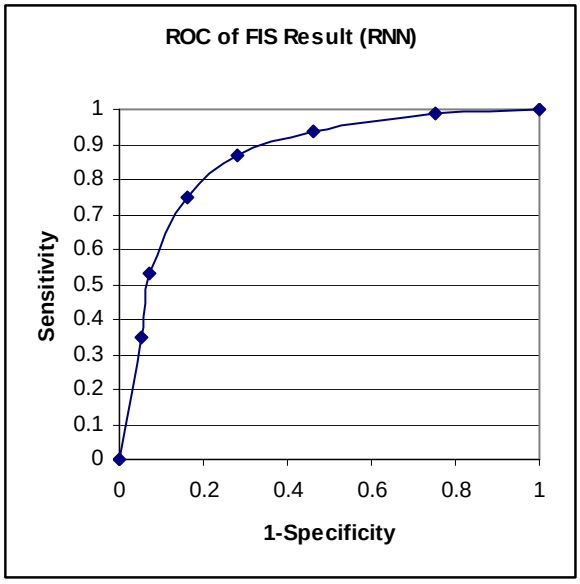

Figure 65. ROC of FIS Result (RNN).

The AUC for the FIS using RNN texture features is $A_{z,R}$=0.87. The outputs of the FIS using the GLCM parameters are contrasted with the desired output in Figure 66.

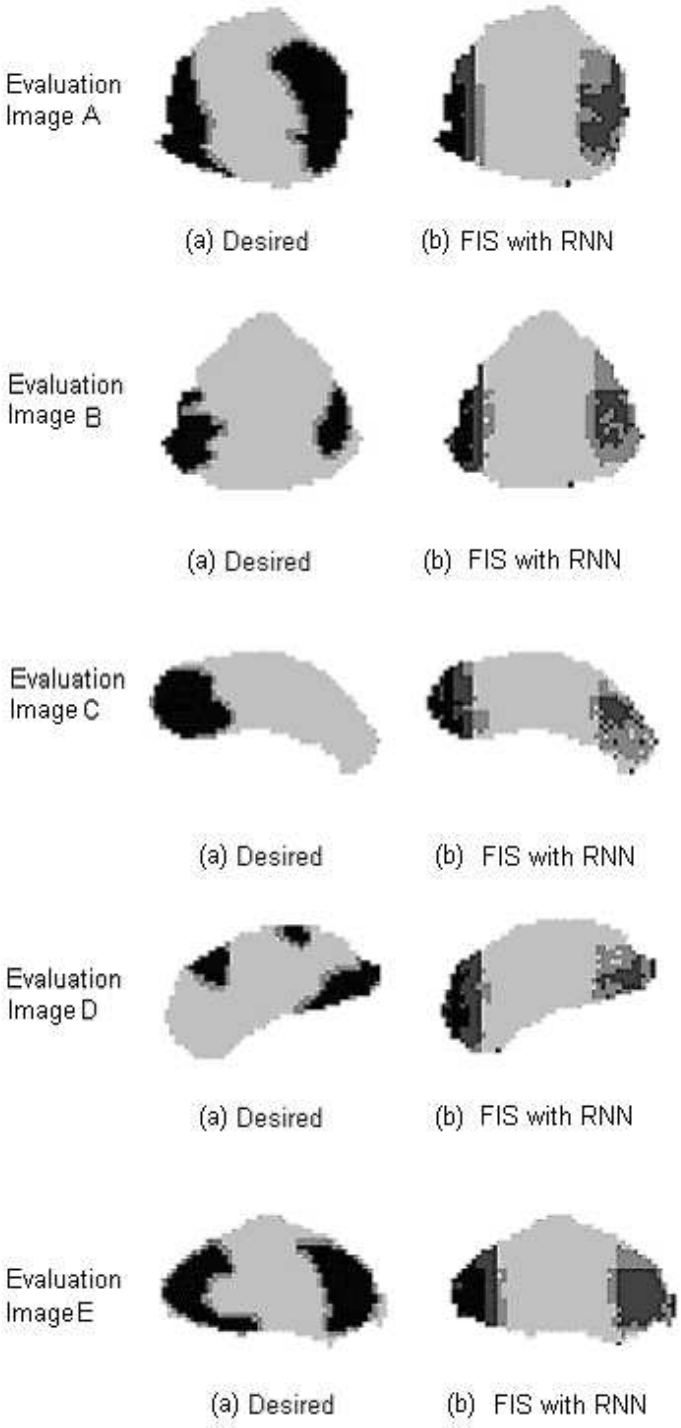

Figure 66. The Desired Segmentation and the Outputs of the FIS with RNN Textural Features.

7.5.3 Fuzzy Inferencing Results From Wavelet-based Textural Features

The ROC of the FIS result using the Wavelet-based textural features is displayed in Figure 67.

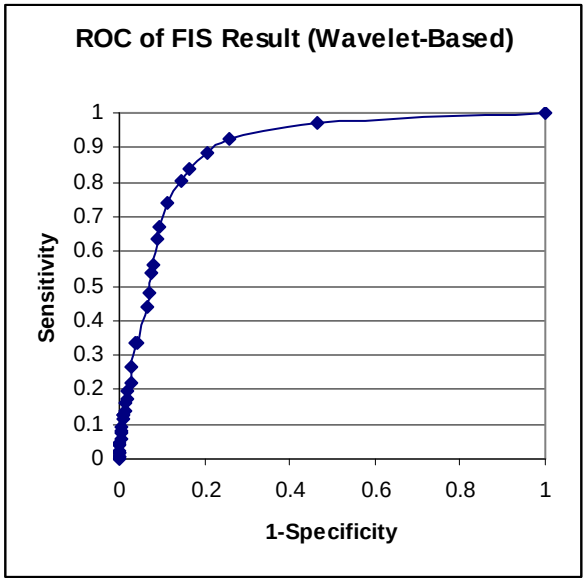

Figure 67. ROC of FIS Result (Wavelet-based).

The AUC for the FIS using the Wavelet-based texture features is $A_{z,W}$=0.89. The outputs of the FIS using the Wavelet-based features are contrasted with the desired output in Figure 68.

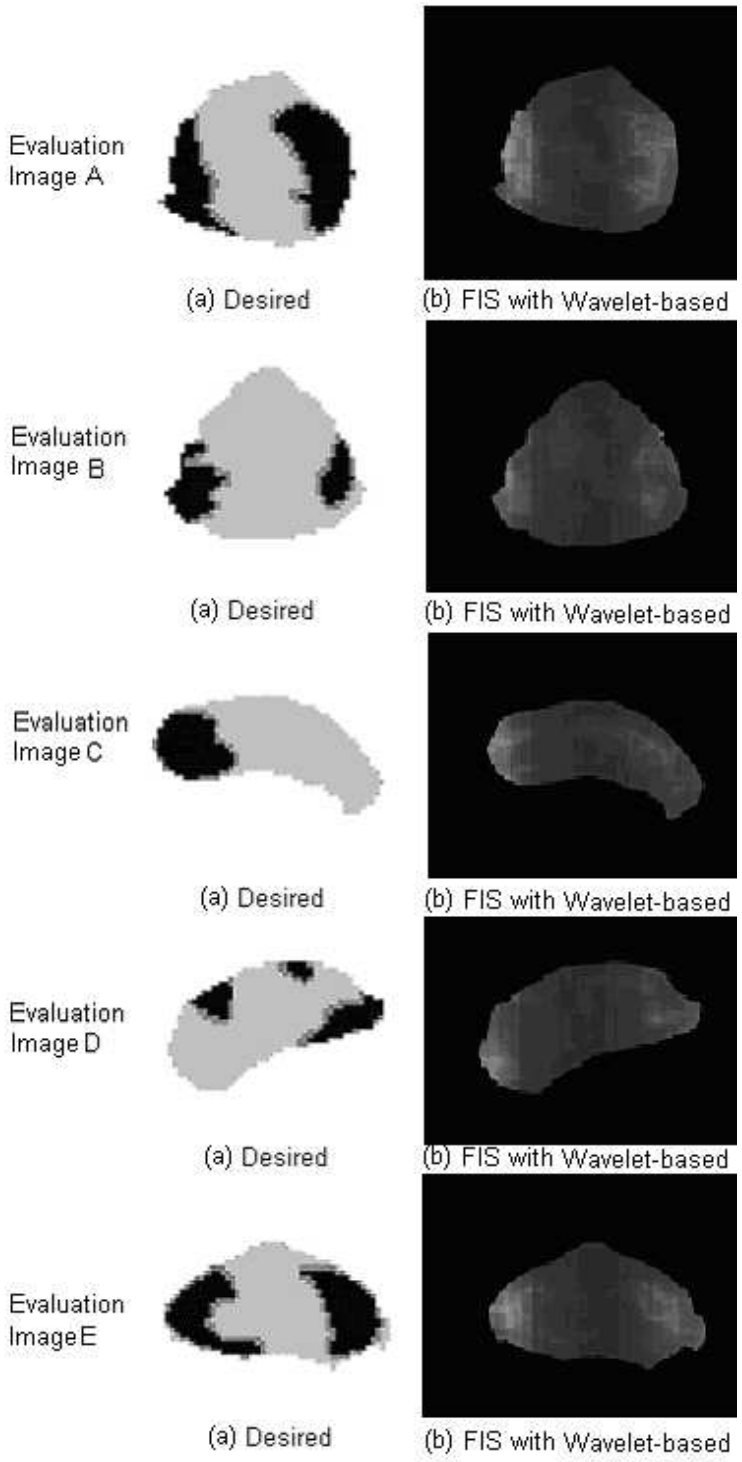

Figure 68. The Desired Segmentation and the Outputs of the FIS with Wavelet-based Textural Features.

7.6 Chapter Summary

This chapter examined the 2×1D membership function approach to extract the statistical spatial feature of malignancy. The process of converting feature distributions into fuzzy membership functions is also described. We also defined the fuzzy inference rules and applied the inferencing to TRUS images in order to achieve classification of malignant and benign regions. The AUC achieved using the various textural feature extraction approaches are listed in Table 4.

Table 4. AUC of the FIS Results Using the Various Approaches for Textural Feature Extraction and the 2×1D membership function approach for spatial feature extraction.

Textural Feature Extraction Approach	AUC
GLCM Energy	0.87
GLCM Homogeneity	0.88
RNN	0.87
Wavelet-based	0.89

From Table 4, it is noted that the Wavelet-based approach to extract the textural feature results in the best FIS result.

Chapter 8
Multi-dimensional Membership Function for Capturing the 3D Statistical Spatial Distribution of Malignancy

8.1 Introduction

In this chapter, we introduced the notion of multi-dimensional fuzzy membership functions, with which multiple input values correspond to a single fuzzy membership value. We applied the multi-dimensional fuzzy membership function approach to capture the 3D statistical spatial distribution of malignancy in order to improve malignancy localization in trans-rectal ultrasound (TRUS) images for prostate cancer diagnostics. The multi-dimensional membership function approach is found to more closely approximate the true 3D statistical spatial distribution of malignancy compared to the classical 1D approach and it is found to provide higher sensitivity in detecting malignant regions in automated diagnostic analysis.

8.2 Prostate in 3D

In Chapter 7, the spatial feature is captured by 2 conventional 1D fuzzy membership functions, which represents the horizontal and vertical statistical distributions of malignancy in a 2D TRUS image. The two features were used as input into a fuzzy inference system (FIS), which provided the binary classification.

However, since the prostate organ is three dimensional, a 2D approach to capture the statistical distribution of malignancy is not entirely accurate. A set of 2D TRUS images are normally acquired by sweeping the ultrasound transducer along the oblique coronal direction from base to apex of the prostate. The growth of malignant tumour within the prostate is not uniform in the direction the series of 2D ultrasound images are acquired (from base to apex – Fig. 3.1), therefore, the statistical distribution of malignancy in different 2D TRUS slices differ.

In [42], Chen et al. studied the 3D nature of the statistical distribution of malignancy. The statistical distribution of the malignancy in the oblique coronal direction from the Chen study is presented in Figure 69, which demonstrates that the malignancy distributions from the base region to the apex region differ considerably.

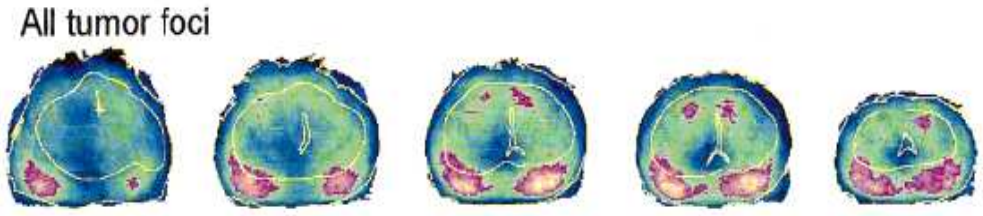

Figure 69. Statistical Distribution of Malignancy Along the Oblique Coronal Direction [42].

This chapter of the thesis aims to apply the fuzzy approach and used novel multi-dimensional fuzzy membership functions to capture the 3D statistical distribution of malignancy in prostates in order to provide more accurate diagnosis of cancer. In Section 8.2, three approaches to represent the 3D nature of the malignancy distribution are presented. The first approach is the n×2×1D fuzzy membership function approach. This approach uses traditional one dimensional fuzzy membership functions. However, it does not accurately represent the 3D distribution of the malignancy. To more accurately capture the 3D spatial distribution of the malignancy, the multi-dimensional fuzzy membership function is proposed in the second approach: the direct 3D fuzzy membership function approach. To improve the computational efficiency using the 3D fuzzy membership function, a reduced version of the 3D fuzzy membership function is introduced. In Section 8.3, results of the proposed approaches are presented and the major issues with the proposed approaches are discussed. The major findings of this chapter are concluded in Section 8.4.

8.3 Capturing the 3D Statistical Distribution of Malignancy

The original *2×1D* membership function approach to capture the statistical spatial distribution of malignancy is explored in Chapter 7. In this section, we developed several approaches to capture the 3D nature of the malignancy distribution more accurately, namely, the *n*×2×1D membership function approach, the direct 3D membership function approach, and the reduced 3D membership function approach. To demonstrate the results of the fuzzy inference system with the multi-dimensional membership function approaches, the RNN approach is applied to extract the textural features.

8.3.1 The *n*×2×1D Membership Function Approach

In the n×2×1D membership function approach, we are now considering the 3rd dimension or the *n* dimension, which represents a distorted version of the oblique coronal direction in the 3D prostate (distorted due to the fanned natured of TRUS image acquisition). Due to the limited number of samples that we have in this direction, which corresponds to the number of 2D TRUS images taken from base to apex, we will divide this dimension into only 3 discrete ranges (hence termed *n* direction). Applying medical terms, we can call these 3 ranges base, mid, and apex. We can divide the ranges by placing approximately 1/3 of the 2D image slices in each region. Once we have the 2D image slices divided into the 3 ranges, we can then obtain 1D membership functions similar to those in Figure 60 for each of the oblique coronal ranges. For the work in this chapter, we used 28 TRUS images from distinct TRUS sets, including 13 images of the base section, 9 of the mid section and 6 of the apex section. Six of the 13 images in the base section was used for construction of the base membership functions (Figure 70), 4 of the 9 in the mid section was used to construct the mid membership functions (Figure 71), and 3 of the 6 in the apex section was used for the apex membership functions (Figure 72).

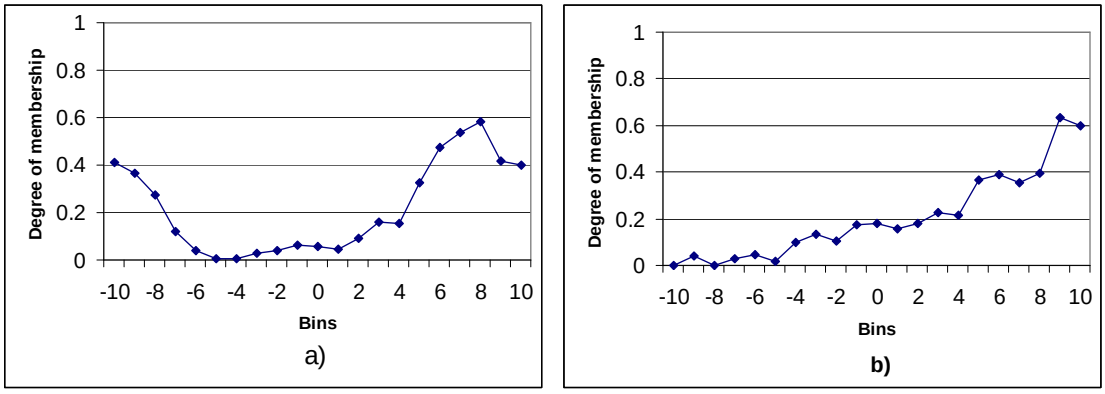

Figure 70. 1D Fuzzy Membership Functions in the Horizontal (*l*) (a) and Vertical (*m*) (b) Directions with *n*=1 (Base).

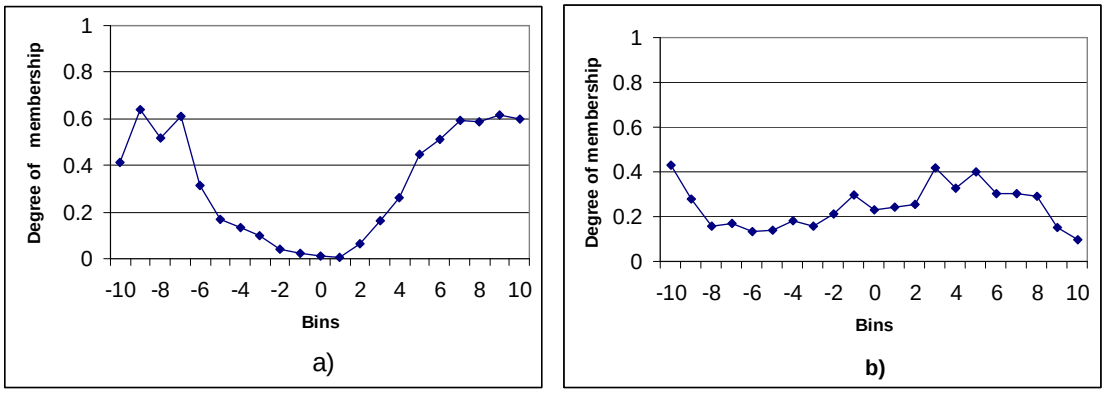

Figure 71. 1D Fuzzy Membership Functions in the Horizontal (*l*) (a) and Vertical (*m*) (b) Directions with *n*=2 (Mid).

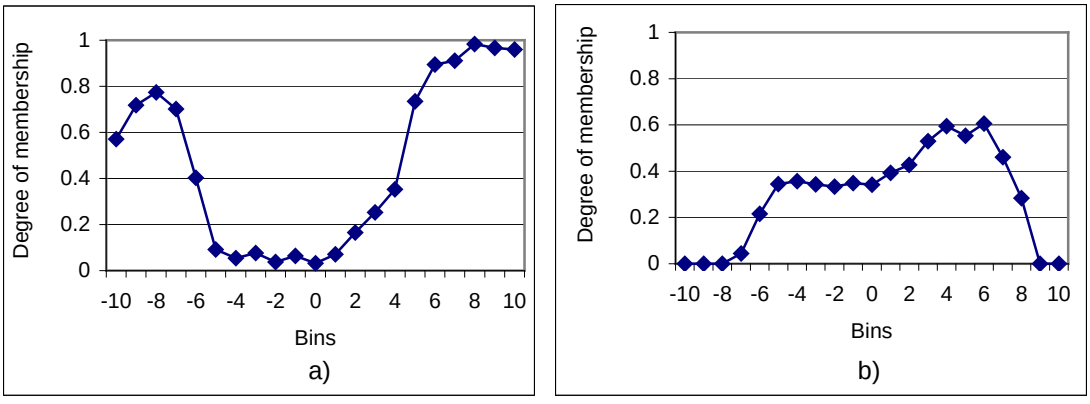

Figure 72. 1D Fuzzy Membership Functions in the Horizontal (*l*) (a) and Vertical (*m*) (b) Directions with *n*=3 (Apex).

When evaluating images, if we know which oblique coronal range the input image belongs to (the *n*-position), we can adaptively switch the *n* sets of 2×1D membership functions in the *l* and *m* directions to analyze the image with the appropriate statistical distribution (Figure 73).

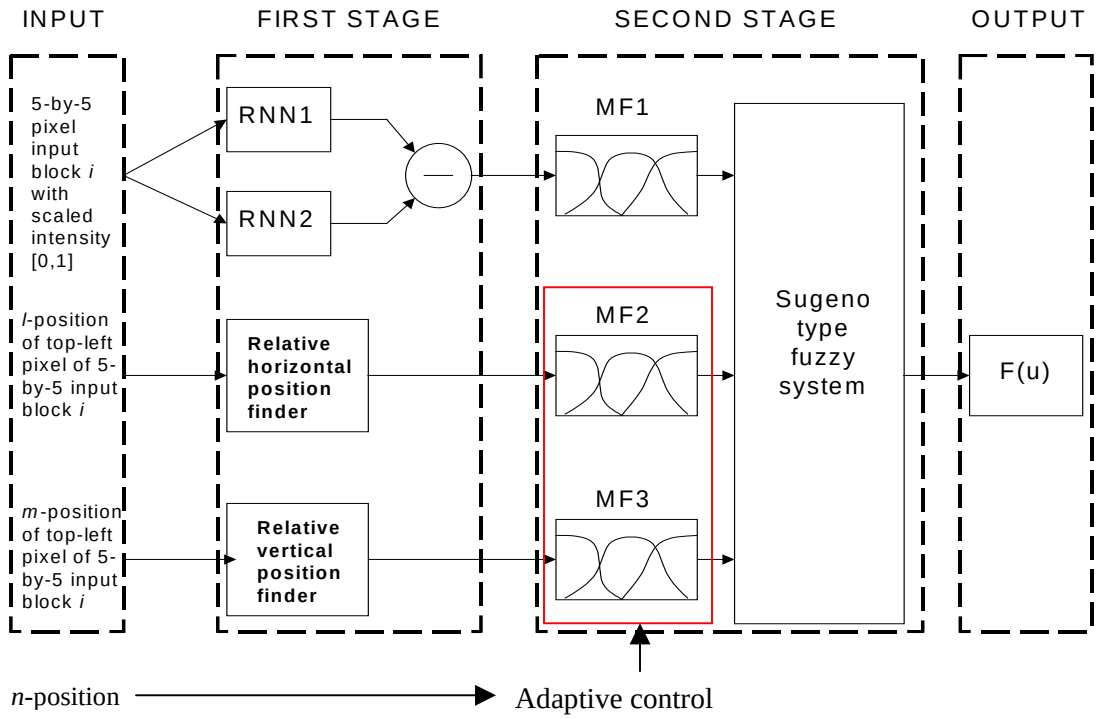

Figure 73. Fuzzy Inference System with Adaptive Member Function for Variables 2 and 3.

In the *n*×2×1D membership function approach, the fuzzy rules applied in the inference step are similar to that of the original approach. The difference is the *n* sets of 2×1D statistical membership functions and fuzzy relation matrices will be adaptively altered when applying the max-min inference depending on the *n*-position of the input image. The output for the *n*×2×1D membership function approach is given by the following equation:

$$D' = (A_1^{'} \times B_{1,n}^{'} \times C_{1,n}^{'} \circ R_{1,n}) \cup (A_2^{'} \times B_{2,n}^{'} \times C_{2,n}^{'} \circ R_{2,n}) \quad \textbf{Equation 22}$$

where

$$A_1^{'} \times B_{1,n}^{'} \times C_{1,n}^{'} \circ R_{1,n} = \underset{v,l(n),m(n)}{\vee} [\mu_{A1'}(v) \cdot \mu_{B1,n'}(l) \cdot \mu_{C1,n'}(m)] \wedge [\mu_{A1}(v) \cdot \mu_{B1,n}(l) \cdot \mu_{C1,n}(m) \cdot \mu_{D1}(z)]$$

$$A_2^{'} \times B_2^{'} \times C_2^{'} \circ R_2 = \underset{v,l(n),m(n)}{\vee} [\mu_{A2'}(v) \cdot \mu_{B2,n'}(l) \cdot \mu_{C2,n'}(m)] \wedge [\mu_{A2}(v) \cdot \mu_{B2,n}(l) \cdot \mu_{C2,n}(m) \cdot \mu_{D2}(z)]$$

where $\mu A_1(v)$ and $\mu A_2(v)$ represents the 1D RNN output difference membership functions, $\mu B_{1,n}(l)$ and $\mu B_{2,n}(l)$ represents the n-position l-direction 1D spatial distribution membership functions, $\mu C_{1,n}(m)$ and $\mu C_{2,n}(m)$ represents the n-position m-direction 1D spatial distribution membership functions, and $\mu D_1(z)$ and $\mu D_2(z)$ represents the output membership functions in Figure 62.

8.3.2 Capturing 3D Distribution: Direct 3D Membership Function Approach

In the direct 3D membership function approach, the probability of malignancy will be measured at the *l*×*m*×*n* (=20×20×3) discrete voxels in the 3D prostate. The measurement at each voxel will be converted to a discrete membership value. The set of *l*×*m*×*n* membership values will form the single 3D type I membership function. With discrete 3D type I membership functions, 3 inputs (the voxel location represented by *l*, *m*, and *n* values) relates to a single membership value. The 3D membership function 'is malign from 3D statistical distribution', $\mu_{B1,3D}(l_i, m_j, n_k)$, is displayed by 3 images representing the 2D membership function subsets $\mu_{B1,3D}(l_i, m_j, 1)$, $\mu_{B1,3D}(l_i, m_j, 2)$, and $\mu_{B1,3D}(l_i, m_j, 3)$ (Figure 74). The bright regions represent high degree of membership.

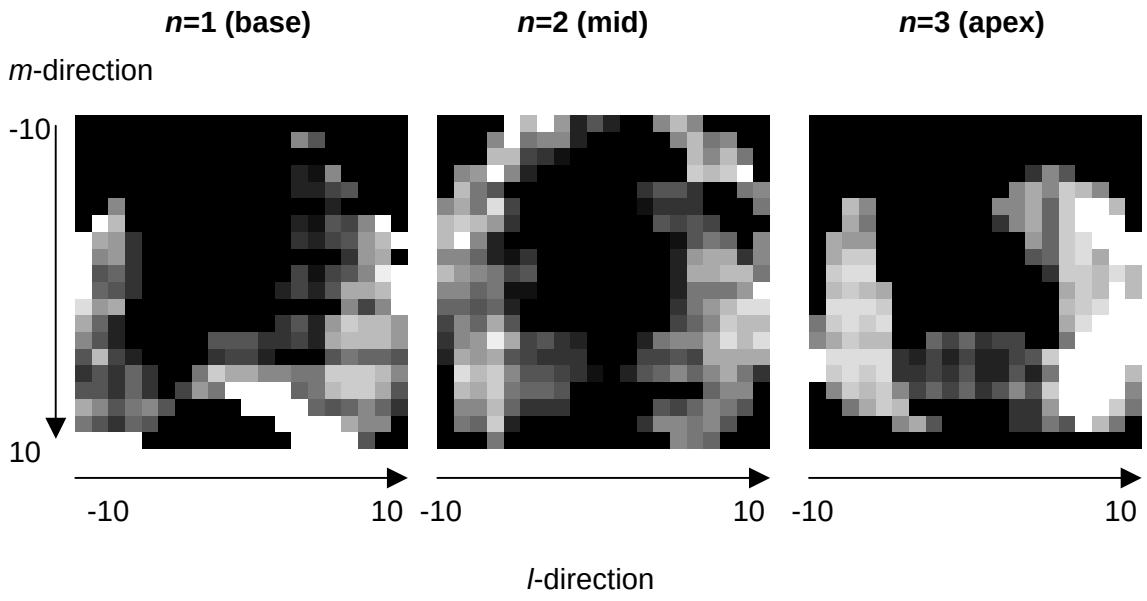

Figure 74. 2D Membership Function Subsets of the 3D Membership Function 'is Malign from Statistical Distribution'.

From Figure 74, we can see that the statistical distribution of malignancy extracted from sampling the discrete 3D voxels in the training images correspond well to the distribution collected by Chen in [42] (Figure 69). In the base section, the malignancy is concentrated at the two lower corners of the prostate. In the mid section, the malignancy is apparent in both the two low corners in the peripheral zone and parts of the transition zone in the top half of the slice. While in the apex section, malignancy is distributed in most of the peripheral zone across the entire *l*-direction range.

The reason for introducing the 3D membership function (MF) is to capture the 3D distribution of the malignancy more accurately. The following example shows how a single multi-dimensional membership function could capture the multi-dimensional data better than multiple single dimensional ones. Figure 75(a) shows the 2D distribution we would like to capture (1 and

0 beside the discrete point represent the distribution at that point) and the two classical 1D membership functions constructed from this distribution.

Figure 75(b) shows the result after applying product form of fuzzy relations. Compared to the original distribution, the representation of the distribution at each point on the 2D map by the two classical 1D MFs is severely distorted compared to the original distribution in (a). On the other hand, the 2D membership function would capture the distribution exactly.

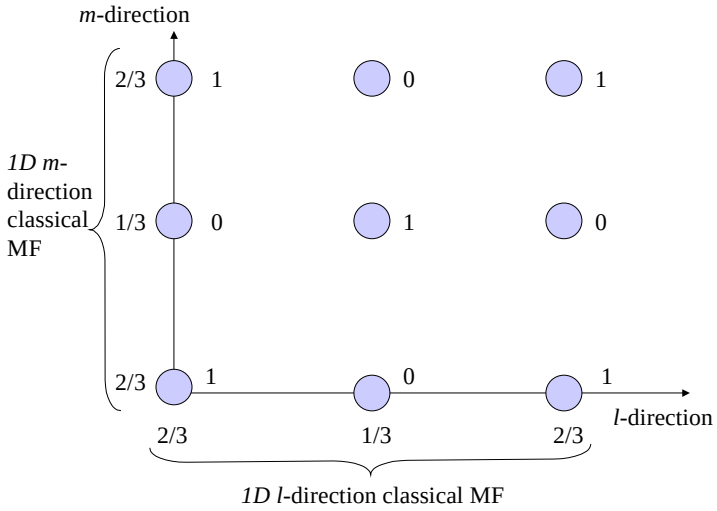

a) extracting 1D classical MFs from 2D distribution

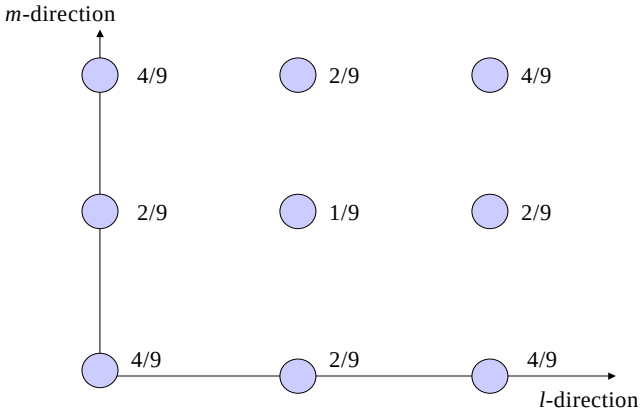

b) 2D distribution representation by 1D classical MFs.

Figure 75. Classical 1D Membership Functions Distorts Multi-dimensional Spatial Distributions.

The fuzzy inference system for the direct 3D membership function approach is displayed in Figure 76. The second stage FIS takes in 4 inputs (RNN output difference + spatial information in *l*, *m*, *n* directions). The FIS has two membership functions at the front-end, one 1D type I MF for the RNN output difference data and one 3D type I MF for the spatial data.

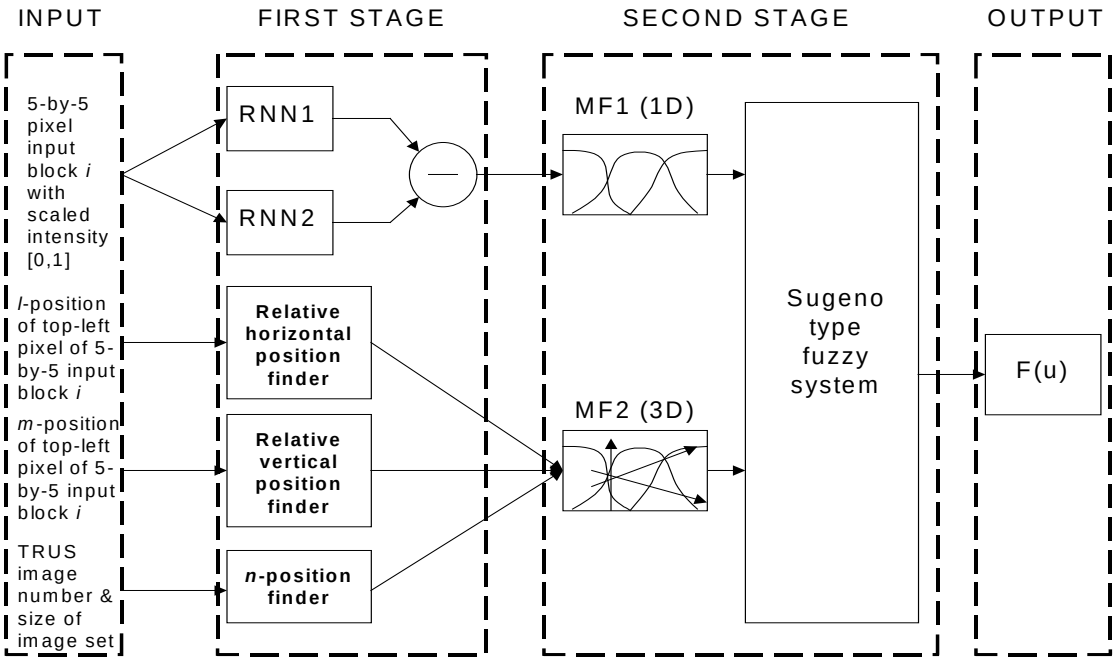

Figure 76. Neural-fuzzy System with 3D MF for Capturing Spatial Information.

To use the 3D membership function in the fuzzy inference system, we need to introduce composition rules for the 3D membership function. If we look at the 3D membership function as a multi-time folded version of the 1D membership function, then in theory, we could apply classical composition rules, with the only major difference being the number of input variables (3 per membership function instead of 1) and the size of the discrete membership function matrix (much larger than the 1D case, leading to greater computation requirements). The output for the direct 3D membership function approach is given by the following equation:

$$D' = (A_1^{'} \times B_{1,3D}^{'} \circ R_{1,3D}) \cup (A_2^{'} \times B_{2,3D}^{'} \circ R_{2,3D})$$ **Equation 23**

where

$$A_1^{'} \times B_{1,3D}^{'} \circ R_{1,3D} = \underset{v,l,m,n}{\vee} [\mu_{A1'}(v) \cdot \mu_{B1,3D'}(l,m,n)] \wedge [\mu_{A1}(v) \cdot \mu_{B1,3D}(l,m,n) \cdot \mu_{C1}(z)]$$

$$A_2^{'} \times B_{2,3D}^{'} \circ R_{2,3D} = \underset{v,l,m,n}{\vee} [\mu_{A2'}(v) \cdot \mu_{B2,3D'}(l,m,n)] \wedge [\mu_{A2}(v) \cdot \mu_{B2,3D}(l,m,n) \cdot \mu_{C2}(z)]$$

where $\mu A_1(v)$ and $\mu A_2(v)$ represents the 1D RNN output difference membership functions, $\mu B_{1,3D}(l,m,n)$ and $\mu B_{2,3D}(l,m,n)$ represents the 3D spatial distribution membership functions, $\mu C_1(z)$ and $\mu C_2(z)$ represents the output membership functions in Figure 62.

8.3.3 Capturing 3D Distribution: Reduced 3D Membership Function Approach

The direct 3D membership function is very computationally expensive. Although the fuzzy relation matrix involving the 3D membership function could be calculated in, we would still need to apply the fuzzy inferencing with the input values to this huge matrix during the evaluation step. Therefore, proposed solution 3 involves decomposing the 3D membership function in solution 2 to manageable 1D classical membership functions ("reduced 3D" approach).

A single N-dimension type I membership function could be collapsed to a (N-1)-dimension II membership function by fuzzifying the N^{th} dimension. By doing this, we retain range of membership values in the N^{th} dimension, but we lose the exact value relating the each discrete location in that dimension. We can also decompose a discrete N-dimension type I membership function into multiple (N-1)-dimension type I membership functions, or even more (N-2)-dimension type I membership functions without any lose of information.

For example, 1x(*m*x*l*x*n* 3D type I MF) = *N*x(*l*x*m* 2D type I MF) = *N*x*L*(*m* 1D type I MF) = *N*x*M*(*l* 1D type I MF). All four of these representations of the spatial distribution carry the exact same information. In the first instance, this data is carried within a single 3D type I MF, in the second

case, in *N* number of 2D type I MFs of size *l*x*m*, and in cases three and four, in *N*x*L* or *N*x*M* number of 1D type I MFs of size *m* or *l* respectively.

To construct the neuro-fuzzy segmentation system with this approach, we would first decompose the 3D type I MF found previously into either *N*x*M* *l*-sized 1D type I MF or *N*x*L* *m*-sized 1D type I MF. In this work, the latter approach was selected and 60 sets of 1D membership functions, $\mu B_{1,n,l}(m)$ and $\mu B_{2,n,l}(m)$, were constructed. The membership function 'is malign from statistical distribution at *n*=1 and *l*=7', $\mu B_{1,1,7}(m)$, is displayed in Figure 77.

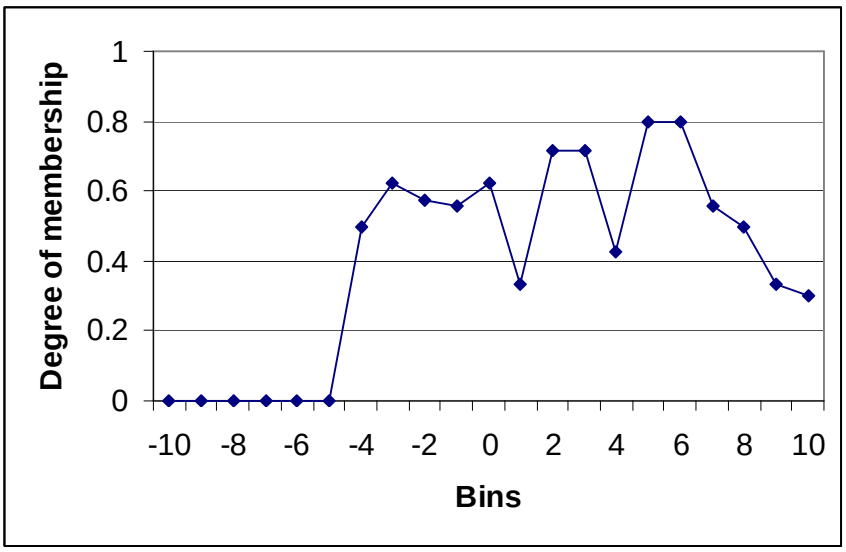

Figure 77. Decomposed 1D Membership Function Representing the Statistical Distribution of Malignancy at *n*=1 and *l*=7.

For this approach, in the fuzzy inference system, we would adaptively switch the *N*×*L* sets of 1D MFs based on the *n* and *l* positions (Figure 78).

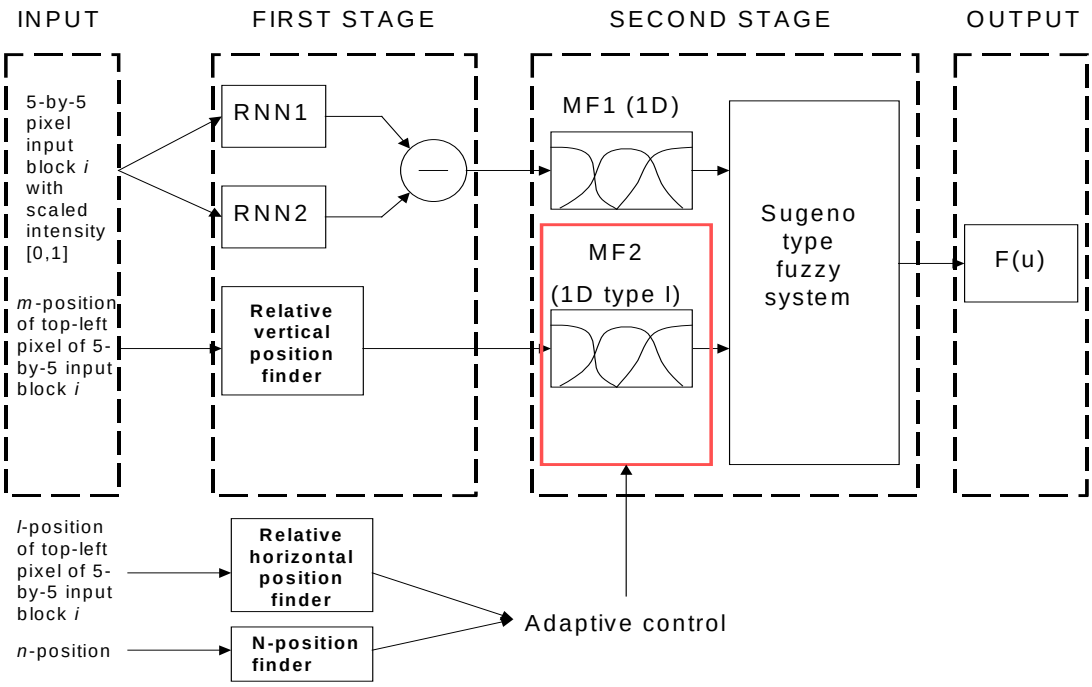

Figure 78. "Reduced 3D" Implementation of the Fuzzy Inference System.

The output given by the reduced 3D membership function approach is very similar to that of the direct 3D approach. However, computational time is significantly shortened in the reduced 3D approach. The output of the reduced 3D approach is given by the following equation:

$$D' = (A_1' \times B_{1,n,l}' \circ R_{1,n,l}) \cup (A_2' \times B_{2,n,l}' \circ R_{2,n,l}) \qquad \textbf{Equation 24}$$

where

$$A_1' \times B_{1,n,l}' \circ R_{1,n,l} = \underset{v,m}{\vee}[\mu_{A1'}(v) \cdot \mu_{B1,n,l'}(m)] \wedge [\mu_{A1}(v) \cdot \mu_{B1,n,l}(m) \cdot \mu_{C1}(z)]$$

$$A_2' \times B_{2,n,l}' \circ R_{2,n,l} = \underset{v,m}{\vee}[\mu_{A2'}(v) \cdot \mu_{B2,n,l'}(m)] \wedge [\mu_{A2}(v) \cdot \mu_{B2,n,l}(m) \cdot \mu_{C2}(z)]$$

where $\mu A_1(v)$ and $\mu A_2(v)$ represents the 1D RNN output difference membership functions, $\mu B_{1,n,l}(m)$ and $\mu B_{2,n,l}(m,)$ represents the 1D spatial distribution membership functions at spatial location n and l, $\mu C_1(z)$ and $\mu C_2(z)$ represents the output membership functions in Figure 62.

8.4 Results of the *n*×2×1D, Direct 3D, and Reduced 3D Approaches to Capture the 3D Distribution of Malignancy

In this section, the results of the *n*×2×1D, direct 3D, and reduced 3D approaches to capture the statistical spatial distribution of malignancy are compared in terms of ability to predict cancer location, computational time, and memory requirements. Some possible future improvements on the proposed method are discussed.

Shown in Figure 79, Figure 80 and Figure 81 are the desired segmentation results, results of the *n*×2×1D approach, results of the direct 3D approach, and results of the reduced 3D approach of 3 evaluation TRUS images belonging to the base, mid, and apex regions.

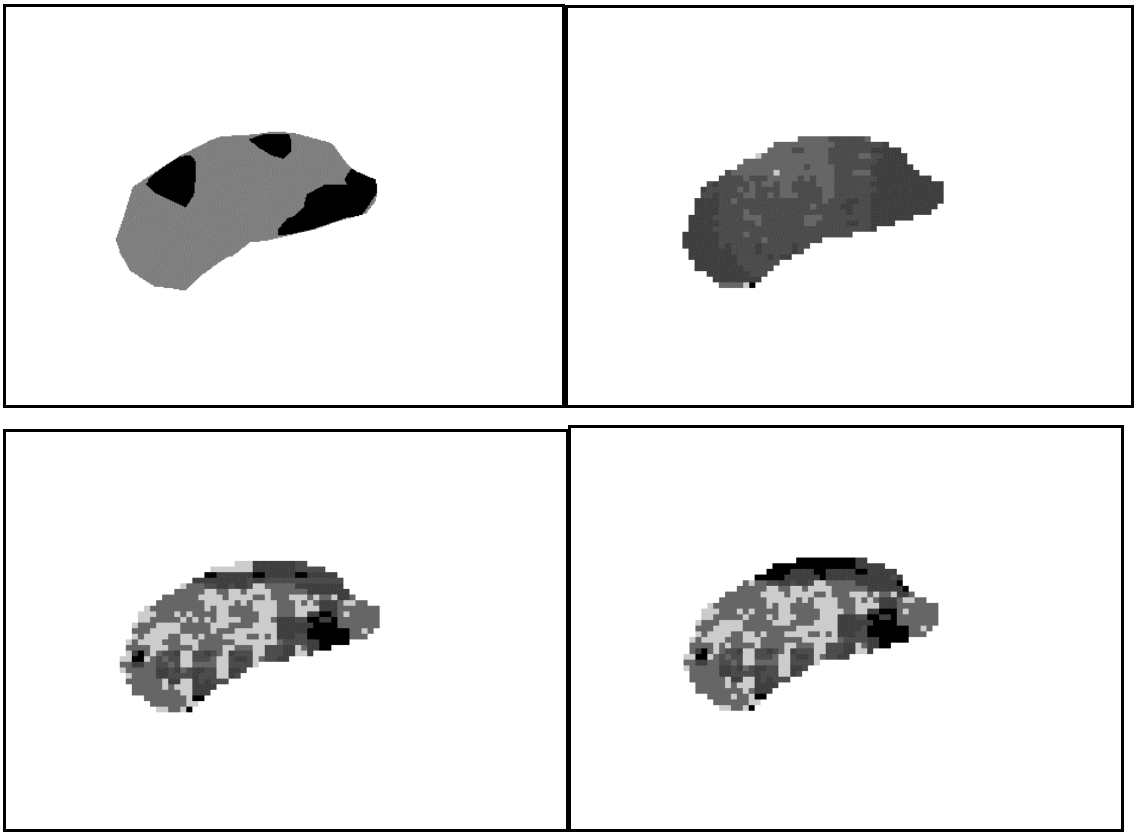

Figure 79. Evaluation Results of Base TRUS Image. a) Desired Segmentation (Top-Left). b) Result of *n*×2×1D Approach (Top-Right). c) Result of Direct 3D Approach (Bottom-Left) d) Result of Reduced 3D Approach (Bottom-Right).

For the base TRUS image in Figure 79, with the $n\times2\times1$D MF approach, we are able to identify one of the 3 malignant regions. The direct and reduced 3D approaches are much more sensitive and were able to identify all malignant regions.

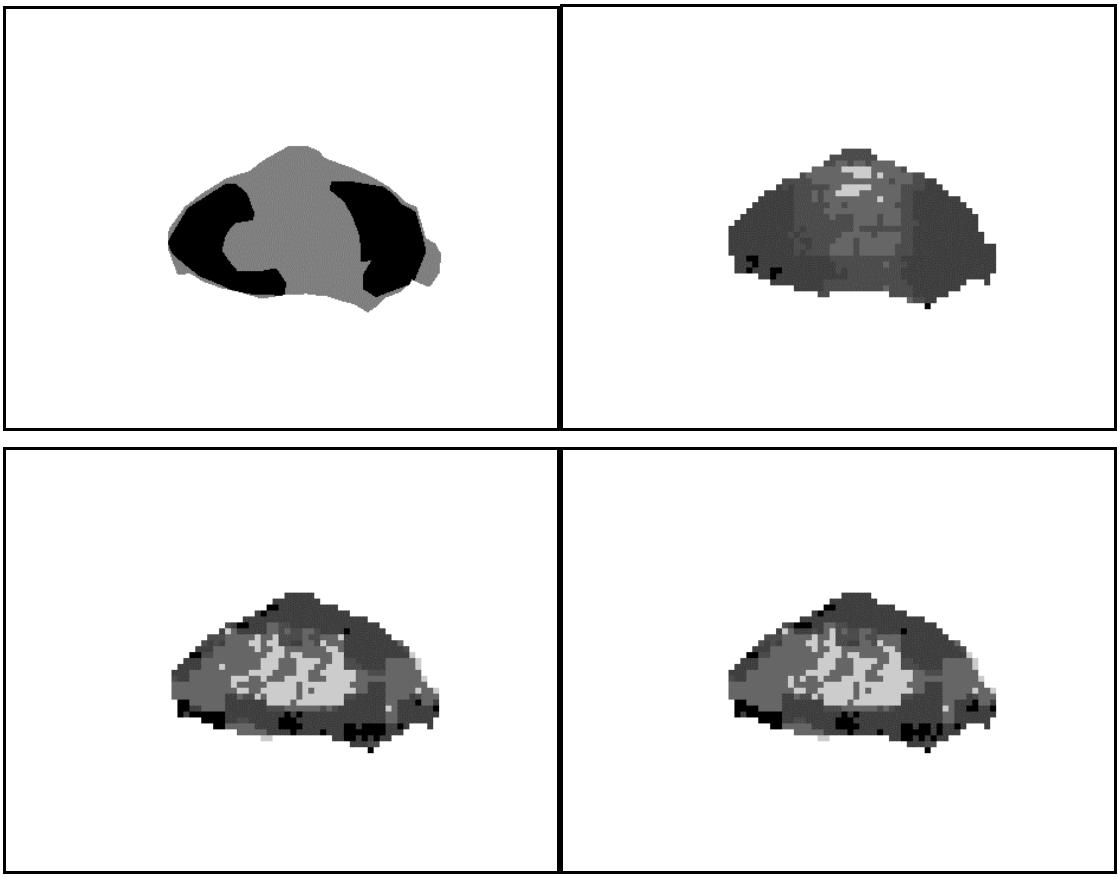

Figure 80. Evaluation Results of Mid TRUS Image. a) Desired Segmentation (Top-Left). b) Result of $n\times2\times1$D Approach (Top-Right). c) Result of Direct 3D Approach (Bottom-Left) d) Result of Reduced 3D Approach (Bottom-Right).

For TRUS image in Figure 80, the malignant regions are identified by all three approaches. However, the $n\times2\times1$D MF approach provided the smoothest and most accurate segmentation.

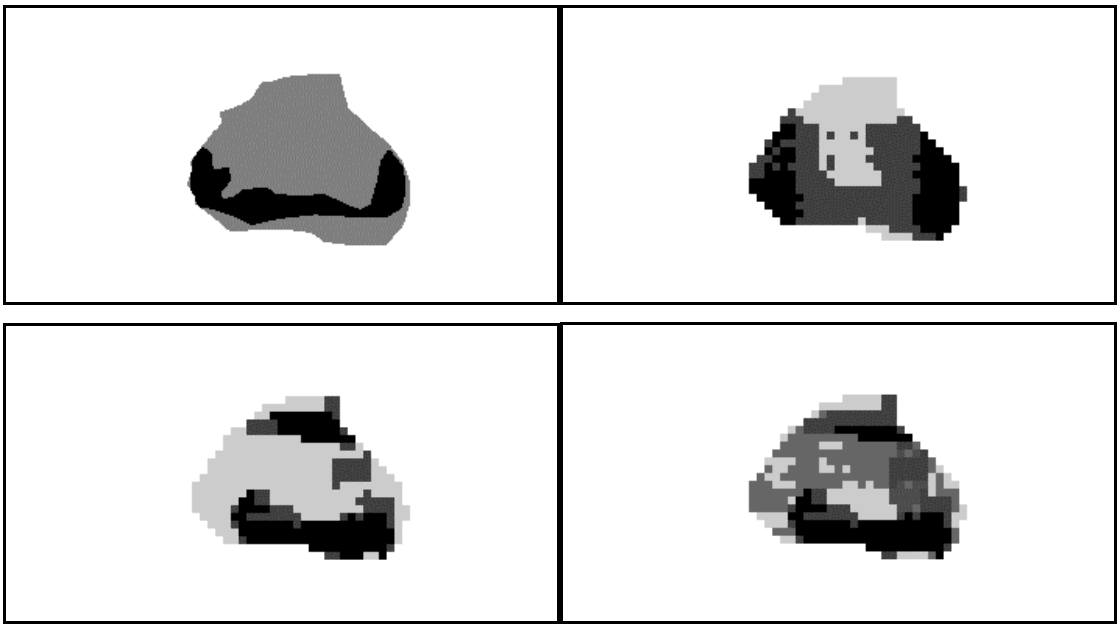

Figure 81. Evaluation Results of Apex TRUS Image. a) Desired Segmentation (Top-Left). b) Result of *n*×2×1D Approach (Top-Right). c) Result of Direct 3D Approach (Bottom-Left) d) Result of Reduced 3D Approach (Bottom-Right).

From classification examples in Figure 79, Figure 80 and Figure 81, the sensitivity (ability to detect malignancy regions) of the 3D approaches (both direct and reduced) appears to be superior to that of the *n*×2×1D approach as the former successfully identified all malignant regions in the TRUS images evaluated. This result was expected as the 3D MF approaches more accurately describes the 3D nature of the malignancy distribution within the prostate. However, the resulting segmentation using the 3D approaches are not as smooth as those provided by the *n*×2×1D approach. This could be attributed to the fact that an insufficient number of training images were used to form a smooth 3D statistical map of the malignancy.

The runtime and memory requirements of the three approaches are listed in Table 5.

Table 5. Runtime and Memory Requirement for *n*×2×1D MF, Direct 3D MF, and Reduced 3D MF Approaches to Capture the 3D Statistical Spatial Distribution of Malignancy.

Approaches	Runtime (seconds)	Memory
***n*×2×1D MF**	335.5	4134k
Direct 3D MF	4684.8	4138k
Reduced 3D MF	145.2	4212k

The algorithms are written in MATLAB script and are run on a P4-2.6GHz machine. The runtime is calculated as the time required to successfully classify 682 input samples with the respective approaches. Using the reduced 3D MF approach, the runtime was dramatically improved over the direct 3D MF approach. The memory requirement for the *n*×2×1D MF approach consists of six 1k data files to store the six spatial membership functions and six 688k pre-calculated fuzzy relation matrices. The direct 3D MF approach requires three 4k data file to store the membership function values and two 2,063k pre-calculated fuzzy relation matrices. The reduced 3D MF approach stores the membership functions in three 4k data files and requires one-hundred-twenty 35k files to store the pre-calculated fuzzy relation matrices. The total storage required for the three approaches are relatively the same.

In future works, we would like to use more data to construct more comprehensive 3D spatial distributions of the malignancy. If there are sufficient training data, we can also improve the spatial distribution accuracy in the oblique coronal direction by dividing the slices into more bins in the *n*-direction.

If knowledge on either the image number or total number of images of the set is not available, the exact oblique coronal position of the image could not be determined (*n*-position). In future

work, we would also like to explore type II fuzzy membership functions as a solution to this problem.

With the $n\times2\times1$D approach, for images without the oblique coronal direction label, we can apply a set of 1D type II membership functions in the l and m directions that are constructed by combining the three (oblique coronal) sets of type I membership functions.

For the direct 3D membership function case, we could collapse the 3D type I membership function into a 2D type II membership function, which is fuzzy with respect to the oblique coronal direction. The 2D type II membership function would have variable membership values at each of the $l\times m$ discrete membership locations. The variable membership values would be bounded by the maximum and minimum values at the $l\times m$ locations along the n-direction in the 3D type I membership function. The neural-fuzzy system with the 2D type II membership function is depicted in Figure 82.

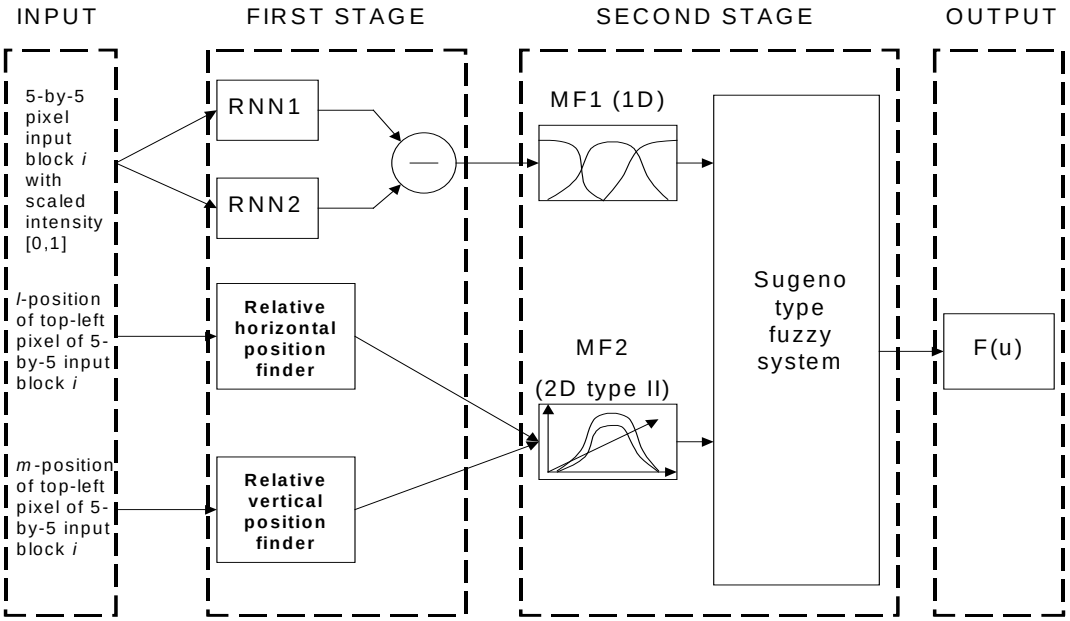

Figure 82. Neuro-fuzzy System with 2D Type II MF for Capturing Spatial Information.

For the reduced 3D approach, if n-position information is not available, we could modify MF2 in Figure 78 into 1D type II MFs.

8.5 Chapter Summary

In this chapter, we introduced 3 approaches to capture the 3D statistical spatial distribution of malignancy in TRUS images of the prostate for more accurate identification of the malignant region in prostate cancer diagnostics. The first approach to capture the 3D distribution is by using *n* sets of 2×1D classical fuzzy membership functions, with each 2×1D set representing the horizontal and vertical statistical distributions of malignancy in the n^{th} oblique coronal range. For a more accurate representation of the 3D statistical spatial distribution, we introduced the direct 3D membership function approach, in which the spatial distribution membership function is formed by spatially sampling the probability of malignancy in 3 quasi-perpendicular directions. The direct 3D MF approach captures the 3D distribution more accurately, but is very computationally inefficient. The reduced 3D MF approach stores the same amount of information as stored 3D MF, but applies fuzzy inferencing in a more computationally efficient manner to reduce computational complexity of the algorithm.

Chapter 9
Discussion and Future Work

Automated prostate cancer localization in TRUS images involves identifying the distinguishing feature classes, constructing and selecting the optimally distinguishing features, and designing a classifier to combine the features to provide a segmentation result.

The intensity feature is the one most often used by radiologists to identify malignant tumour. However, it is deemed suboptimal for computerized medical image analysis as the associated sensitivity and specificity from manual analysis using the intensity feature are low. A less visually perceptible feature, texture, is the main feature focused on to provide tissue segmentation in this thesis. This emphasis is partially due to experimentation and partially to the success of recent papers by Scheipers et al. whose approach concentrates on the texture features produced by the GLCM. My work examines the performance GLCM texture features alone with that of the RNN texture features. In order to improve on currently available texture feature extraction approaches, a novel texture feature extraction approach, based on the wavelet transform, is implemented. The main goal of the novel texture feature extraction method is to linearly separate, as much as possible, the distributions of the malignant and benign feature values in the feature space.

It is highly likely that the linear separability of the proposed wavelet-based textural feature could be improved. In Figure 50 and Figure 55 for example, the enhanced level 1 decomposition detail difference images show noticeable differences in the line structures in the malignant and benign regions. However, this distinction was not perfectly captured by the proposed local feature filter. It might be possible to obtain a better result by measuring the co-occurrence of certain values in the local region rather than counting the occurrence of *b*-connected values below the threshold *a*. This potential improvement will be explored in future works.

One advantage of the proposed approach to extract textural features is the removal of the effects of intensity inhomogeniety on the texture characterization process. If intensity inhomogeniety is present, both the GLCM and RNN approaches will treat this as a textural characteristic, which could lead to false negative classifications for isoechoic cancer. However, with the proposed approach, the extracted textural feature is minimally affected by intensity inhomogeniety and correctly classifies most isoechoic malignant regions (Figure 50 and Figure 53).

In this thesis, the spatial feature extraction is examined extensively to complement the texture feature. Unlike previous papers, for example those by Scheipers et al. who integrated the spatial information by a simple one dimensional feature, the distance between the pixel of interest to a fixed point, this thesis explores approaches which could capture the 2D and finally the 3D nature of the spatial information in a more comprehensive manner. This is accomplished by introducing the concept of multi-dimensional fuzzy membership functions.

The texture feature and spatial feature are then defused using a fuzzy inference system as a classifier. The fuzzy inference system is appropriate for this task because fuzzy membership functions has the ability to fully capture the overlapping nature of the distributions of the extracted features. An important issue examined in this thesis is how best convert the feature distributions into fuzzy membership functions which could be processed by the fuzzy inference system. This subject is discussed in Chapter 7.

In a clinical setting, the separation thresholds should be chosen according to criterions such as the mortality, discomfort to the patient, and expense associated with the treatment or non-treatment of the disease [43]. If the cost of missing a positive case is deemed great, the operator should adjust the thresholds to move to the left side of the ROC, where the sensitivity is high.

The shortcoming of using the statistics of the malignant tissue distribution is that for abnormal cases, where the location of the malignancy differs considerably from the normal distribution, the sensitivity of the second stage (Second stage refers to the result after integrating the texture and spatial features, whereas first stage refers to using only the texture feature for classification.) classifications is poor. Therefore, a system that can run two parallel segmentation algorithms, one configured for high sensitivity and one for high specificity, may be more appropriate in clinical diagnostic situations.

The fuzzy inference in the proposed system applies two simple rules that are based on heuristic knowledge. If there was more knowledge of the causality between the input features and the likelihood of malignancy, more rules can be incorporated into the system to improve its performance. Furthermore, since the overlap between the output membership functions μD_1 and μD_2 (Figure 62) is less than 50%, it may be beneficial to add a third triangular membership function μD_3, centred around the output value of 0.5. In cases where the input features present conflicting information, the function μD_3 can be used to capture this ambiguity.

Manual malignant tumour localization in TRUS images by a trained radiologist has a relatively moderate sensitivity and low specificity compared to that of a sextant prostate biopsy. In this work, we have shown that an automated region segmentation system can be designed to encapsulate expert knowledge and to provide segmentation results that closely approximate those obtained by an experienced radiologist. However, since manual segmentations are used to train the RNNs and construct the GLCM, wavelet-based texture feature distributions as well as the spatial malignancy distribution, the clinical performance of the automated system is upper-bounded by the limited accuracy of the manual segmentation training sets. It is certainly possible to improve the clinical performance of the system by using pathologically verified segmentation as training sets. Since this provides much more precise malignant and benign

region inputs into the RNN and a more representative texture feature distribution for the GLCM and wavelet-based approaches, the local textural properties of these two regions should be better encapsulated by the proposed system.

The local texture variations captured by the texture extraction approaches discussed in this work are unlikely to be distinguished by radiologists when they visually segment TRUS images. Therefore, if the proposed system is trained with precise pathologically verified segmentation, its performance, in terms of sensitivity and specificity, will be superior compared to that of manual segmentation. Since TRUS image acquisition is cheaper and less invasive than sextant prostate biopsies, the proposed system has the potential to be an important supplementary or alternative tool for conclusive prostate cancer diagnoses.

Chapter 10
Conclusion

Segmentation of the malignant and benign regions in TRUS images is difficult due to the inherent noise and low resolution in such images. This work identifies the distinguishing images features, constructs and selects the features, converts these features into fuzzy membership functions and combines the features using a fuzzy inference system. In this work, the design and construction of novel optimal features is emphasized.

In feature identification, the textural and spatial features are selected based on their effectiveness in identifying malignant tumour in TRUS, which is noted in existing research. Intensity based features are rejected due to their low diagnostic specificity. Three approaches are examined to capture the texture feature, including the conventional GLCM approach, the RNN approach, and the novel wavelet-based approach. The GLCM features have being applied previously for prostate cancer detection in ultrasound images. In this thesis, these features are used as a standard with which to measure the incremental performance of novel texture features. The RNN was found to be effective at segmenting white matter and gray matter in brain MRI. In this thesis, it has been adapted to distinguish between malignant and benign tissues in ultrasound images. The wavelet-based approach separates the textures in the image into deterministic and non-deterministic components by decomposing the image into subbands characterized by scale and orientation. This decomposition allows the removal of noisy texture elements that interferes with the diagnostic process. To apply the wavelet-based filter to extract the texture features, the malignant and benign tissue textures are first characterized. This involves searching for the subband that yields the minimal overlap between the benign and malignant distributions. This is the subband that optimally characterizes the differences between the textures of interest. Once the characteristic subband has been located, subsequent analysis

focuses solely on the wavelet detail coefficients of this subband. An enhanced version of the wavelet detail coefficients in the characteristic subband actually allows the operator to manually view the glandular growth patterns that are characteristic of the different grades of tumour growth.

Four approaches are designed to extract the statistical spatial features. In the first approach, two conventional one-dimensional fuzzy membership functions are used to represent the horizontal and vertical distributions of the malignancy in the TRUS image. In the second approach, multiple sets of 2×1D fuzzy membership functions are used to represent the malignancy distribution more accurately in the oblique coronal direction. In the third approach, a three-dimensional fuzzy membership function is introduced in order to improve the representation of the 3D nature of the malignancy distribution. In the fourth approach, computational complexity is taken into consideration and a reduced version of the 3D fuzzy membership function is introduced to improve the computation time. Multi-dimensional fuzzy membership functions provide a more accurate mapping of the malignancy in the 3D prostate organ as the malignancy distribution varies considerably from the base to the apex region of the prostate along the oblique coronal direction.

The proposed automated diagnostic system consists of two stages. In the first stage, only the local texture features are used for the region classification. The first stage output provides results with high sensitivity. In the second stage, the local texture features are combined with the spatial features with a fuzzy inference system. The second stage output provides significantly improved specificity and overall diagnostic accuracy.

The proposed automated diagnostic system is evaluated with TRUS images obtained using 7MHz ultrasound probes. Radiologist's manual segmentation was used as the gold standard. By

combining the texture feature with the spatial feature (represented by 2×1D fuzzy membership functions) using the fuzzy inference system, AUCs of 0.87 (GLCM energy), 0.88 (GLCM homogeneity), 0.87 (RNN) and 0.89 (Wavelet-based) are obtained.

Bibliography

[1] Chiu B., Freeman G.H., Salama M.M.A., Fenster A., Rizkalla K., Downey D.B. A segmentation algorithm using dyadic wavelet transform and discrete dynamic contour, Proc. of IEEE CCECE, Montreal, Canada, 2003.

[2] National Cancer Institute of Canada, Canadian cancer statistics 2002. Toronto, Canada, 2002.

[3] Loch T., Leuschner I., Genberg C., Weichert-Jacobsen K., Kuppers F., Retz M., Lehmann J., Yfantis E., Evans M., Tsarev V., and Stockle M. Future trends in transrectal ultrasound. Artificial Neural Network Analysis (ANNA) in the detection and staging of prostate cancer. Der Urologe A 39(4):341-347:2000.

[4] Scheipers U., Ermert H., Sommerfeld H.-J., Garcia-Schurmann M., Senge T., and Philippou S. Ultrasonic multifeature tissue characterization for prostate diagnostics. Ultrasound in Med. and Biol. 29(8):1137-1149:2003.

[5] Gleason D.F. Classification of prostatic carcinomas. Cancer Chemother. Rep 1966;50:125-128.

[6] Lawton C.A., Grignon D., Newhouse J.H., Schellhammer P.F., Kuban D.A. Oncodiagnosis panel: 1997 Prostatic Carcinoma, Radiographics 1999;19:185-203.

[7] Prostateline, http://hcp.prostateline.com/article/500067.aspx, 2004.

[8] Clements R. Has ultrasonography a role for screening for prostatic cancer? Eur. Radiol. 7:217-223:1997.

[9] Bushberg J.T., Seibert J.A., Leidholdt Jr. E.M., and Boone J.M. The essential physics of medical imaging, 2nd ed. Philadelphia, Penn: Lippincott, Williams & Wilkins; 2002:469-553.

[10] Schwartz L. Imaging and prostate cancer. J. Radiation Oncology 36(1-supplement):118:1996.

[11] Pham DL, Xu C, Prince JL. 2000. Current methods in medical image segmentation. *Annu. Rev. Biomed. Eng*. 02:315-37.

[12] Sahoo PK, Soltani S, Wong AKC. 1998. A survey of thresholding techniques. *Compt. Vis. Graph. Image Proc.* 41:233-60.

[13] Li, HD, Kallergi M, Clarke LP, Jain VK, Clark RA. 1995. Markov random field for tumor detection in digital mammography. *IEEE Trans. Med. Imaging* 14:565-76.

[14] Lee C, Hun S, Ketter TA, Unser M. 1998. Unsupervised connectivity-based thresholding segmentation of midsaggital brain MR images. *Comput. Biol. Med.* 18:309-38.

[15] Haralick RM, Shapiro LG. 1985. Image segmentation techniques. *Comput. Vis. Graph. Image Proc.* 29:100-32.

[16] Gibbs P, Buckley DL, Blackband SJ, Horsman A. 1996. Tumour volume detection from MR images by morphological segmentation. *Phys. Med. Biol.* 41:2437-46.

[17] Pohlman S, Powell KA, Obuchowski NA, Chilcote WA, Broniatowski SG. 1996. Quantitative classification of breast tumors in digitized mammograms. *Med. Phys.* 23:1337-45.

[18] Vannier MW, Butterfield RL, Jordan D, Murphy WA, Levitt RG, Gado M. 1985. Multispectral analysis of magnetic resonance images. *Radiology* 154:221-24.

[19] Laine A, Fan J. 1993. Texture classification by wavelet packet signatures, *IEEE Trans. Pattern Ana. Mach. Intel.* 15:1185-91.

[20] Liang Z, MacFall JR, Harrington DP. 1994. Parameter estimation and tissue segmentation from multispectral MR images. *IEEE Trans. Med. Imaging* 13:441-49.

[21] Pham DL, Prince JL. 1999. An adaptive fuzzy c-means algorithm for image segmentation in the presence of intensity inhomogeneities. *Pattern Recogit. Lett.* 20:57-68.

[22] Davatzikos C, Bryan RN. 1996. Using a deformable surface model to obtain a shape representation of the cortex. IEEE Trans. Med. Imaging 15:785-95.
[23] Cohen LD. 1991. On active contour models and balloons. *CVGIP: Image underst.* 53:211-18.
[24] Caselles V, Catte F, Coll T, Dibos F. 1993. A geometric model for active contours. *Numer. Math.* 66:1-31.
[25] Malladi R, Sethian JA, Vemuri BC. 1995. Shape modeling with front propagation: a level set approach. *IEEE Trans. Pattern Anal. Mach. Intell.* 17:158-75.
[26] Xu C, Prince JL. 1998. Snakes, shapes, and gradient vector flow. *IEEE Trans. Image Process.* 7:359-69.
[27] McNitt-Gray M.F., Huang H.K., and Sayre J.W. Feature selection in the pattern classification problem of digital chest radiograph segmentation, IEEE Trans. Med. Imaging 14:537-47:1995.
[28] Gelenbe E., Feng Y.T., Ranga K., and Krishnan R. Neural network methods for volumetric magnetic resonance imaging of the human brain, Proc. IEEE 84:1488-96:1996.
[29] Gonzalez RC, Woods RE. *Digital Image Processing, 2nd Ed*. Prentice Hall, Upper Saddle River, New Jersey, 2002, ch. 7.
[30] Georgiou G., Cohen F.S. Is early detection of liver and breast cancers from ultrasound scans possible? Patt. Rec. Let. 2003;24:729-39.
[31] Chen D.-R., Chang R.-F., Kuo W.-J., Chen M.-C. Huang Y.-L. Diagnosis of breast tumors with sonographic texture analysis using wavelet transform and neural networks. Ultrasound in Med. & Bio. 2002;28(10):1301-10.
[32] Lee W.-L., Chen Y.-C., Hsieh K.-S. Ultrasonic liver tissues classification by fractal feature vector based on M-band wavelet transform. IEEE Trans. Med. Imaging 2003;22(3):382-93.
[33] J. M. Francos, A. Z. Meiri, and B. Porat, “A unified texture model based on a 2-dWold-like decomposition,” IEEE Trans. Signal Processing, 1993;41:2665–2678.
[34] Gelenbe E. Random neural networks with negative and positive signals and product form solution. Neural Comp. 1(4):502-510:1989.
[35] Gelenbe E. Stability of the random neural network model. Neural Comp. 2(2):239-247:1990.
[36] Gelenbe E. Learning in the recurrent random neural network. Neural Comp. 5:154-164:1993.
[37] Daubechies I. Orthonormal basis for compactly supported wavelets, Commun. Pure Appl. Math., 1998;XLI:909-96.
[38] Obuchowski N.A., and McClish D.K. Sample size determination for diagnostic accuracy studies involving binomial ROC curve indices. Stastics in Medicine 16(13):1529-1542:1997.
[39] Hanley J.A., and McNeil B.J. The meaning and use of the area under the receiver operation characteristic (ROC) curve. Radiology 143:29-36:1982.
[40] Zadeh L.A. Outline of a new approach to the analysis of complex systems and decision processes. IEEE Trans. Syst. Man. Cybernet 3:28-44:1973.
[41] Zadeh L.A. Knowledge representation in fuzzy logic. IEEE Trans. Knowl. Data Eng. 1:89-100:1989.
[42] Chen ME, et al., Detailed mapping of prostate cancinoma foci: biopsy strategy implications, Cancer 2000;89:1800-09.
[43] Metz C.E. Basic principles of ROC analysis. Semin. Nuclear Med. VII(4):283-298:1978.